Field Testing and Simulating Servo-Aero-Gravoelastically Scaled Rotors for Extreme-Scale Wind Turbines

A Dissertation Presented to

The Faculty of the School of Engineering and Applied Sciences

University of Virginia

in Partial Fulfillment

of the Requirements for the Degree of

Doctor of Philosophy

By

Meghan Kaminski

August 2020

APPROVAL SHEET

The dissertation

is submitted in partial fulfilment of the requirements

for the degree of

Doctor of Philosophy

<u>Meghan Kaminski</u>
Author

The thesis has been read and approved by the examining committee:

<u>Eric Loth</u>
Advisor

<u>Daniel Quinn</u>

<u>Gavin Garner</u>

<u>Devin Harris</u>

<u>Daniel Todd Griffith</u>

Accepted for the school of Engineering and Applied Science:

August

2020

Abstract

Wind energy continues to grow as a valuable source of renewable energy due to the reduction in the levelized cost of energy over time. To achieve this growth, wind turbine sizes are growing beyond those predicted by conventional rotor designs. The increased turbine size allows for higher tower heights, accessing higher atmospheric wind speeds, and larger rotor diameters, allowing for more power capture. Such turbines are considered extreme-scale turbines (greater than 10 MW rated power) and consist of blades in excess of 100 meters in length. To reduce the gravitational loadings on blades of such sizes, the blades are designed to be lightweight which leads to highly flexible rotors as compared to conventional wind turbine blade designs. While computational methods have been developed and verified for conventional rotors, it is unknown if they are capable of capturing the dynamics of the highly-flexible, extreme-scale turbines. Experimental testing of the rotors can alleviate any uncertainties with simulations in fully understanding the interaction of gravitational, aerodynamic and elastic loads. While full-scale rotor testing is ideal to capture these dynamics, it can be prohibitively expensive in terms of both time and cost. Therefore, a sub-scaling method which captures the full-scale dynamics can prove beneficial to the development of novel extreme-scale designs.

In this study, a method for sub-scaling these ‘extreme-scale’ rotors is developed, applied, and verified through three different sub-scale turbine model designs. The scaling methods are based on a gravo-aeroelastic scaling (GAS) method which ensures the gravitational, aerodynamic, and elastic interactions of the full-scale blades are captured at a fraction of the cost in terms of time to build and materials needed. The following study begins with outlining the requirements of a computationally ideally-scaled turbine and describing the desired results of a sub-scale model based upon an extreme-scale rotor. This leads to a 1% additively manufactured blade model utilizing a bio-inspired designs in order to maintain the defined scaling requirements and is verified through structural testing. Finally, this study concludes with a 20% scale manufactured model based on the gravo-aeroelastic scaling method for experimental testing at the National Renewable Energy Laboratory’s Flatirons Campus. This model is then verified and compared against computational results for both parked and operational conditions.

Acknowledgements

Formally, I would like to acknowledge my advisor Dr. Eric Loth, the chair of the Department of Mechanical Engineering at the University of Virginia for the many hours he has spent passing on knowledge and leading me in the correct direction for graduate school. I may not have been his most conventional student, but created a diverse and welcoming environment for each of his students. Additionally, I would like to thank his wife Marie for patiently waiting while he often times worked to get me to where I am today. I would like to thank Dr. Kathryn Johnson from the Colorado School of Mines for being so welcoming and providing guidance throughout my graduate studies. Another thank you goes to Dr. Todd Griffith from the University of Texas at Dallas for providing significant amounts of direction with the included research study. Additional thanks go to the entirety of the Segmented Ultralight Morphing Rotor Team for their help and guidance on each of these chapters. Lastly, I would like to thank the members of the ARPA-E team: Mario Garcia-Sanz, Sonja Glavaski, Michael Olsen and Brenda Haendler. Without them and their guidance, this research would not be possible nor as impactful.

I would also like to thank the many family members and friends for putting up with my antics over the years and helping to support me in what it is I decide to focus in that moment. Most notably, I would like to thank my parents, Amy Beth and Paul Albert Kaminski. They have spent many hours supporting me through all adventures and I would not have gotten to where I am today without their support and guidance. A thank you goes to my sisters for never taking me too seriously and keeping me humble while growing up. I would like to thank Jacob Suydam for reading over my work and always being able to provide that one word that is ‘on the tip of my tongue’. A thanks to friends made from the University of Virginia, especially Catherine Perrin and Jessica Smith for listening and sitting through countless practice presentations and providing a place for me to decompress beyond the MAE offices. Finally, I would like to thank all my colleagues at the University of Virginia for their help with research and keeping me entertained outside of research, without them graduate school would not have been the wonderful experience I look fondly upon.

This work has been supported by ARPA-E under award number DE-AR0000667. Any opinions, findings, and conclusions or recommendations expressed in this material are those of the authors and do not necessarily reflect the views of ARPA-E.

Table of Contents

1. Introduction

1.1 Motivation for Parked Testing of Flexible Rotors

Wind energy has proven to be a dominant form of renewable energy with predictions showing this growth to continue upwards [1]. To match these trends, wind turbine designers are looking towards higher turbine heights to capture the higher wind speeds at higher altitude as well as longer blade lengths to increase the capture area of the turbine with a 135% growth in observed rotor diameters from 1998 to 2017 [2]. With the encouragement to continue to design such turbines, it is important to note these rotor display highly flexible dynamics as compared to the conventionally manufactured turbines [3] and can reach to such sizes that they are classified at extreme-scale wind turbines [3]. Such designs include Sandia National Lab's upwind 100-meter blade design series [4–7]. Each blade improves upon the last with the SNL100-03 turbine having a significant mass reduction as compared to earlier design iterations and as compared to conventional rotors [7]. Additionally, the 13-MW Segmented Ultralight Morphing Rotor (SUMR-13) design capitalizes on a downwind and coned rotor which allows for load alignment along the blades during operation [3,8–10]. The load alignment in the blades allows for a reduction in structural requirements, and thus reduction in mass. While each of these rotors, and other such extreme-scale rotors, has been computationally proven, the computational methods used were developed for conventionally sized rotors which offer a different set of dynamics as compared to extreme-scale rotors [11]. At the full-scale, GE Renewable Energy has deployed the Haliade-X turbine: a full-scale manufactured 12 MW rotor with 107-meter blade lengths for off-shore testing [12]. While is a monumental feat, the manufacturing of further design iterations will prove prohibitively expensive [13] and it becomes a major cost benefit to test the full-scale rotors at a sub-scale size. Therefore, the goals herein are to develop a sub-scaling methods for extreme-scale rotors which fully capture the dynamics of these highly flexible rotors.

1.2 Previous Studies

Previous studies have focused on sub-scale testing, however the goals of their studies differ from the goals presented herein. For example, floating sub-scale turbine have been experimentally tested to examine the wind-wave impacts on turbine substructures in off-shore conditions at 1/50th scale [14,15] based on the National Renewable Energy Laboratory's 5-MW, 126-meter reference turbine [16]. For each of these studies, the designs were Froude scaled to ensure the wind-wave loads on the rotor were maintained on the rotor and platform; however, they were at such a scale, the Reynolds number differences needed to be corrected for. For each of these studies, the blade mass and stiffness scaling was not a priority as the goal was to observe the platform dynamics.

To reduce the effects of the Reynolds number on the sub-scale models, select studies utilize intermediate-scale rotors designed based on their full-scale counterpart. These tests include Poseidon, a prototype wind turbine deployed on a platform which additionally extracts wave energy [17,18]. Another such intermediate-scale test is the SWiFT facility, an intermediate-scale wind farm for testing wind turbine wakes at Sandia National Laboratories. Lastly, the Vulturn-US tests deploy a 1/8th scale rotor of a 76.8 m diameter turbine for testing offshore of Maine to explore the wind-wave loads on a semi-submersible hull [19–21]. While each of these tests has met their research objectives, the gravo-aeroelastic scaling of the blades was not a top priority and many of the gravo-aeroelastic dynamics of the blades were not captured at the sub-scale.

To capture these dynamics, a servo-aero-gravoelastic (SAGE) scaling method is proposed for operational conditions which captures the necessary dynamics and deflections present in the full-scale model at a sub-scale size [22]. This type of scaling considers the blade geometry (blade length, airfoil shapes and distribution, etc.), dynamics (frequencies relative to rotor RPM, tip-speed ratio, etc.), and loads (gravitational, centrifugal, and aerodynamic) to ensure proper non-dimensional dynamics and deflections in the full-scale are present in the sub-scale models. To accomplish these requirements, the GAS method aims to match the non-dimensional tip-speed ratio, the ratio of rotational speed to first flapping frequency, and the operational tip deflections normalized by blade length.

1.3 Study Objectives

The objective of the present study is to develop and test a gravo-aeroelastic scaling (GAS) method for extreme-scale wind turbine rotors. To accomplish this, the scaling method is developed for an ideal sub-scale rotor and is computationally applied for an ideal 20% scale SUMR-13 (SUMR-IS) turbine which also includes scaling of the control systems for a servo-gravo-aeroelastic scaling method (SAGE). The SUMR-IS model shows the effects of Reynolds number on the sub-scale model and explores the significance of these effects on the goals and objectives as set out by the GASE scaling method. This study proceeds to show the scaling method on a 1% additively manufactured model of the extreme-scale SNL100-03 rotor model. This model utilizes a bio-inspired structural design in order to meet the strict mass and stiffness constraints of the full-scale model. Despite matching the distributed mass and stiffness, the model was not aerodynamically tested due to the large differences in Reynolds number at the 1% scale.

The final model used to explore the scaling method is the 20% manufactured model of the SUMR-13 rotor, the SUMR-Demonstrator (SUMR-D). This rotor model was scaled using gravo-aeroelastic scaling for testing at the National Renewable Energy Laboratory's Flatirons Campus (NREL FC) which offers an environment which has significantly higher wind speeds than that of an environment modelled to be ideally scaled from the full-scale SUMR-13 environment. The manufacturing, proof testing, and installation of the blades are shown in Figure 1-1. The high wind conditions of the NREL FC caused the blade's non-dimensional mass and stiffness to be higher than that of the full-scale, but still significantly less than that of a conventional rotor. To test the scaling method on these blades, the SUMR-D blades were tested in parked conditions for both pitch-to-run configuration and pitch-to-feather configurations as well as operational conditions. These experimental results were compared against the computational results for a 'digital twin' of the manufactured model as well as the full-scale SUMR-13 model to determine whether the sub-scale model was able to capture the dynamics of the highly flexible full-scale SUMR-13 turbine.

a)

Photo by Rick Damiani, NREL

b)

Photo by Lee Jay Fingersh, NREL

c)

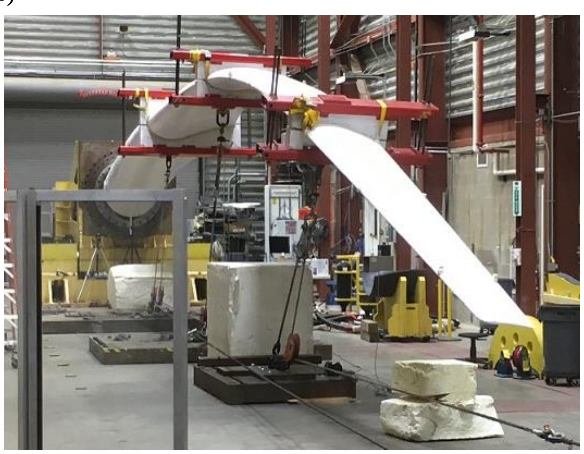

Photo by Scott Hughes, NREL

d)

Photo by Lee Jay Fingersh, NREL

Figure 1-1: Manufacturing process for the Segmented Ultralight Morphing Rotor Demonstrator used in Chapters 3, 4 and 5 showing a) the blade mold, b) the root of the blade and the strain gauges used for bending moments, c) load testing of the blade, and d) final installation of the blades.

This is the first in depth study to explore and develop the gravo-aeroelastic scaling method to properly match the full-scale dynamics and deflections of a highly flexible extreme-scale wind turbine blade. As such, this is also the first study which demonstrates a small-scale wind turbine rotor which uses additive manufacturing to develop a bio-inspired structural design to match the dynamics of a highly flexible full-scale turbine. Additionally, this is the first study to use the gravo-aeroelastic scaling method at an intermediate scale for both operational and parked conditions.

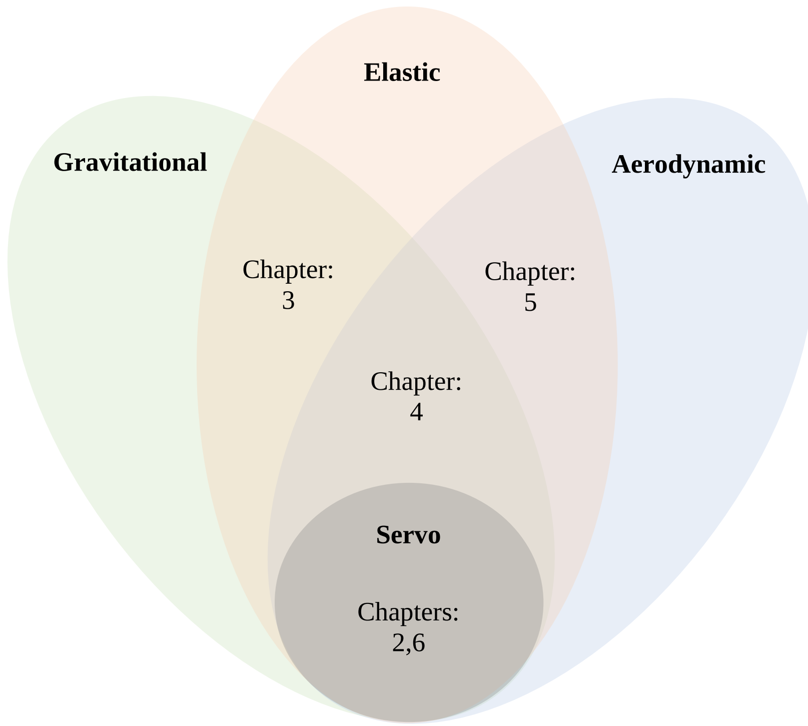

Figure 1-2: Summary of chapters and the portion of the servo-aero-gravoelastic scaling method explored.

Figure 1-2. shows the connection of each of the chapters to the servo-aero-gravoelastic scaling method where the following study begins with Chapter 2 defining the full servo-aero-gravoelastic scaling method and applies it to the SUMR-13 rotor. The scale model in question is an ideally scaled model and is computationally compared against the full-scale model to explore the Reynolds number effects on a GAS wind turbine. Chapter 3 reduced the scaling method to a gravo-elastic model and applied it to the SNL100-03 blade for an additively manufactured 1% scale model utilizing bio-inspired structural design to meet the strict mass constraints. This model was structurally tested using static loads equivalent to appropriately scaled aerodynamic loads but was not aerodynamically tested due to the large Reynolds number differences. As such, this model was defined as being gravo-elastically scaled. Chapter 4 proceeds to define and manufacture a gravo-aeroelastic 20% model of the SUMR-13 blades for a gravo-aeroelastically scaled model. The manufactured blades are ground tested and the 'digital twin' of the manufactured blades are computationally compared against the full-scale results. Chapter 5 utilizes the manufactured blade developed in Chapter 4 and compares the parked experimental results against computational results of the full-scale model. The results explore a non-dimensional comparison of the blade root moments and tip deflections between the experimental results and computational results of the SUMR-D and SUMR-13 turbine. This study removes the effects of gravity and is therefore an aeroelastic model. Chapter 6 mirrors Chapter 5 and applies the methods to operational results which have altered controls to present the full results of the application and execution of the scaling method on the SUMR-13 rotor. Finally, Chapter 6 provides concluding remarks for the presented study.

References

[1] Sugawara, E., and Nikaido, H. "EIA Energy Outlook 2020." *Antimicrobial Agents and Chemotherapy*, Vol. 58, No. 12, 2019, pp. 7250–7257. doi:10.1128/AAC.03728-14.

[2] Wiser, R., and Bolinger, M. *2017 Wind Technologies Market Report*. 2017.

[3] Noyes, C., Qin, C., and Loth, E. "Pre-Aligned Downwind Rotor for a 13.2 MW Wind Turbine." *Renewable Energy*, Vol. 116, 2018, pp. 749–754. doi:10.1016/j.renene.2017.10.019.

[4] Griffith, D. T., and Ashwill, T. D. *The Sandia 100-Meter All-Glass Baseline Wind Turbine Blade : SNL100-00*. 2011.

[5] Griffith, D. T. *The SNL100-01 Blade: Carbon Design Studies for the Sandia 100-Meter Blade*. 2013.

[6] Griffith, D. T. *The SNL100-02 Blade : Advanced Core Material Design Studies for the Sandia 100- Meter Blade*. 2013.

[7] Griffith, D. T., and Richards, P. W. *The SNL100-03 Blade : Design Studies with Flatback Airfoils for the Sandia 100-Meter Blade*. 2014.

[8] Ananda, G. K., Bansal, S., and Selig, M. S. "Aerodynamic Design of the 13.2 MW SUMR-13i Wind Turbine Rotor." *AIAA SciTech Forum*, 2018. doi:10.2514/6.2018-0994.

[9] Loth, E., Steele, A., Ichter, B., Selig, M. S., and Moriarty, P. Segmented Ultralight Pre - Aligned Rotor for Extreme - Scale Wind Turbines. 2012.

[10] Bay, C. J., Damiani, R., Jay Fingersh, L., Hughes, S., Chetan, M., Yao, S., Todd Griffith, D., Ananda, G. K., Selig, M. S., Zalkind, D. S., Pao, L. Y., Martin, D., Johnson, K. E., Kaminski, M., and Loth, E. "Design and Testing of a Scaled Demonstrator Turbine at the National Wind Technology Center." *AIAA Scitech Forum*, 2019.

[11] Chetan, M., Todd Griffith, D., and Yao, S. "Flutter Predictions in the Design of Extreme-Scale Segmented Ultralight Morphing Rotor Blades." doi:10.2514/6.2019-1298.

[12] GE. Haliade-X 12 MW Offshore Wind Turbine Platform. https://www.ge.com/renewableenergy/wind-energy/offshore-wind/haliade-x-offshore-turbine.

[13] Dagher, H. J., Viselli, A. M., Goupee, A. J., Kimball, R., and Allen, C. *The VulturnUS 1:8 Floating Wind Turbine*.

[14] Du, W., Zhao, Y., He, Y., and Liu, Y. "Design, Analysis and Test of a Model Turbine Blade for a Wave Basin Test of Floating Wind Turbines." *Renewable Energy*, Vol. 97, 2016, pp. 414–421. doi:10.1016/j.renene.2016.06.008.

[15] Goupee, A. J., Koo, B. J., Kimball, R. W., Lambrakos, K. F., and Dagher, H. J. "Experimental Comparison of Three Floating Wind Turbine Concepts." *Journal of Offshore Mechanics and Arctic Engineering*, Vol. 136, No. 2, 2014. doi:10.1115/1.4025804.

[16] Jonkman, J. M., Butterfield, S., Musial, W., and Scott, G. *Definition of a 5-MW Reference Wind Turbine for Offshore System Development*. 2009.

[17] Mølgaard, M., Bellew, S., and Nielsen, W. *General Rights Experimental and Theoretical Analysis of a Combined Floating Wave and Wind Energy Conversion Platform*. 2017.

[18] Kallesøe, B. S. *Aero-Hydro-Elastic Simulation Platform for Wave Energy Systems and Floating Wind Turbines*. 2011.

[19] Viselli, A. M., Goupee, A. J., and Dagher, H. J. "Model Test of a 1:8-Scale Floating Wind Turbine Offshore in the Gulf of Maine." *Journal of Offshore Mechanics and Arctic Engineering*, 2015. doi:10.1115/1.4030381.

[20] Viselli, A. M., Goupee, A. J., Dagher, H. J., and Allen, C. "Design and Model Confirmation of the Intermediate Scale VolturnUS Floating Wind Turbine Subjected to Its Extreme Design Conditions Offshore Maine." *Wind Energy*, Vol. 19, No. 6, 2016, pp. 1161–1177. doi:10.1002/we.

[21] Dagher, H., Viselli, A., Goupee, A., Kimball, R., and Allen, C. "The VolturnUS 1:8 Floating Wind Turbine: Design, Construction, Deployment, Testing, Retrieval, and Inspection of the First Grid-Connected Offshore Wind Turbine in US."

[22] Kaminski, M., Loth, E., Griffith, D. T., and Qin, C. (Chris). "Ground Testing of a 1% Gravo-Aeroelastically Scaled Additively- Manufactured Wind Turbine Blade with Bio-Inspired Structural Design." *Journal of Renewable Energy*, Vol. 148, 2020, pp. 639–650. doi:10.1016/j.renene.2019.10.152.

2. Servo-Aero-Gravo-Elastic (SAGE) Scaling of a 13-MW Downwind Turbine

Abstract:

Reduced scale wind turbines can be extremely cost-effective to test new rotor concepts since prototype costs tend to scale with the cube of the rotor diameter. Ideally, the scaled model would have the same non-dimensional deflections, dynamics, and control behavior as the full-scale model. This would provide a high-fidelity demonstration of the full-scale performance, which is ideal if the full-scale turbine has significant aeroelastic interactions. To this end, Servo-Aero-Gravo-Elastic (SAGE) scaling is developed and applied to a 13-MW turbine that is scaled to a 20% scale model. The scaling preserves the tip-speed ratio, the rotor speed normalized by the flapping frequency, and the tip deflections normalized by the blade length. In addition, the controller employs the same control structure (gain-scheduled pitch control and variable speed torque control) and is scaled dynamically (e.g. matching non-dimensional time constant of the pitch angle, etc.). Furthermore, the thrust, gravity, and centrifugal moments are scaled such that the load angles are preserved as a function of a non-dimensional wind speed. However, the aerodynamic scaling must consider differences in Reynolds number (since this parameter cannot be held constant) and subsequent changes in axial induction factor. The non-dimensional tip deflections remain comparable through all wind speed ranges indicating the viability of the SAGE scaling method.

Nomenclature

a	=	axial induction factor
c	=	chord length
c_x	=	airfoil coefficient
C_x	=	operational turbine coefficient
EI	=	blade stiffness
F	=	blade forces
Fr_{moment}	=	moment-based Froude Number
g	=	gravitational constant
k_P	=	proportional gain
k_I	=	integral gain
Lo	=	Lock Number
M	=	moment
m	=	blade mass
Ma	=	Mach number
N	=	ratio
r	=	distance
Re	=	Reynolds number
s	=	spanwise location
S	=	total blade length
U	=	wind speed
x	=	airfoil chordwise distance
y	=	distance perpendicular to chord
α	=	angle of attack
β	=	pre-cone angle
δ	=	deflection
η	=	scaling factor
λ	=	tip-speed ratio
θ	=	pitch
θ_k	=	gain-scheduling parameter
ρ	=	density
τ	=	shaft tilt
ψ	=	azimuthal angle
$\dot{\varphi}$	=	rotor speed error
Ω	=	rotational speed
ω	=	frequency
ζ	=	regulator mode damping ratio

Subscripts

$()_c$	=	centrifugal
$()_{cmd}$	=	commanded
$()_d$	=	drag
$()_f$	=	full-scale value
$()_{flap}$	=	blade structural flapwise
$()_{fine}$	=	lower limit value
$()_{gear}$	=	gearbox value
$()_{gen}$	=	generator value
$()_{hub}$	=	hub value
$()_{infinity}$	=	free stream
$()_l$	=	lift
$()_{local}$	=	local
$()_{max}$	=	maximum
$()_n$	=	regulator mode, natural
$()_p$	=	power
$()_{rated}$	=	rated value
$()_{rms}$	=	root-mean-square about mean
$()_{rot}$	=	rotating
$()_s$	=	sub-scale value
$()_t$	=	thrust
$()_{tower}$	=	tower
$()_{tip}$	=	tip value
$()_{wind}$	=	wind value
$()'$	=	spanwise distributed value
$\overline{()}$	=	non-dimensional value

2.1 Introduction

Wind energy continues to grow and be a dominant force in the renewable energy sector with wind power having dramatic additions to the United States energy market [1]. Much of this growth is associated with an increase in turbine size (to capture the higher wind conditions at higher altitudes). The subsequent increase in blade length has led to increased flexibility and aeroelastic characteristics [2]. Examples of recent extreme-scale rotor designs with such flexibility include the 13.2 MW SNL100 series [3–6] and the 13.2 MW Segmented Ultralight Morphing Rotor, denoted the SUMR-13 turbine [7–11]. These designs employ blades more than 100 meters in length providing dynamic responses, complex aerodynamics, and aeroelastics not typically seen in conventionally designed rotors. Since these designs have never been built, it is not clear to what degree current computational tools can adequately describe their behavior. Therefore, experimental results are critical for both testing and validation. To cost-effectively understand these dynamics in actual field conditions, scaled model prototypes can be designed, built, and tested prior to committing to the high cost of building the full-scale model.

A typical scaling method for the aeroelasticity and gravity effects on wind turbine blades is to use Froude scaling when going from the full-scale design to the sub-scale design [12]. However, such scaling does not take into account control characteristics nor the reduction in Reynolds number resulting in models that do not permit the sub-scale model to replicate the aerodynamics of the full-scale model [13,14].

In terms of controller scaling, it is well known that the controller architecture and parameters can substantially change the root bending moments and thus blade dynamics and deflections [15]. However, to the authors' knowledge, there are no previous studies addressing controller scaling performance for extreme-scale wind turbines using a full aeroelastic deflection case.

In terms of the Reynolds number issue, McTavis *et al.* [16] investigated wake and coefficient of thrust effects on turbines for a Reynolds number range of 10^4 to 10^5. They experimentally compared a turbine with a 1.2 meter diameter rotor (operating at a Reynolds number of 175,000) with a smaller sub-scale turbine with a 25 cm diameter rotor operating at Reynolds numbers of 29,100 and 12,800. The results showed the smallest Reynolds number sub-scale model has a coefficient of thrust that is 60% less than that of the full-scale rotor, while the moderate Reynolds number sub-scale model has a 25% deficit. Similarly, Make *et al.* [17] used simulations to investigate various sub-scale rotors with matching tip-speed ratios. The first sub-scale model was geometrically scaled while the second model was scaled to match the full-scale performance by altering the chord length, twist distribution, and distributed airfoils. The geometrically-scaled turbine yielded a 50% thrust deficit with 5 times less power due to the differences in Reynolds number and its effect on the blade lift and drag. However, these differences are lessened when employing the performance-based model. These studies show that the effects of Reynolds number when applying aeroelastic sub-scaling to a wind turbine can be important.

Another such test which applies a gravo-aeroelastic scaling approach is a 20% demonstrator of the 13.2 MW Segmented Ultralight Morphing Rotor (SUMR-13) suitable for testing at the National Wind Technology Center (NWTC) [18,19]. The test presents differences in manufacturing and site specific constraints such that while the full-scale turbine is optimized for class IIB wind speeds, the scale model is designed to withstand class IA wind speeds which contains both higher scaled wind speeds and turbulence intensity. These conditions cause the scale model to be designed with above ideal mass and stiffness distributions that therefore affect the aero-structural interactions.

The following investigation documented in this article develops an ideally scaled computational 20% model of the SUMR-13 system by placing it in an ideal environment (wind speeds and turbulence intensity) and matching the following full-scale non-dimensionalized parameters: tip-speed ratio, tip deflection relative to blade length, and rotor frequency relative to the flapping frequency. Further, a total rotational Froude number and sectional rotational Loch number are defined and held constant between sub- and full-scale systems. In addition, the non-dimensional controller performance is ideally replicated in the sub-scale system. The sub-scale demonstrator used for this study is termed herein as the Segmented Ultralight Morphing Rotor - Ideally Scaled (SUMR-IS). A consequence of the gravo-aeroelastic scaling is the mismatch of Reynolds numbers between full- and sub-scale, resulting in differences in aerodynamic performance whose effects on operation will be explored.

Thus, the goal of this study is to develop a scaling approach that can have the same non-dimensional deflections, dynamics, and control behavior to provide a high-fidelity demonstration of a full-scale turbine with significant aeroelastic behaviors. To this end, a Servo-Aero-Gravo-Elastic (SAGE) scaling approach is developed and applied to a 13-MW turbine scaled down to 20% of the full-scale dimensions. All the critical servo-gravo-aeroelastic nondimensional parameters are held constant during this scaling. For such scaling, the Reynolds number cannot be held constant, so this effect is investigated.

To the author's knowledge, this is the first study to employ a servo-aero-gravo-elastic scaling method to an extreme-scale wind turbine and the first to examine the effects of the Reynolds number mismatch. Additionally, this is the first study which explores a computationally scaled rotor which applies to each of structural components, aerodynamics, and control systems on the wind turbine. The comparison between a full-scale model and a sub-scale model is herein accomplished computationally as an experimental comparison with a full-scale 13.2 MW turbine would be extremely expensive (as will be discussed), but the results can be used to develop an experimentally scaled campaign and understand the expected effects due to Reynolds number.

This article is organized as follows. Section 2.2 explains the generalized SAGE method. Section 2.3 applies the SAGE method to the SUMR-13 turbine to define scaled geometry with influence on sectional aerodynamics as well as to scale blade mass, blade stiffness, incoming wind speeds, and controller parameters. Section 2.4 evaluates the performance of the scaling in terms of operational rotor performance and blade deflections. Finally, Section 2.5 provides concluding remarks and recommendations for future studies.

2.2 General Servo-Aero-Gravo-Elastic Scaling Methods

To create a servo-aero-gravo-elastic model, one must appropriately scale the structural, wind, and controller parameters individually. A geometric scaling factor (η) is first defined as the ratio of the full-scale blade length (S_f) to the sub-scale blade length (S_s):

$$\eta = {}^{S_s}\!/_{S_f} \tag{2.1}$$

The aforementioned scaling factor is applied to all geometric external dimensions: hub radius r_{hub}, sectional blade radius s, chord c, etc. To further ensure geometric similitude, any angle associated with the wind turbine must remain constant such as: coning angle β, shaft tilt τ, azimuthal angle Ψ, etc. as shown in Figure 1.

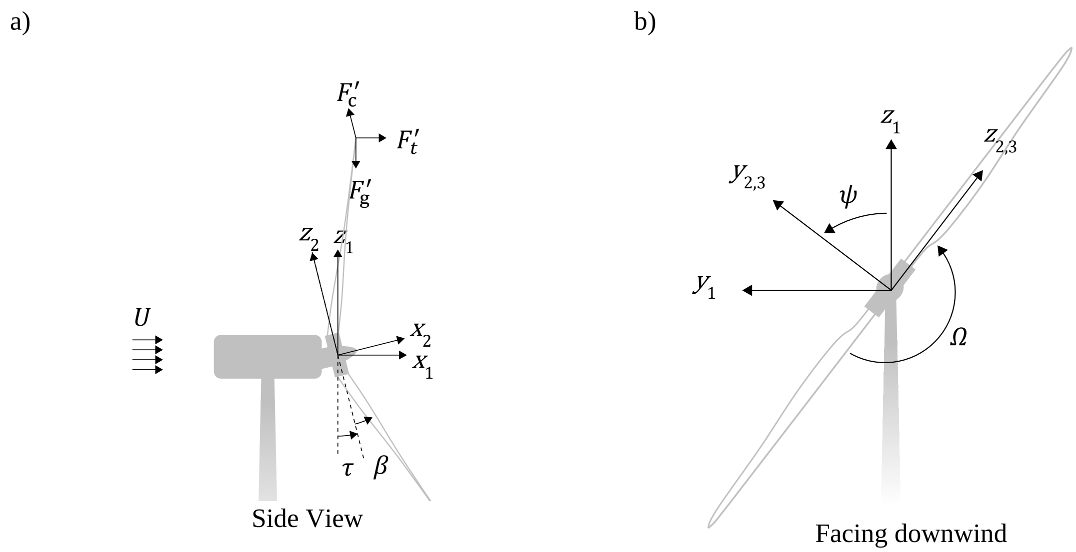

Figure 2-1: Turbine depicted from a) the side view and b) the front view facing downwind with parameters and sectional moments shown: blade pre-cone angle β, shaft tilt τ, azimuth position ψ, incoming wind speed U, sectional centrifugal force F_c', sectional thrust force F_t', and sectional gravitational force F_g'.

Next, we consider the contributions to the root flapwise bending moment (M) which are dependent on the sectional distributed forces (F), then the ratio of the centrifugal component (M_c) to the gravitational component (M_g) can be employed for scaling. The ratio of centrifugal to gravitational moments is expressed herein based on the acceleration due to gravity (g) acting on the blade pointed upwards ($\psi = 0$) per Figure 2-1:

$$ {}^{M_c}\!/_{M_g} = \frac{\Omega^2 (r_{\mathrm{hub}} + S\cos\beta)\sin\beta}{g\,(\cos\beta\sin\tau - \sin\beta\cos\tau)} \tag{2.2}$$

The right-hand-side of this equation is derived in terms of coning and shaft tilt angles and integrated along the span. Holding this moment ratio fixed ensures that the load angles associated with the combination of the gravity and centrifugal effects on the blades will be preserved as a function of the azimuth angular position ψ. If the shaft tilt and coning angle are preserved, then keeping the moment ratio fixed requires that $\Omega^2 S/g$ is preserved, which can be defined as a rotational Froude number (Fr_{rot}). Note this differs from a Froude number (ratio of inertial and gravitational forces) due to the rotational Froude number being a ratio of centrifugal and gravitational moments.

$$Fr_{\mathrm{rot}} = \frac{\Omega^2 S}{g} = {M_c}/{M_g} \tag{2.3}$$

Th relationship between centrifugal and gravitational moments dictates the rotational speed scaling which is shown as follows:

$$\frac{\Omega_{\mathrm{s}}}{\Omega_{\mathrm{f}}} = 1/\sqrt{\eta} \tag{2.4}$$

Fixing the tip-speed ratio preserves the flow angles and dynamics. Applying appropriate length and rotational speed scaling to the fixed tip-speed ratio, the upstream wind speed *(U)* scaling can be found. The following defines the tip-speed ratio (λ) and the wind speed scaling.

$$\lambda = \frac{\Omega(r_{\mathrm{hub}} + S\cos\beta)}{U} \tag{2.5}$$

$$\frac{U_{\mathrm{s}}}{U_{\mathrm{f}}} = \sqrt{\eta} \tag{2.6}$$

Given that time scales (t) will be proportional to the ratio of the length to the velocity scales, this indicates the dynamics in the sub-scale time variation must be scaled as seen as follows.

$$\frac{t_{\mathrm{s}}}{t_{\mathrm{f}}} = \sqrt{\eta} \tag{2.7}$$

Next, one should consider the influence of the thrust component, by taking the ratio of the centrifugal component (M_{c}') of the flapwise bending moment relative to the thrust component (M_{t}'):

$$M'_c/M'_t = \frac{-m'\Omega^2(r_{\mathrm{hub}} + s\cos\beta)\sin\ \beta}{\frac{1}{2}\rho_{\mathrm{wind}} c_{\mathrm{t}} c(U_{\mathrm{rated}}^2 + [\Omega\{r_{\mathrm{hub}} + s\cos(\beta - \tau)\}]^2) * (\cos\tau\cos\beta - \sin\tau\cos\psi\sin\beta)} \tag{2.8}$$

Equation (2.8) is simplified and defined as the sectional rotational Lock number by retaining the structural angles, applying the geometric scaling, and keeping the tip-speed ratio constant. Note this differs from a Lock number (ratio of aerodynamic and inertial loads of a full blade) as it is a ratio of centrifugal and aerodynamic loads for a section of the blade:

$$Lo_{\mathrm{rot}}{}' = \frac{m'\Omega^2}{\rho_{\mathrm{wind}} c_{\mathrm{t}} U_{\mathrm{rated}}^2} \tag{2.9}$$

Retaining equation (2.9) and applying an assumption of constant coefficient of thrust, the sectional blade mass density is found to scale with the ratio of the air densities and η^2. Integrating these sectional values along the span of the blade leads to the total blade mass scaling. The sectional and total blade mass scale as follows:

$$m'_{\mathrm{s}}/m'_{\mathrm{f}} = \left(\frac{\rho_{\mathrm{wind,s}}}{\rho_{\mathrm{wind,f}}}\right)\eta^2 \tag{2.10}$$

$$m_{\mathrm{s}}/m_{\mathrm{f}} = \left(\frac{\rho_{\mathrm{wind,s}}}{\rho_{\mathrm{wind,f}}}\right)\eta^3 \tag{2.11}$$

Based on the above, the scaling definitions for the three base units (length, time, and mass) are each summarized in Table 2-1 [20].

Table 2-1: Base unit scaling for a servo-aero-gravo-elastic model

Base Units, SI Units	Scale Factor
Length, *m*	η
Time, *s*	$\sqrt{\eta}$
Mass, *kg*	$\left(\frac{\rho_{\text{wind,s}}}{\rho_{\text{wind,f}}}\right)\eta^3$

Each of these base units can be applied to rotor parameters with combined units to determine how each of the individual parameters should scale. As an example, the units of blade stiffness per unit span (*EI'*) are defined as $\frac{kg*m^3}{s^2}$ which has units of $\frac{[\text{mass}]*[\text{length}]^3}{[\text{time}]^2}$. Employing Table 2-1, the scaling factor for the stiffness is given in Table 2-2, along with the other significant structural and aerodynamic parameters. It should be noted that a scaled blade can be conceptually designed and fabricated to match all these parameters except that of Reynolds number and Mach number. A complete list of scaling of parameters is found in Appendix A.

Table 2-2: Summary of the structural and aerodynamic scaling parameters in terms of the length scaling parameter η.

Scaling Parameter	Scale Factor
Length Scaling: $\frac{\boldsymbol{S_s}}{\boldsymbol{S_f}}$	η
Rotational Scaling: $\frac{\Omega_s}{\Omega_f}$	$1/\sqrt{\eta}$
Wind Velocity Scaling: $\frac{\boldsymbol{U_s}}{\boldsymbol{U_f}}$	$\sqrt{\eta}$
Total Blade Mass Scaling: $\frac{\boldsymbol{m_s}}{\boldsymbol{m_f}}$	$\left(\frac{\rho_{\text{wind,s}}}{\rho_{\text{wind,f}}}\right)\eta^3$
Flap-wise Frequency Scaling: $\frac{\boldsymbol{\omega_{\text{flap, s}}}}{\boldsymbol{\omega_{\text{flap, f}}}}$	$1/\sqrt{\eta}$
Stiffness Scaling: $\frac{(\boldsymbol{EI'})_s}{(\boldsymbol{EI'})_f}$	$\left(\frac{\rho_{\text{wind,s}}}{\rho_{\text{wind,f}}}\right)\eta^5$
Reynolds Number Ratio: $\frac{\boldsymbol{Re_s}}{\boldsymbol{Re_f}}$	$\left(\frac{\rho_{\text{wind,s}}}{\rho_{\text{wind,f}}}\right)\left(\frac{\mu_{\text{wind,f}}}{\mu_{\text{wind,s}}}\right)\eta^{3/2}$
Mach Number Ratio: $\frac{\boldsymbol{Ma_s}}{\boldsymbol{Ma_f}}$	$\left(\frac{a_{\text{wind,f}}}{a_{\text{wind,s}}}\right)\sqrt{\eta}$

Beyond the structural and aerodynamic parameters, the controller must also scale appropriately. The structure of the control system is consistent from full- to sub-scale i.e. the full-scale and scale systems both contain a gain-scheduled proportional-integral pitch control and a variable-speed torque controller similar to that of the NREL-5MW reference controller [21]. As mentioned, it is important to maintain the tip-speed ratio (λ) defined in equation (2.5) and the non-dimensional rotational rate frequency ($\overline{\Omega_{\text{flap}}}$) in order to retain consistent flow angles over the blade as well as maintain the input to output frequencies of the rotor (blade natural frequency to the rotational frequency).

$$\overline{\Omega_{\text{flap}}} = \frac{\Omega}{\omega_{\text{flap}}} \tag{2.12}$$

The pitch control dynamics directly affect flap-wise loading [22–25], so the pitch response of the rotor (to an incoming wind gust) must be consistent between the full- and sub-scale rotor models. The pitch angle (θ) control is a commonly-used gain-scheduled, proportional-integral control law [21,26], defined by:

$$\theta_{\text{cmd}} = GK(\theta)\left[k_{\text{P}} N_{\text{gear}}(\Omega - \Omega_{\text{rated}}) + k_{\text{I}} N_{\text{gear}} \int (\Omega - \Omega_{\text{rated}}) dt\right] \quad (2.13)$$

where k_{P} and k_{I} are the proportional and integral gains, Ω is the rotor speed, N_{gear} is the gearbox ratio, and Ω_{rated} is the rated speed. The gain-scheduling term

$$GK(\theta) = \frac{1}{1 + \frac{\theta}{\theta_{\text{k}}}} \quad (2.14)$$

accounts for aerodynamic non-linearities and depends on the blade pitch θ and the gain scheduling parameter θ_{k}. The blade pitch command in equation (2.13) is saturated at a lower limit of θ_{fine}, the aerodynamically optimal pitch angle. When a rigid body rotor model is combined with the PI control in (2.13), the dynamics of the generator speed error can be represented by a second order system [21]

$$\ddot{\varphi}_{\Omega} + 2\zeta\omega_n\dot{\varphi}_{\Omega} + \omega_n^2\varphi_{\Omega} = 0 \quad (2.15)$$

Which is similar to the dynamics of the pitch response because $\dot{\varphi}_{\Omega} = \Omega - \Omega_{\text{rated}}$ and the pitch command in equation (2.13) is a linear combination of φ_{Ω} and its derivatives.

The pitch response is made consistent by matching the non-dimensional time constant of the pitch angle, or the time it takes the pitch to transition 63% of the difference between the initial and final values during a step increase in wind speed. The time constants are a result of scaling the regulator mode natural frequency (ω_{n}) as defined in Table 2-3. Using the base unit scaling of Table 2-1, the expected time constants should scale with $\sqrt{\eta}$. By matching the time constants due to a deterministic step increase in wind speed it is expected that the dynamics of the sub-scale system will match the full-scale system during turbulent conditions as well.

Table 2-3: Dimensional controller scaling parameters for a servo-aero-gravo-elastic model.

Scaling Parameter	Scale Factor
Time Constant, t_{const}	$\sqrt{\eta}$
Pitch Control Natural Frequency, ω_n	$1/\sqrt{\eta}$
Gain Scheduling Parameter, θ_{k}	(-)
Damping Ratio, ζ	(-)

The turbine is tested using FAST, an aeroelastic simulation tool that uses blade element momentum theory [17,27]. The 2-dimensional aerodynamic parameter files will be presented showing the coefficient of lift (c_l) and coefficient of drag (c_d) versus the airfoil angle of attack (α) at 66% span at the two different Reynolds numbers. The 66% span location is used as this is near where the effective radius for the thrust moment is typically located.

The appropriate structural, wind speed, controller, and two-dimensional aerodynamic parameter files will be used to return the 3-dimensional results via simulation. These results will display the differences due to Reynolds number in both steady and turbulent conditions.

2.3 Scaling Applied to an Extreme-Scale Turbine

2.3.1 Scaling Summary

The overall scaling is summarized in Table 4 where the turbine utilized for the full-scale model is the SUMR-13 rotor with 104.36 meter blades and a tower height of 142.4 meters. The resulting sub-scale rotor has blade lengths of 20.87 meters and a tower height of 28.48 meters. This scaling leads to a blade mass more than 150 times lighter in mass. The reduction in rotor area and rated wind speeds leads to dramatic reduction in rated power (a reduction of nearly 300-fold). As such, the overall cost reduction to fabricate the SUMR-IS compared to SUMR-13 may be expected to be in this same range of reduction. It is important to note the changes in Reynolds number between the two scales, which can have an impact in terms of aerodynamic performance. Similarly, there are differences in Mach number due to the wind-air speed of sound remaining constant between the two scales. However, these are expected to have minimal effect on turbine performance given that the Mach numbers are low enough that compressibility effects are weak. As such, the Reynolds number represents a parameters that cannot be scaled for field-tested wind turbines with significantly different sizes

Table 2-4: Summarizing parameters of the SUMR-13 rotor and the servo-aero-gravo-elastically scaled SUMR-IS rotor to investigate differences associated with Reynolds number effects.

	SUMR-13	SUMR-IS
Design Innovation	Extreme-Scale	Extreme-Scale
Length Scaling Factor (η)	1	0.2
Blade Length (S)	104.36 m	20.87 m
Hub Radius (l_{hub})	2.5 m	0.5 m
Tower Height (l_{tower})	142.4 m	28.48 m
Coning Angle (β)	Variable	12.5 degrees
Tip-Speed Ratio (λ)	9.5	9.5
Rated Turbine Power (P_{rated})	13.2 MW	47 kW
Rated Wind Speed (U_{rated})	11.3 m/s	5.05 m/s
Rated Rotor Speed (Ω_{rated})	9.82 rpm	21.96 rpm
Pitch Saturation (θ)	0.48 degrees	0.48 degrees
Blade Mass (m)	54787.4 kg	350.64 kg
Flapping Frequency (ω_{flap}) at Ω_{rat}	0.69 Hz	1.53 Hz
Reynolds Number at 66% Span (Re)	1.63E7	1.16E6
Ref. Mach Number at 66% Span (Ma)	0.227	0.101

2.3.2 Rotor Airfoil Shapes and Sectional Aerodynamics

The full-scale rotor used for the current SAGE model is the 13.2-MW Segmented Ultralight Morphing Rotor (SUMR-13) [7–11]. SUMR-13 rotor is a 2-bladed downwind morphing rotor with blade lengths reaching to 104.4 meters in length. Select airfoils distributed down the length of the blades are shown in Figure 2-2. Adjacent airfoils are used to define additional airfoils at intermediate locations. The SUMR-13 turbine represents a class of turbine blades denoted extreme-scale wind turbine blades which, along with having excessive length, are highly flexible causing additional dynamics not represented in conventional wind turbine blades. The SUMR-IS turbine employs similar geometric properties as the SUMR-13 turbine including the airfoil distribution in Figure 2-2, the non-dimensional chord distribution, and the twist distribution. However, it has an aerodynamic performance based on the Reynolds numbers (as will be discussed later).

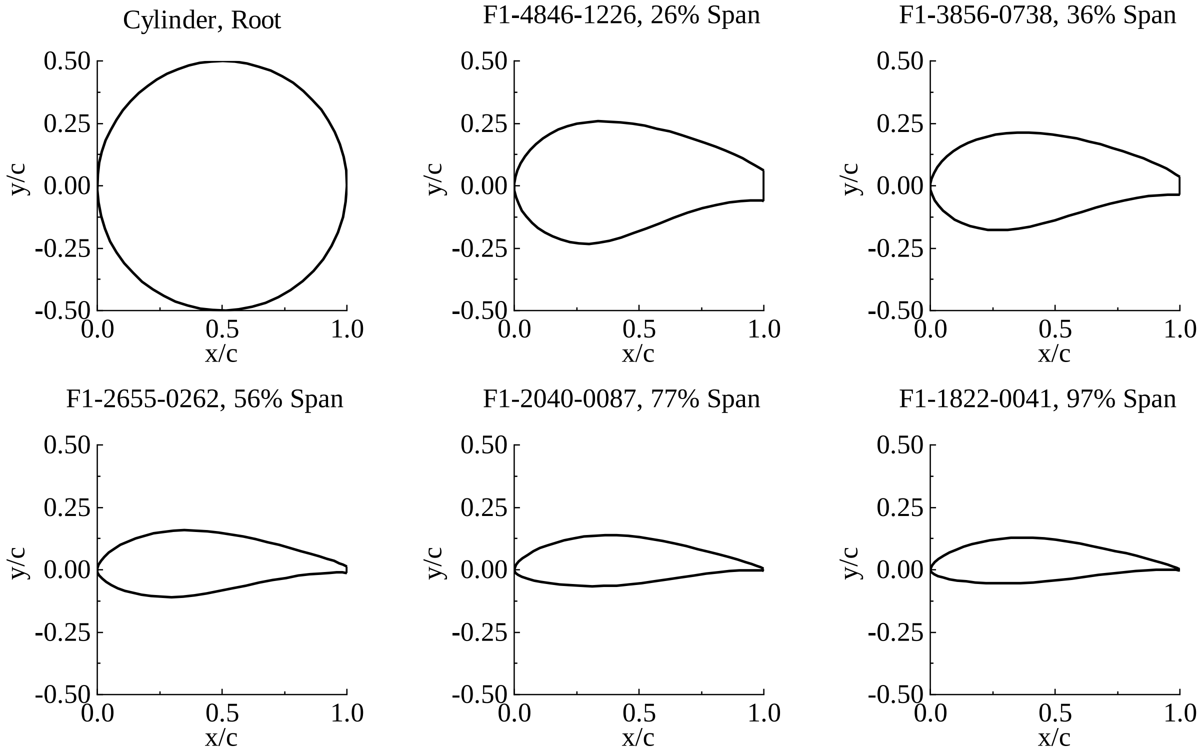

Figure 2-2: Airfoil distribution of the SUMR-13 rotor and the SUMR-IS rotor shown non-dimensionally by the chord length *c*, the distance along the chord *x*, the distance perpendicular to the chord *y*. Each blade employs the same non-dimensional chord and twist distributions.

While the SUMR-IS employs geometric similitude (as shown) as well as properly scale frequencies, controllers, stiffness, and mass distribution (as discussed below), the aerodynamic performance will not scale properly. In particular, differences in Reynolds numbers will cause the airfoil lift and drag (as a function of angle of attack) to be modified. These difference are used by FAST and are based on data synthesized between experiments and XFOIL [28]. Shown in Figure 2-3 are the coefficients of lift and drag as a function of angle of attack for an airfoil at 66% span. The airfoil utilized is a blend between the 56% and 77% span airfoils found in Figure 2-2. The SUMR-13 rotor operates at a higher Reynolds number than that of the SUMR-IS turbine causing a decrease in lift as well as an increase in drag which holds true for all airfoils along the blade span. Therefore, in operation, the entire blade will experience a decrease in lift and an increase in drag if the two blades are operating the same AOA.

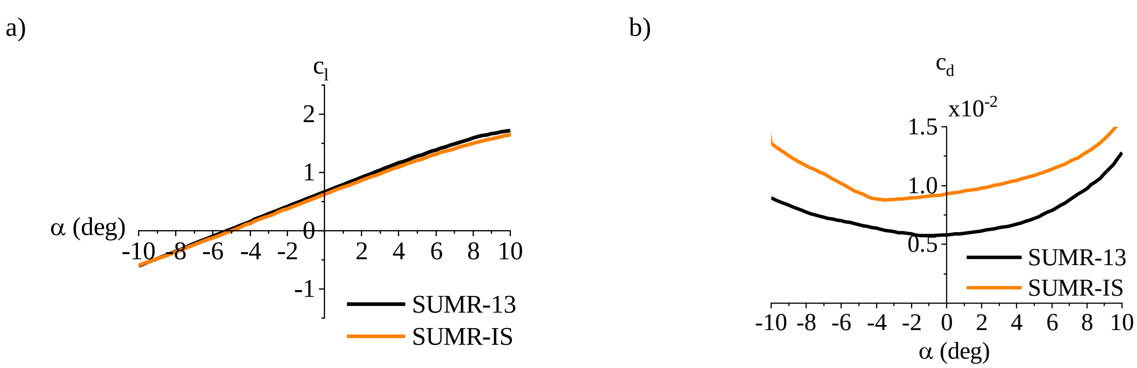

Figure 2-3: The a) coefficients of lift (c_l) and b) coefficients of drag (c_d) vs. airfoil angle of attack (α) for the full-scale SUMR-13 rotor and the Ideally Scaled SUMR-IS turbine for an airfoil at 66% span.

2.3.3 *Blade Mass and Stiffness Distributions*

Based on Table 2, the flapwise sectional properties of stiffness (EI') and mass density (m') are non-dimensionally matched in equations (2.16)-(2.18) where the overbar ($\bar{\ }$) represents non-dimensional values. Their values are presented in Figure 2-4 as a function of the non-dimensional spanwise location.

$$\bar{s} = {}^{s}/_{S} \tag{2.16}$$

$$\overline{EI'} = {}^{EI'}/_{\rho_{\text{wind}} g S^5} \tag{2.17}$$

$$\overline{m'} = {}^{m'}/_{\rho_{\text{wind}} S^2} \tag{2.18}$$

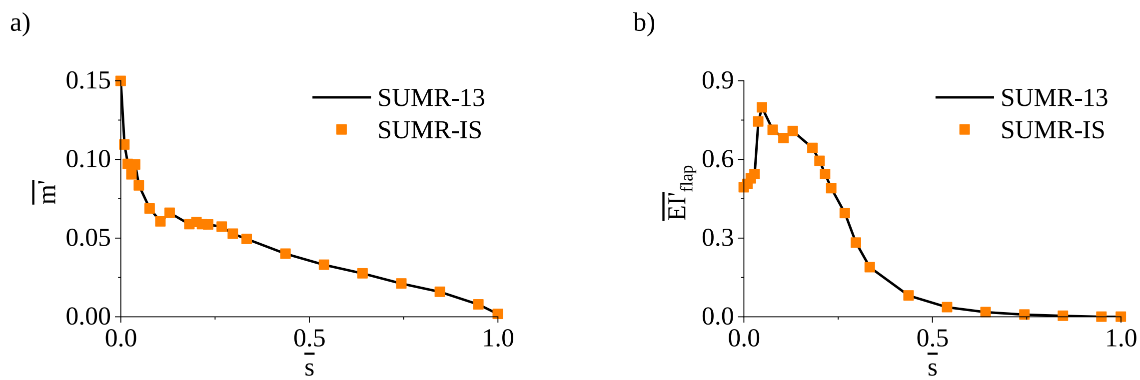

Figure 2-4: Select non-dimensional distributed blade structural parameters showing a) mass density ($\overline{m'}$) and b) stiffness ($\overline{EI'}$) for the SUMR-13 blade and the ideally scaled SUMR-IS blade.

2.3.4 *Empirically Scaled Controller and Scaled Wind Speeds*

To verify the controller scaling, a non-dimensional step input of wind speeds is applied to each turbine in order to check the non-dimensional time constant of the pitch angle in response to a step change in wind speed. A non-dimensional wind input step size of 0.265 will be applied to starting non-dimensional wind speeds of 1.327 and 1.77, i.e., 33% and 77% above rated. The non-dimensional wind speed values utilize equation (2.19) and are plotted against non-dimensional time of equation (2.20) in Figure 2-5. These values are chosen in order to provide a full-range of above-rated operating conditions.

$$\bar{U} = {}^{U}/_{U_{\text{rated}}} \tag{2.19}$$

$$\bar{t} = t * {}^{g}/_{U_{\text{rated}}} \tag{2.20}$$

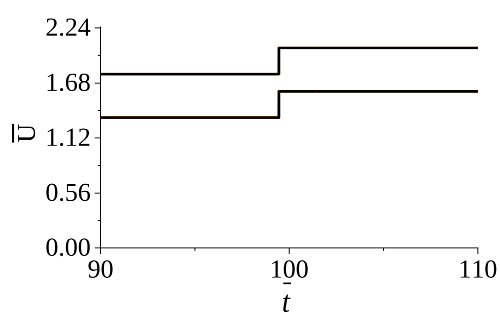

Figure 2-5: Two non-dimensional input wind speeds spanning the Region 3 operating regime for verifying the controller scaling performance.

The controller variables are then scaled as stated in Table 2-3 with the resulting parameters summarized in Table 2-5. Table 2-5 additionally contains the non-dimensional time constant of the pitch angle (time for pitch to reach 63% of its final pitch) for the SUMR-13 and the SUMR-IS controllers. The pitch angle as a result of the step changes in wind speed can also be seen in Figure 2-6 where there is a ~5.5% error in the non-dimensional time constant. The error in time constant can be attributed to the assumption of a rigid body rotor model used for equation (2.15). The results of Figure 2-6 indicate that there can be small controller differences in addition to the effects of Reynolds number. In general, the controller for the SUMR-IS in terms of pitch response to this discontinuous velocity shift is about 5-10% less responsive that that of the SUMR-13 in terms of non-dimensional time response.

Table 2-5: Summarizing parameters of the SUMR-13 and SUMR-IS (with adjusted controllers) with their respective non-dimensional time constants due to a non-dimensional step steady-state wind speed input.

	Ω_n (rad/s)	ξ (-)	$\bar{t}_{\mathrm{const}}$	
Non-Dimensional Wind Speed Range	(-)	(-)	1.38-1.59	1.77-2.04
SUMR-13	0.1415	1.35	5.31	7.10
SUMR-IS	0.316	1.35	5.60	7.47

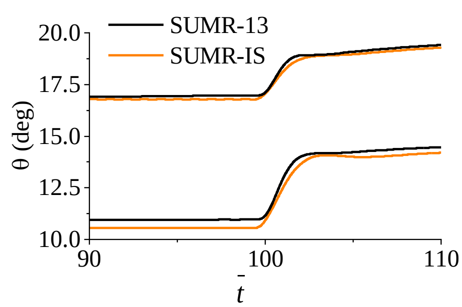

Figure 2-6: Comparison of the ideally scaled controller pitch (θ) over a non-dimensional time subjected to two separate step input wind speeds as specified in Figure 5 which span the Region 3 operating regime.

For a final scaling check, we consider the wind speeds. Since the turbines are tested in turbulent conditions, it is important to ensure that the scaled mean and fluctuation inflow parameters are preserved. The scaling of the wind input is compared by plotting the non-dimensional wind speed at hub height against the non-dimensional time in Figure 2-7. While instantaneous values are different, the mean and standard deviations are nearly identical.

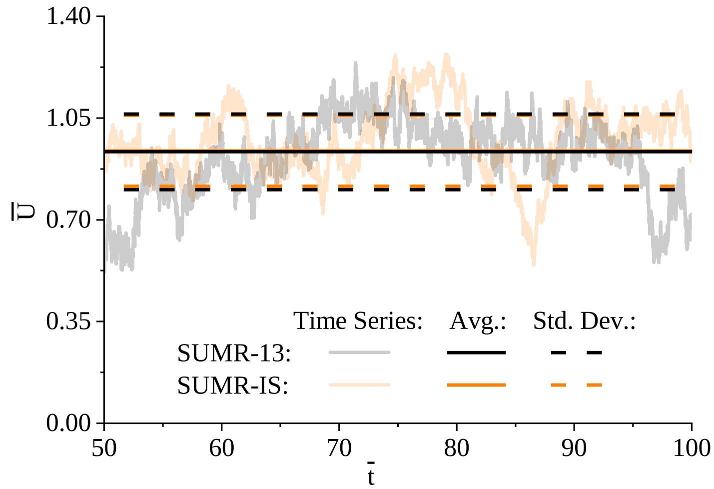

Figure 2-7: Non-dimensional wind input ($\overline{U}$) with average (solid line) and standard deviation (dashed line) shown as a function of non-dimensional time ($\bar{t}$) for computational simulations

2.4 Operational Results of Scaled Turbine

2.4.1 Rotor Aerodynamic Performance

The reduction in Reynolds number on the appropriately scaled 2-Dimensional airfoils leads to a slight decrease in lift and a large increase in drag for the same operating angle of attack as shown in Figure 2-3. As summarized in Section 2.3, the turbine saturates the blade pitch at its lower limit in below-rated conditions to maximize power capture and regulates power production in above-rated conditions by regulating rotor speed. The relationship between the turbine coefficient of power and the coefficients of lift and drag are shown in equation (2.21) and the subsequent relationship between the coefficient of power and axial induction factor are shown in equation (2.22) [29].

$$C_{\mathrm{p}} = C_l\sqrt{1+\lambda^2}\left(\lambda - \frac{C_{\mathrm{d}}}{C_{\mathrm{l}}}\lambda^2\right) \tag{2.21}$$

$$C_{\mathrm{p}} = 4a(1-a)^2 \tag{2.22}$$

The relationship shown in equation (2.21) includes the turbine tip-speed ratio λ. The tip-speed ratio is maintained through scaling in Figure 2-8a but the slight reduction in coefficient of lift and a significant increase in coefficient of drag due to Reynolds numbers differences. These differences cause the axial induction factor to substantially decrease for the outboard regions as seen in Figure 2-8b for Region 2 operations.

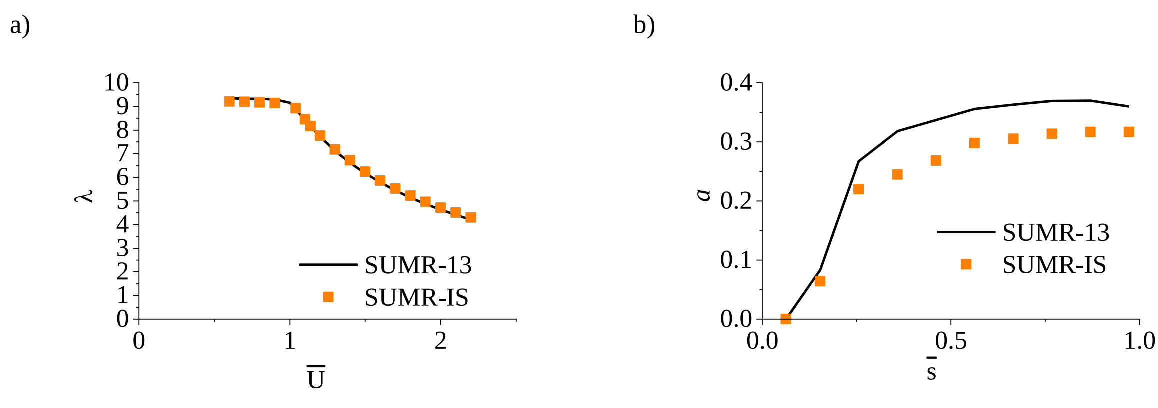

Figure 2-8: Computational results of a) the tip-speed ratio over the entire range of operating conditions and b) the turbine axial induction factor in below rated conditions where $\overline{U} = 0.7$ over the span of the blade.

With the SUMR-13 rotor is designed to operate at maximum coefficient of power. This maximum value is reduced in Region 2 due to the reduction in the axial induction factor as seen in Figure 2-9.

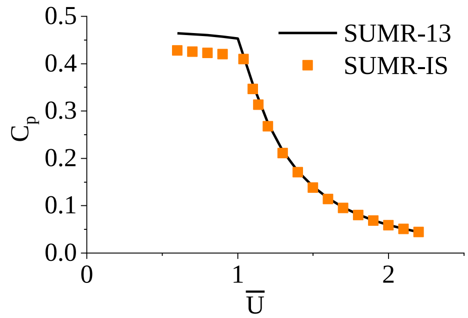

Figure 2-9: The turbine coefficient of power (C_p) over the entire range of operating conditions with a reduction in maximum C_p in Region 2 due to the reduction in axial induction factor.

A summary of the influence of the Reynolds number difference is depicted in Figure 2-10 and seen in below-rated conditions. When scaling down the turbine, the Reynolds number decreases, which leads to a decrease in the lift and an increase in the drag of the blade airfoils. These two-dimensional aerodynamic effects then result in a reduction in the axial induction factor due to the reduction in torque, thus reducing the turbine coefficient of power. These aerodynamic changes lead to operational changes in the turbines as will be discussed in Section 2.4.2.

Reynolds Number Effects

↓

Decrease in Airfoil Lift, Increase in Airfoil Drag

↓

Decrease in Axial Induction Factor

↓

$C_{p,max}$ Reduction

Figure 2-10: Influence of the effects of Reynolds number on sub-scale turbine aerodynamics

2.4.2 Operational Results

As previously stated through controller scaling and equations (2.5) and (2.12), it is important to match the tip-speed ratio as well as the non-dimensional rotational rate despite the aerodynamic alterations stated in Section 2.4.1. Matching the tip-speed ratio helps to approximately keep the flow angles over the rotor consistent. An exact match in flow angles over the blade can occur so long as the pitch and axial induction factors remain constant between full- and sub-scale. Matching the non-dimensional rotational rate ensures the resonant conditions which occur at the full-scale also occur at the sub-scale. The matching tip-speed ration can be seen in Figure 2-8a and the matching non-dimensional rotational rate over a range of wind speeds is seen in Figure 2-11. As expected, both the tip-speed ratio and non-dimensional rotational rate match over the entire range of wind speeds.

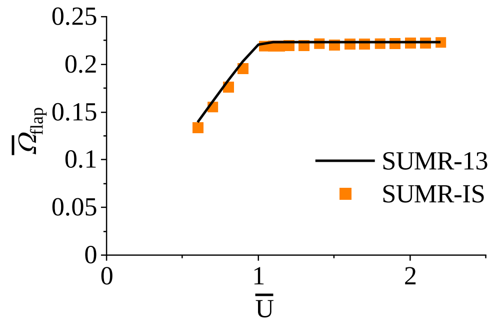

Figure 2-11: The steady non-dimensional rotational rate ($\bar{\Omega}_{\text{flap}}$) over the range of operating wind speeds.

The resulting pitch over a range of wind speeds is depicted in Figure 2-12a. The values match well for the below-rated conditions and are within 10% for above rated conditions due to the system pitching to obtain more power make up for the higher drag and lower lift due to Reynolds numbers differences.

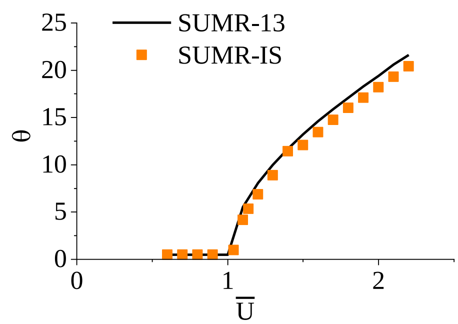

Figure 2-12: The blade pitch (θ) over a range of operational steady wind speeds.

To determine how well the scaling performs, the mean and fluctuating values of the normalized flapwise tip deflections are given in equations (2.23) and (2.24). Such deflections stem directly from the flapwise bending moments, the blade mass and stiffness distributions, and the pitch controller. In addition, these deflections directly indicate the degree of scaling for aeroelastic behaviors.

$$\overline{\delta_{\text{tip}}} = {\delta_{\text{tip}}}/{S} \tag{2.23}$$

$$\overline{\delta_{\text{tip,rms}}} = {\delta_{\text{tip,rms}}}/{S} \tag{2.24}$$

While there are significant aerodynamic changes in a sub-scale rotor, a SAGE scaled rotor aims to ensure the aeroelastic interactions remain proper. As such, Figure 2-13 presents the tip deflections for both the steady and turbulent conditions. Presented are the mean tip deflections as well as the root-mean-square of tip deflections about the mean. Each case presents below ideal deflections in below-rated conditions and above ideal conditions in above-rated conditions. The differences in tip deflection can be attributed to Reynolds effects as well as controller structure differences between below-rated and above-rated. While each mean is slightly different, there is significant overlap of the RMS about the mean, and the resultant tip deflections are reasonably accurate despite the significant changes in Reynolds number.

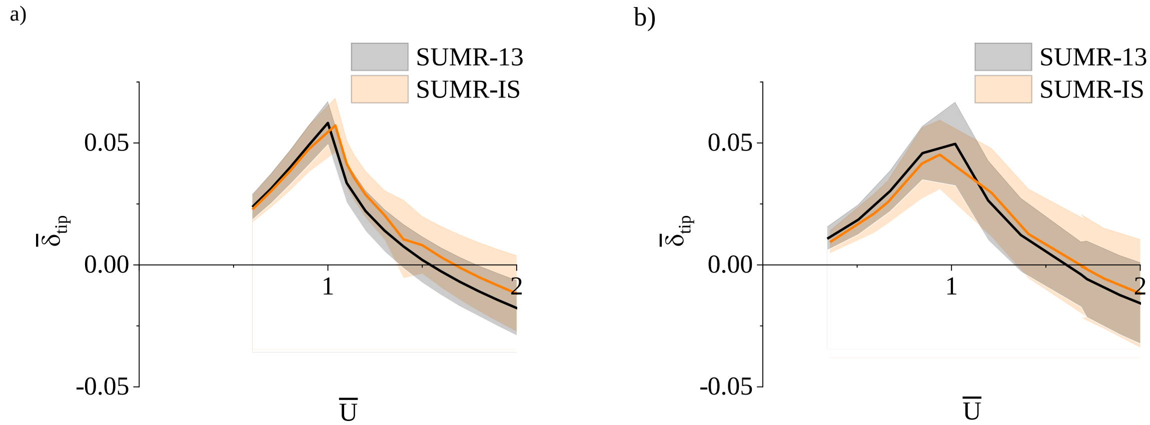

Figure 2-13: 11 simulations run in a) steady conditions and b) turbulent conditions showing the non-dimensional tip deflections ($\bar{\delta}_{tip}$) through the entire range of wind speeds with solid lines representing the average and shaded regions representing the standard deviation.

These results indicate that the inability to match the Reynolds (and the associated reduction in induction factors at the sub-scale) does not significantly limit the ability to match the aeroelastic deflections for a scaling of 20% on a 13 MW highly flexible downwind turbine when employing the SAGE method. This is a strong endorsement for employing sub-scale systems to experimentally study the aeroelastic performance of extreme-scale wind turbine rotor concepts with appropriate servo-gravo-aeroelastic scaling. This is particularly true as the cost of building and testing a research turbine tends to scale with the generated power as well as the rotor mass, and a 20% scale turbine has a power rating reduction of more than three orders of magnitude and a mass reduction of 150-fold. The cost savings for a sub-scale turbine may therefore be at least 150-fold. To verify the performance shown in Figure 2-13, it is recommended that this approach be assessed by comparing SAGE-based field tests of a full-scale and sub-scale turbine, especially for a lightweight rotor with high flexibility (as is the current trend for extreme-scale rotors) where the load paths tend to significantly deviate from the centrifugally-dominated radial direction. This could be accomplished by employing one of the recent production-level extreme-scale turbines for the full-scale system [30,31].

Further computational work can be conducted to further examine the effects of Reynolds number by retaining the exact control set points (pitch, non-dimensional rpm, etc.) in reference to a non-dimensional free-stream wind speed. Retaining the control set points will help differentiate between the differences due to aerodynamics and subsequent controls. Additionally, it is suggested to adjust the controller in order to preserve the operational tip deflections of the sub-scale rotor as compared to the full-scale rotor to retain a SAGE scaled rotor.

2.5 Conclusions and Recommendations

The current study presents an ideal 20% model of a 13.2-MW turbine (SUMR-13) using a servo-aero-gravo-elastic scaling method in order to retain the controller, aerodynamic, and gravitational interactions. The SAGE method aims to match operational conditions by matching the non-dimensional mean wind speeds and their standard deviations. Additionally, the controller is scaled such that the control structure (gain-scheduled, proportional-integral pitch control and variable speed torque control) and the non-dimensional time constant of the pitch control remains constant. Additionally, structural components (blade, tower, hub, etc.) are appropriately scaled such that the non-dimensional structural properties are matched by defining base unit scaling and applying these scalings to the units of a property. Overall, the goal of SAGE scaling is to match the tip-speed ratio, the rotor speed normalized by the flapping frequency, and the average tip deflections during operation normalized by the blade length.

A drawback of the SAGE scaling method is a difference in the Reynolds number affecting the aerodynamics, which subsequently changes the axial induction factor. Despite the altered aerodynamic properties, the turbine was able to portray non-dimensional tip deflections similar to the full-scale model which, as previously stated, is a primary goal of the SAGE scaling method. This indicates the high potential value of employing sub-scale systems to experimentally study the aeroelastic performance of extreme-scale wind turbine rotor concepts with appropriate servo-gravo-aeroelastic scaling. Field testing is recommended to confirm the quantitative efficacy of this scaling methodology. In addition, further work can be conducted computationally to further examine the effects of Reynolds number by retaining the exact control set points in reference to a non-dimensional free stream wind speed to adjust the controller in order to preserve the operational tip deflections of the sub-scale rotor as compared to the full-scale rotor to retain a SAGE scaled rotor.

References

[1] Wiser, R., Bolinger, M., Barbose, G., Darghouth, N., Hoen, B., Mills, A., Rand, J., Millstein, D., Jeong, S., Porter, K., Disanti, N., and Oteri, F. *2018 Wind Technologies Market Report*. 2018.

[2] Bir, G., and Jonkman, J. M. "Aeroelastic Instabilities of Large Offshore and Onshore Wind Turbinesa." *Journal of Physics*, Vol. 75, 2007.

[3] Griffith, D. T., and Ashwill, T. D. *The Sandia 100-Meter All-Glass Baseline Wind Turbine Blade : SNL100-00*. 2011.

[4] Griffith, D. T. *The SNL100-01 Blade: Carbon Design Studies for the Sandia 100-Meter Blade*. 2013.

[5] Griffith, D. T. *The SNL100-02 Blade : Advanced Core Material Design Studies for the Sandia 100- Meter Blade*. 2013.

[6] Griffith, D. T., and Richards, P. W. *The SNL100-03 Blade : Design Studies with Flatback Airfoils for the Sandia 100-Meter Blade*. 2014.

[7] Ananda, G. K., Bansal, S., and Selig, M. S. "Aerodynamic Design of the 13.2 MW SUMR-13i Wind Turbine Rotor." *AIAA SciTech Forum*, 2018. doi:10.2514/6.2018-0994.

[8] Loth, E., Selig, M. S., and Moriarty, P. "Morphing Segmented Wind Turbine Concept." *AIAA Applied Aerodynamics Conference*, No. July, 2010, pp. 1–6. doi:10.2514/6.2010-4400.

[9] Loth, E., Steele, A., Ichter, B., Selig, M. S., and Moriarty, P. Segmented Ultralight Pre - Aligned Rotor for Extreme - Scale Wind Turbines. 2012.

[10] Noyes, C., Qin, C., and Loth, E. Ultralight, Morphing Rotor for Extreme-Scale Wind Turbines. 2017.

[11] Noyes, C., Qin, C., and Loth, E. "Pre-Aligned Downwind Rotor for a 13.2 MW Wind Turbine." *Renewable Energy*, Vol. 116, 2018, pp. 749–754. doi:10.1016/j.renene.2017.10.019.

[12] Kaminski, M., Loth, E., Griffith, D. T., and Qin, C. (Chris). "Ground Testing of a 1% Gravo-Aeroelastically Scaled Additively- Manufactured Wind Turbine Blade with Bio-Inspired Structural Design." *Journal of Renewable Energy*, Vol. 148, 2020, pp. 639–650. doi:10.1016/j.renene.2019.10.152.

[13] Bottasso, C. L., Campagnolo, F., and Petrović, V. "Wind Tunnel Testing of Scaled Wind Turbine Models: Beyond Aerodynamics." *Journal of Wind Engineering and Industrial Aerodynamics*, Vol. 127, 2014, pp. 11–28. doi:10.1016/j.jweia.2014.01.009.

[14] Bayati, I., Belloli, M., Bernini, L., and Zasso, A. "Aerodynamic Design Methodology for Wind Tunnel Tests of Wind Turbine Rotors." *Journal of Wind Engineering and Industrial Aerodynamics*, Vol. 167, 2017, pp. 217–227. doi:10.1016/j.jweia.2017.05.004.

[15] Martin, D. P., Johnson, K. E., Zalkind, D. S., and Pao, L. Y. "LPV-Based Torque Control for an Extreme-Scale Morphing Wind Turbine Rotor." *Proceedings of the American Control Conference*, 2017, pp. 1383–1388. doi:10.23919/ACC.2017.7963146.

[16] McTavish, S., Feszty, D., and Nitzsche, F. "Evaluating Reynolds Number Effects in Small-Scale Wind Turbine Experiments." *Journal of Wind Engineering and Industrial Aerodynamics*, 2013. doi:10.1016/j.jweia.2013.07.006.

[17] Make, M., and Vaz, G. Analyzing Scaling Effects on Offshore Wind Turbines Using CFD. Renewable Energy, 83, 2015, pp. 1326–1340.

[18] Yao, S., Griffith, D. T., Chetan, M., Bay, C. J., Damiani, R., Kaminski, M., and Loth, E. "Structural Design of a 1/5 Th Scale Gravo-Aeroelastically Scaled Wind Turbine Demonstrator Blade for Field Testing." *AIAA SciTech*, 2019, pp. 1–9. doi:10.2514/6.2019-1067.

[19] Bay, C. J., Damiani, R., Jay Fingersh, L., Hughes, S., Chetan, M., Yao, S., Todd Griffith, D., Ananda, G. K., Selig, M. S., Zalkind, D. S., Pao, L. Y., Martin, D., Johnson, K. E., Kaminski, M., and Loth, E. "Design and Testing of a Scaled Demonstrator Turbine at the National Wind Technology Center." *AIAA Scitech Forum*, 2019.

[20] Mills, I., Cvitas, T., Homann, K., Kallay, N., and Kuchitsu, K. *Quanitites, Units, and Symbols in Phyiscal Chemistry*. Blackwell Science Ltd., 1993.

[21] Jonkman, J. M., Butterfield, S., Musial, W., and Scott, G. *Definition of a 5-MW Reference Wind Turbine for Offshore System Development*. 2009.

[22] Zalkind, D. S., Dall'Anese, E., and Pao, L. Y. "Automatic Controller Tuning Using a Zeroth-Order Optimization Algorithm." *Wind Energy Science- Discuss*, 2020. doi:10.5194/wes-2020-63.

[23] Hansen, M., Sørensen, J., Voutsinas, S., Sørensen, N., and Madsen, Ha. "State of the Art in Wind Turbine Aerodynamics and Aeroelasticity." *Progress in Aerospace Sciences*, Vol. 42, 2006, pp. 285–330. doi:10.1016/j.paerosci.2006.10.002.

[24] Bossanyi, E. A. Wind Turbine Control for Load Reduction. *Wind Energy*. 3. Volume 6, 229–244.

[25] Pao, L. Y., and Johnson, K. E. “Control of Wind Turbines: Approaches, Challenges, and Recent Developments.” *IEEE Control Systems Magazine*, Vol. 31, No. APRIL, 2011, pp. 44–62. doi:10.1109/MCS.2010.939962.

[26] Dunne, F., Aho, J., and Pao, L. Y. “Analysis of Gain-Scheduling Implementation for the NREL 5-MW Turbine Blade Pitch Controller.” *Proceedings of the American Control Conference*, Vol. 2016-July, 2016, pp. 3188–3193. doi:10.1109/ACC.2016.7525408.

[27] Jonkman, J. M., and Buhl, M. L. *FAST User’s Guide*. 2005.

[28] Drela, M. “XFOIL: An Analysis and Design System for Low Reynolds Number Airfoils.” *Low Reynolds Number Aerodynamics: Lecture Notes in Engineering*, Vol. 54, 1989. doi:10.1007/978-3-642-84010-4_1.

[29] Kohli, N. K., and Patel, L. K. *Study of Performance of Wind Turbine*.

[30] GE. Haliade-X 12 MW Offshore Wind Turbine Platform. https://www.ge.com/renewableenergy/wind-energy/offshore-wind/haliade-x-offshore-turbine.

[31] Diaz, V. Powered by Change: Siemens Gamesa Launches 14 MW Offshore Direct Drive Turbine with 222-Meter Rotor. https://www.siemensgamesa.com/en-int/newsroom/2020/05/200519-siemens-gamesa-turbine-14-222-dd#:~:text=With an unprecedented 14-megawatt,world currently undergoing enormous upheaval.

Appendix A

Blade Parameter Scaling	FAST Variable	SI Units	Scaling Parameter
Blade Fraction	BlFract	[-]	1
Aerodynamic Center	AeroCent	[-]	1
Structural Twist	StrcTwst	[-]	1
Blade Mass Density	BMassDen	$\frac{kg}{m}$	$\left(\frac{\rho_{wind,s}}{\rho_{wind,f}}\right)\eta^2$
Flapping Stiffness	FlpStff	$\frac{kg*m^3}{s^2}$	$\left(\frac{\rho_{wind,s}}{\rho_{wind,f}}\right)\eta^5$
Edge Stiffness	EdgStff	$\frac{kg*m^3}{s^2}$	$\left(\frac{\rho_{wind,s}}{\rho_{wind,f}}\right)\eta^5$
Axial Stiffness	GJStff	$\frac{kg*m^3}{s^2}$	$\left(\frac{\rho_{wind,s}}{\rho_{wind,f}}\right)\eta^5$
Torsional Stiffness	EAStff	$\frac{kg*m}{s^2}$	$\left(\frac{\rho_{wind,s}}{\rho_{wind,f}}\right)\eta^3$
Alpha	Alpha	[-]	1
Flapping Inertia	FlpIner	$kg*m$	$\left(\frac{\rho_{wind,s}}{\rho_{wind,f}}\right)\eta^4$
Edge Inertia	EdgIner	$kg*m$	$\left(\frac{\rho_{wind,s}}{\rho_{wind,f}}\right)\eta^4$
Reference Axis for Precurve	PrecrvRef	m	η
Reference Axis for Presweep	PreswpRef	m	η
Flapping Center of Gravity Offset	FlpcgOf	m	η
Edge Center of Gravity Offset	EdgcgOf	m	η
Flapping Elastic Offset	FlpEAOf	m	η
Edge Elastic Offset	EdgEAOf	m	η

Tower Parameter Scaling	FAST Variable	SI Units	Scaling Parameter
Tower Height	HtFract	[-]	1
Tower Mass Density	TMassDen	$\frac{kg}{m}$	$\left(\frac{\rho_{wind,s}}{\rho_{wind,f}}\right)\eta^2$
Tower Fore-aft Stiffness	TwFAStif	$\frac{kg*m^3}{s^2}$	$\left(\frac{\rho_{wind,s}}{\rho_{wind,f}}\right)\eta^5$
Tower Side-to-Side Stiffness	TwSSStff	$\frac{kg*m^3}{s^2}$	$\left(\frac{\rho_{wind,s}}{\rho_{wind,f}}\right)\eta^5$

Elastodyn Scaling	FAST Variable	SI Units	Scaling Parameter
Initial Out-of-Plane Tip Deflection	OPoPDefl	m	η
Initial In-Plane Tip Deflection	IPDefl	m	η
Intial Teeter Angle	TeetDefl	[-]	1
Initial Rotor Speed	RotSpeed	$\frac{1}{s}$	$\frac{1}{\sqrt{\eta}}$
Initial Fore-Aft Tower-Top Displacement	TTDspFA	m	η
Initial Side-to-Side Tower-Top Displacement	TTDspSS	m	η
Initial Horizontal Surge Translational Displacement	PtfmSurge	m	η

Initial Horizontal Sway Translational Displacement	PtfmSway	m	η
Initial Vertical Heave Translational Displacement	PtfmHeave	m	η
Rotor Apex to Blade Tip Distance	TipRad	m	η
Rotor Apex to Blade Root Displacement	HubRad	m	η
Rotor Apex to Hub Center of Mass	HubCM	m	η
Undersling Length	UndSling	m	η
Yaw Axis to Rotor Apex Distance	Overhang	m	η
Teeter Pin to Shaft Strain Gauge Distance	OverShftGagL	m	η
Towertop to Nacelle Center of Mass			
Downwind	NacCMxn	m	η
Lateral	NacCMyn	m	η
Vertical	NacCMzn	m	η
Towertop to Nacelle Inertial Measurement Unit		m	
Downwind	NcIMUxn	m	η
Lateral	NcIMUyn	m	η
Vertical	NcIMUzn	m	η
Towertop to Rotor Shaft Vertical Distance	Twr2Shft	m	η
Height of Tower	TowerHt	m	η
Height of Tower Base above Ground	TowerBsHt	m	η
Ground to Platform Center of Mass			
Downwind	PtfmCMxt	m	η
Lateral	PtfmCMyt	m	η
Vertical	PtfmCMzt	m	η
Tip Brake Mass	TipMass	kg	$\left(\frac{\rho_{wind,s}}{\rho_{wind,f}}\right)\eta^3$
Hub Mass	HubMass	kg	$\left(\frac{\rho_{wind,s}}{\rho_{wind,f}}\right)\eta^3$
Hub Inertia about Teeter Axis	HubIner	$kg * m^2$	$\left(\frac{\rho_{wind,s}}{\rho_{wind,f}}\right)\eta^5$
Generator Inertia about High-Speed-Shaft	GenIner	$kg * m^2$	$\left(\frac{\rho_{wind,s}}{\rho_{wind,f}}\right)\eta^5$
Mass of Nacelle	NacMass	kg	$\left(\frac{\rho_{wind,s}}{\rho_{wind,f}}\right)\eta^3$
Nacelle Inertia about Yaw	NacYIner	$kg * m^2$	$\left(\frac{\rho_{wind,s}}{\rho_{wind,f}}\right)\eta^5$
Yaw Bearing Mass	YawBrMass	kg	$\left(\frac{\rho_{wind,s}}{\rho_{wind,f}}\right)\eta^3$
Platform Mass	PtfmMass	kg	$\left(\frac{\rho_{wind,s}}{\rho_{wind,f}}\right)\eta^3$
Platform Inertia			
Roll	PtfmRIner	$kg * m^2$	$\left(\frac{\rho_{wind,s}}{\rho_{wind,f}}\right)\eta^5$
Pitch	PtfmPIner	$kg * m^2$	$\left(\frac{\rho_{wind,s}}{\rho_{wind,f}}\right)\eta^5$
Yaw	PtfmYIner	$kg * m^2$	$\left(\frac{\rho_{wind,s}}{\rho_{wind,f}}\right)\eta^5$
Rotor Teeter Damping Constant	TeetDmp	$\frac{kg * m^2}{s}$	$\left(\frac{\rho_{wind,s}}{\rho_{wind,f}}\right)\eta^{4.5}$
Rotor Teeter Coulomb Damping Moment	TeetCDmp	$\frac{kg * m^2}{s^2}$	$\left(\frac{\rho_{wind,s}}{\rho_{wind,f}}\right)\eta^4$

Rotor Teeter Soft Stop Linear Spring Constant	TeetSSSp	$\frac{kg*m^2}{s^2}$	$\left(\frac{\rho_{wind,s}}{\rho_{wind,f}}\right)\eta^4$
Rotor Teeter Hard Stop Linear Spring Constant	TeetHssp	$\frac{kg*m^2}{s^2}$	$\left(\frac{\rho_{wind,s}}{\rho_{wind,f}}\right)\eta^4$
Drivetrain Torsional Spring	DTTorSpr	$\frac{kg*m^2}{s^2}$	$\left(\frac{\rho_{wind,s}}{\rho_{wind,f}}\right)\eta^4$
Drivetrain Torsional Damper	DTTorDmp	$\frac{kg*m^2}{s}$	$\left(\frac{\rho_{wind,s}}{\rho_{wind,f}}\right)\eta^{4.5}$

Servodyn Scaling	FAST Variable	Base Units	Scaling Parameter
Pitch Rate	PitManRat	$\frac{1}{s}$	$\frac{1}{\sqrt{\eta}}$
Speed to Turn on Generator	SpeedGenOn	$\frac{1}{s}$	$\frac{1}{\sqrt{\eta}}$
Time to Turn on Generator	TimGenOn	s	$\sqrt{\eta}$
Time to Turn off Generator	TimGenOf	s	$\sqrt{\eta}$
Rated Generator Speed	VS_RtGnSp	s	$\frac{1}{\sqrt{\eta}}$
Generator Torque in Region 3	VS_RtTq	$\frac{kg*m^2}{s^2}$	$\left(\frac{\rho_{wind,s}}{\rho_{wind,f}}\right)\eta^4$
Generator Torque Constant in Region 2	VS_Rgn2k	$kg*m^2$	$\left(\frac{\rho_{wind,s}}{\rho_{wind,f}}\right)\eta^5$
Time to Initial Deployment of HSS Brake	THSSBrDp	s	$\sqrt{\eta}$
Time for HSS-Brake to Reach Full Deployment	THSSBrDT	s	$\sqrt{\eta}$
Fully Deployed HSS-Brake Torque	HSSBrTqF	$\frac{kg*m^2}{s^2}$	$\left(\frac{\rho_{wind,s}}{\rho_{wind,f}}\right)\eta^4$
Time to Enable Active Yaw Control	TyCOn	s	$\sqrt{\eta}$
Nacelle-yaw Spring Constant	YawSpr	$\frac{kg*m^2}{s^2}$	$\left(\frac{\rho_{wind,s}}{\rho_{wind,f}}\right)\eta^4$
Nacelle-yaw Damping Constant	YawDamp	$\frac{kg*m^2}{s}$	$\left(\frac{\rho_{wind,s}}{\rho_{wind,f}}\right)\eta^{4.5}$
Yaw Maneuver Rate	YawManRat	$\frac{1}{\mathrm{s}}$	$\frac{1}{\sqrt{\eta}}$

Aerodyn 14 Scaling	FAST Variable	Base Units	Scaling Parameter
Blade Length	RNodes	m	η
Zero-Lift line Twist	AeroTwst	[-]	1
Distance Between Nodes	DRNodes	m	η
Chord Length	Chord	m	η

3. Ground Testing of a 1% Gravo-Aeroelastically Scaled Additively-Manufactured Wind Turbine Blade with Bio-inspired Structural Design

Abstract

A gravo-aeroelastic scaling (GAS) method is developed to design wind turbine blades that represent centrifugal, aerodynamic, and gravitational loads of extreme-scale turbines. To match these elements, certain blade characteristics are given priority: non-dimensional 1st flap-wise frequency, non-dimensional flapping tip deflection, and tip-speed-ratio. Using the GAS method, a 1% sub-scale blade was designed to match the mass distributions and ground tested to match the non-dimensional flap-wise dynamics and deflections of Sandia National Lab's 13.2-MW blade. To the authors' knowledge, this is the first manufactured blade model to employ gravo-aeroelastic scaling using additive manufacturing and bio-inspiration. A series of scale models were designed, built, and ground-tested using weights consistent with scaled steady rated loads conditions of an extreme-scale turbine. The models designed were evolved to increase gravo-elastic scaling performance by employing lightweight bio-inspirational morphology and carbon fiber reinforcements. The final version has non-dimensional gravo-elastic errors as follows: 3% in total mass, 15.6% in deflection from ground-based loads representing full-scale steady rated conditions, and 8.1% in the first flap-wise modal frequency (when normalized by the scaled rpm for rated conditions). This model demonstrates the GAS concept can be applied to manufacture sub-scale models as small as 1% of an extreme-scale rotor blade.

Nomenclature

a_n	=	constant
a	=	speed of sound
$BSSE$	=	blade structural scaling error
c	=	chord length
c_t	=	distributed coefficient of thrust
D	=	average rotor diameter
d	=	diameter
EI	=	stiffness
g	=	gravitational constant
H	=	average hub height
I	=	sectional moment of inertia
L	=	beam length
m	=	blade mass
M	=	moment
Ma	=	Mach Number
P	=	tip load
Re	=	Reynolds Number
s	=	spanwise location
S	=	total blade length
t	=	material thickness
U	=	wind speed
β	=	coning angle
δ	=	tip deflection
η	=	scaling factor
ρ	=	density
Ω	=	rotational speed
ω_{flap}	=	flap-wise frequency

Subscripts

$()_C$	=	centrifugal
$()_{cm}$	=	center of mass
$()_{design}$	=	version value
$()_f$	=	full-scale
$()_G$	=	gravitational
$()_i$	=	sectional value
$()_{ideal}$	=	ideal value
$()_{rated}$	=	rated value
$()_{rel}$	=	relative value
$()_s$	=	sub-scale
$()_T$	=	thrust
$()_{wind}$	=	wind value
$()'$	=	distributed value
$\overline{()}$	=	non-dimensional value

3.1 Introduction

In 2013, wind energy accounted for 4.5% of US electricity demand and is one of the fastest growing sources of new electricity supply [1]. It is predicted renewable energy will increase from 13% in 2013 to 18% in 2040 with wind being the largest source of renewable energy generation within the United States energy market [2]. The growth can be attributed to technology developments leading to an improvement of performance, an increase of reliability, and a reduction in the cost of energy [1]. Technological advances aid the increase in rotor diameter (D) and hub height (H) as seen in Figure 3-1, with future turbines expected to have diameters in excess of 200-meters and thus blade lengths in excess of 100-meters.

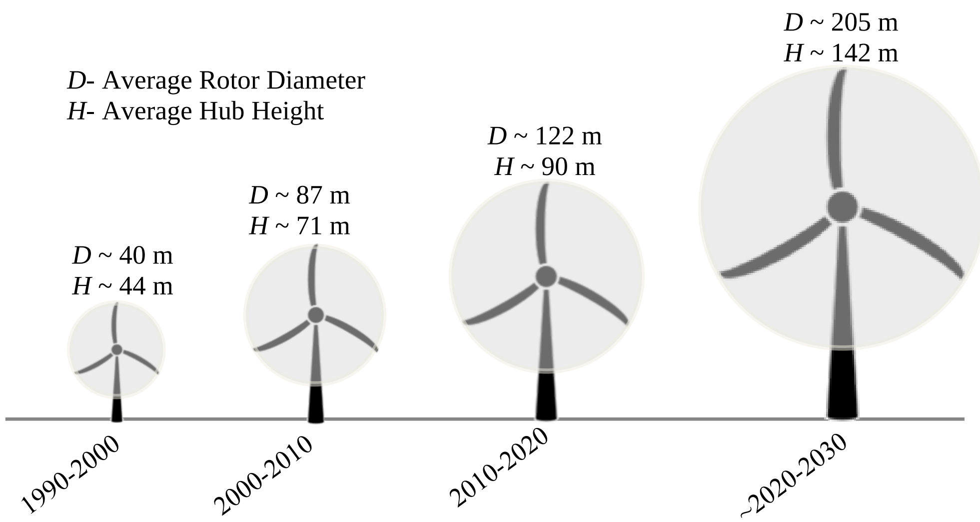

Figure 3-1: The increasing trend of average production rotor sizes with the advancement of time.

Sandia National Labs has computationally shown this increase in blade size is viable with the design of the SNL100-XX series [3–6]. Each blade in the series is a 100-meter blade designed for a 13.2 MW turbine. The initial baseline design, the SNL100-00 blade weighs 114 tons and is made primarily of fiberglass material with the conventional sharp trailing edge airfoil design of the time. The final design, the SNL100-03 blade, is the lightest version to satisfy all the key performance characteristics. It weighs 53 tons and uses carbon reinforcements and flatback airfoils to reduce the amount of material needed, which therefore reduces the weight compared to the initial design by over 50%. These turbines with blade lengths of 100-meters and beyond have been termed "extreme-scale" systems [7].

Other turbine designs are also aiming for such extreme-scale rotors [7,8] however, due to the lack of physical testing on blades or rotors of this size, there are no experimentally confirmed designs as of yet [8]. Such full-scale testing (ground testing or field testing) is prohibitively expensive. As such, there is a need for scaled designs which can allow the physical testing to alleviate the risk of full-scale projects with new rotor technology [9]. In particular, scale models allow for verification of key aspects of blade and rotor design without the same commitment of resources [10].

Previous scaling techniques for structures under aerodynamic loads aim to scale aerodynamically and/or aeroelastically in order to study deflection and dynamic responses suitable for validating computational methods [9–15]. These techniques have been used for testing helicopter blades [10], lightweight aircraft [11], and off-shore wind turbines subjected to wave induced motions [9,12–15]. One such test, the DeepCwind test created a $1/50^{th}$-scaled model of a 5-MW offshore floating wind turbine [12,15]. The test utilizes Froude number scaling for the geometry and environmental conditions, and attempts to offset the changes in aerodynamic forces from the change in Reynolds number by increasing the windspeed. The turbines for this test properly scaled the mass of the turbine relative to the mass of the waves, however, the blades were made to be completely rigid in order to remove complications from stiffness scaling. This approach was appropriate as the interest was in understanding different floating platform designs and their interactions with an assortment of wind and wave loads and not on aeroelastic dynamics. In another example, a $1/93^{rd}$ scaled wind turbine blade of the 44-meter Vestas V90 blade was built to be aeroelastically scaled in terms of the ratio of flap-wise frequency to rotational frequency, but with the gravitational scaling ignored [13]. This approach was appropriate, as the interest was on the deflections caused by centrifugal and aerodynamic forces since gravitational loads are relatively small (in comparison) at rated conditions. However, scaling applied to extreme-scale turbines leads to additional complexity. In particular, gravitational loadings scale at a faster rate than aerodynamic loadings [3]. With blade lengths equal to or greater than 100-meters, the gravitational loadings become of high significance [7,16,17] and therefore must also be taken into account. This indicates a need to apply a scaling which incorporates both the gravitational, aerodynamic, and elastic properties of wind turbine blades. While sub-scale designs have been completed [18], no such designs have been manufactured to the authors' knowledge.

Design and manufacturing difficulties arise if the scale reduction factor is significant. These difficulties include but are not limited to an extremely lightweight scaled mass, high stiffness, and the inability to manufacture the sub-scale with the same materials as the full-scale. These difficulties are further explained in the Methods section.

The mass and stiffness of a blade are limited when using the conventional skin and spar blade designs. To alleviate these limitations when scaling, a bio-inspired structural design is explored. It has been shown topologies resembling the internal structure of bone [19] can minimize mass, while withstanding a specified amount of load in a variety of directions. This structural efficiency follows Wolff's law, whereby human or animal bone structure grows and adapts to the loads applied and expected. Over time, if the bone's loadings increase, so will its internal support, if the loadings decrease, the support too will decrease [20]. The bone shown in Figure 3-2a, includes many truss-like elements with rounded joining regions and with multiple directions of support. The concentration and size of these bone structures is specific to the applied and expected loads. As an example, someone highly active in a single-handed racquet sports can develop significant asymmetries between the bones of their dominant and non-dominant arms as compared to a control subject. This is a result of the increased loading on the racquet holding arm [21]. Thus, expected loads and evolutionary optimization allow for bone to have the lowest possible mass to support the given (applied or expected) loads. Inspired by such biological topologies, engineers use these structural concepts for product designs which must withstand a significant set of loads while retaining low mass. It is predicted this design technique will prove beneficial to the 1% model design.

Fabricating such bio-inspired designs with conventional manufacturing can be an extreme challenge, fortunately, additive manufacturing is an emerging technology allowing for separation from current subtractive methods by creating the product layer by layer. This allows for rapid innovative product design and testing without the need of extra spare parts, new tooling, etc. [22] which therefore reduces overall development cycles [23]. Additive manufacturing encourages novel product designs many of which resemble bio-inspired structural approaches to optimize the part's topology. Airbus's subsidiary, APWorks, is one of the leading designers in additively manufactured products. They have many different designs incorporating both bio-inspiration and additive manufacturing to reduce the weight and therefore the cost of the product. Among the many products are designs for an aircraft partition creating a 44% weight savings while also increasing the stiffness, a cabin bracket with a 72% weight savings, and an armrest with a 44% weight savings [23]. Their most unconventional part is the Light Rider motorcycle, the world's first prototype of a 3D printed motorcycle shown in Figure 3-2b. Researchers at the Technical University of Denmark too are optimizing the internal structure of aircraft wings in order to reduce the mass compared to conventional as seen in Figure 3-2c. These designs employ topologies similar to the internal bone topology of Figure 3-2a. However, this concept has not been previously applied to a wind turbine blade structural design, which tend to favor more conventional skin-and-spar designs lacking the ability to further optimize the blade structural performance topology.

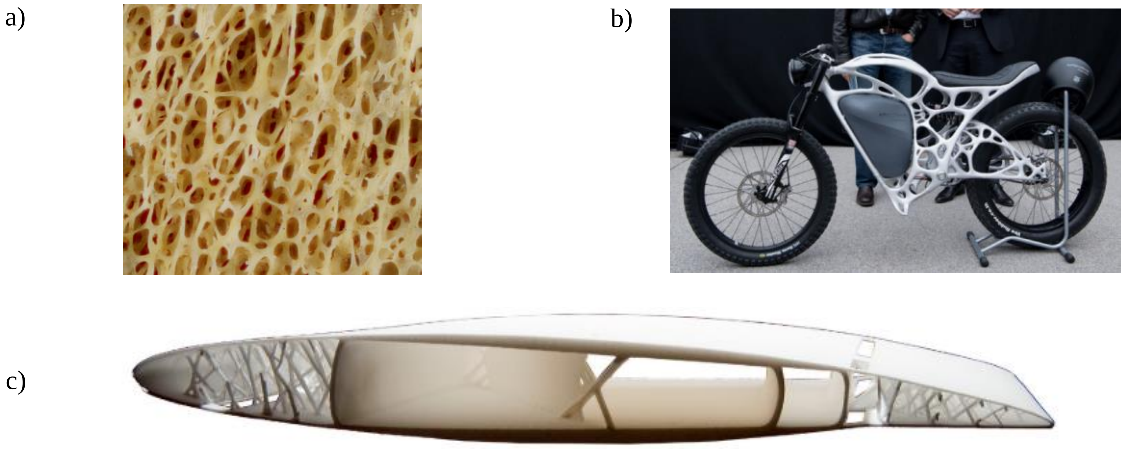

Figure 3-2: a) Internal structure of the spongy bone in the femur of a cow [24], b) the first additively manufactured motorcycle [23,25], and the topologically optimized airplane wing [19].

The first objective of this study is to combine both gravitational and aeroelastic effects for gravo-aeroelastically scaled models that allow for high-fidelity non-dimensional representation of the dynamics and deflections in the operation of extreme-scale rotors [16,17]. The second objective is to apply the GAS method to the SNL100-03 [6] wind turbine blade for a 1/100th structurally scaled model utilizing additive manufacturing and bio-inspired design. This model is then static ground tested with loads mimicking the full-scale steady rated conditions to show the viability of creating a model to simulate full-scale models at a sub-scale size.

To the authors' knowledge, this demonstration is the first study to additively manufacture and gravo-elastically test a scaled structural model of an extreme-scale wind turbine blade and the first to use the gravo-aeroelastic scaling method for design. Additionally, this is the first to employ bioinspired structural design to reduce weight for a given stiffness on scaled wind turbines.

Section 3.2 reviews the methods to obtain GAS models for extreme-scale wind turbine blades and methods to develop an additively manufactured blade displaying bio-inspired structural design. Section 3.3 includes the ideal scaling of the 1% SNL 100-03 blade used as a structural design goal and the physical iterations of the fabricated scaled blades seeking to replicate this ideal design via gravo-elastic ground testing. Section 3.4 provides concluding remarks and recommendations for future work.

3.2 Methods

3.2.1 Gravo-Aeroelastic Scaling

The following GAS method combines gravitational and aeroelastic scaling for an extreme-scale blade in terms of flap-wise structural performance to properly mimic the non-dimensional centrifugal, gravitational, and aeroelastic loads acting on the blade. To begin, it is important to determine a scaling factor of the model (η). This is defined by the ratio of the total blade lengths (S) shown in equation (3.1) and in Figure 3-3a with the subscripts *s* and *f* referring to the sub-scale and full-scale models respectively. This factor also applies to all external dimensions and deflections of the blade including the center of gravity and the blade chord (c).

$$\eta = \frac{S_\mathrm{s}}{S_\mathrm{f}} \tag{3.1}$$

When scaling a blade, it is important to keep the blade root moments imparted at the rotor hub on the turbine scaled appropriately for the purpose of loads matching between full- and sub-scale. The moments experienced by the scaled blade determine the appropriate structural design and stiffness to preserve the non-dimensional deflections and dynamics of the full-scale blade. Because moments are influenced by forces with moment arms, this scaling places more emphasis on the loading and properties near the tip of the blade as compared to those inboard. The moments at the hub are expressed as a summation of all the distributed moments, which are the moments per unit spanwise length at a given point along the blade.

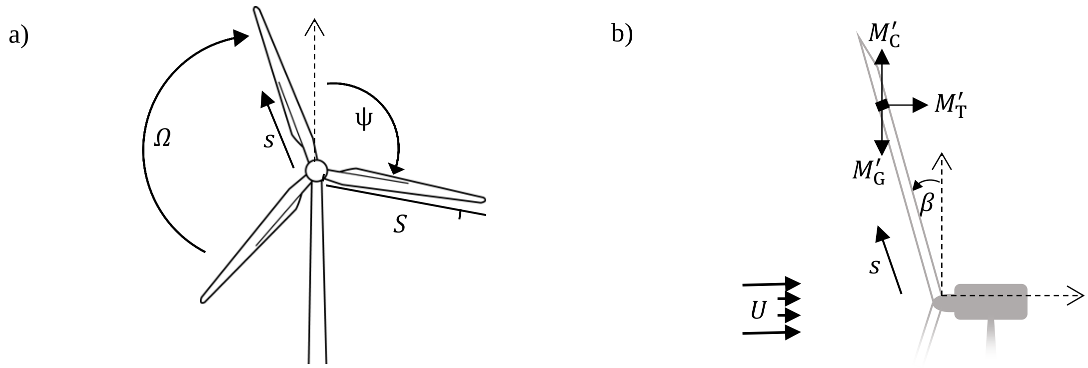

Figure 3-3: An upwind three-bladed turbine with a) the front view showing: rotational speed (*Ω*), sectional distance along the blade length (*s*), and total blade length (*S*) and b) the side view showing sectional bending moments (M'_Q), coning angle (β), and wind speed (*U*) and again the sectional distance along the blade length (*s)* with a non-rotating coordinate frame.

Figure 3-3b depicts the blade in a vertical upward orientation with a coning angle (β) in order to express the distributed moments in the blade flap-wise directions for accurate tip deflections. The three main flap-wise distributed moments felt at the blade root are thrust (M'_T), centrifugal (M'_C), and gravitational (M'_G). These are expressed analytically as follows:

$$M'_T = \frac{1}{2}\rho_{\text{wind}} c U_{\text{rel}}^2 c_t s[\cos(\beta)] \tag{3.2}$$

$$M'_C = m'\ \Omega^2 s^2[\cos(\beta)\sin(\beta)] \tag{3.3}$$

$$M'_G = m'\ gs[\sin(\beta)\cos(\psi)] \tag{3.4}$$

The values above include ρ_{wind} as the air density, U_{rel} as the relative wind speed (which includes wind speed due to the rotation of the blade and the incoming wind), Ω as the rotational speed, and *g* as the gravitational constant. The values that vary as a function of spanwise length, *s*, include c_t as the sectional coefficient of thrust, *c* as the chord length, and *m'* as the distributed mass density of the blade (with units of mass per unit spanwise length).

To find the total moments felt by the root of the blade, the sectional moments due to a force Q can be integrated from the root to the tip of the blade over a differential blade length (*ds*) as shown below, where Q can be replaced by *C*, *T*, or *G*.

$$M_Q = \int_0^S M'_Q\, ds \tag{3.5}$$

There are two main moment ratios to define before determining the scaling parameters. The first is the ratio of sectional gravitational to centrifugal moments, which is the moment equivalent to the Froude number, and the second is the sectional centrifugal to thrust moment, where these are written as follows:

$$M'_G \big/ M'_C = \frac{g}{\Omega^2 s[\cos(\beta)]} \tag{3.6}$$

$$M'_C \big/ M'_T = \frac{2m'\ \Omega^2 s[\sin(\beta)]}{\rho_{\text{wind}} c {U_{\text{rel}}}^2 c_t} \tag{3.7}$$

In terms of dynamics, aeroelasticity, and velocity angles, there are three critical non-dimensional values that should be held constant between the full- and sub-scale blades when designing the sub-scale model: the non-dimensional 1st flap-wise frequency, the non-dimensional maximum steady state tip deflections, and the tip-speed-ratio (TSR). The non-dimensional flap-wise frequency is defined in equation (3.8a). This is the ratio of the primary blade natural frequency (ω_{flap}), defined in equation (3.8b), based upon uniform beam deflections, to the primary input frequency (Ω, rotational speed). In this equation, α_n is a constant that is a function of boundary conditions, mass distribution, and stiffness distributions and is ideally the same between full- and sub-scale, EI is blade stiffness, m is total blade mass, and S is the length of the blade. This non-dimensional frequency drives the flap-wise dynamics of the blade and preserving this value ensures the scaled mass and stiffness values are proportional to each other. In addition, the flap-wise frequency divided by omega in equation (3.8a) is held constant from full-scale to sub-scale ensuring that the spacing of per-rev frequencies are maintained at sub-scale; for example, a design free of blade resonant conditions at the full-scale is also free of resonance at the sub-scale. The non-dimensional maximum steady state tip deflection defined in equation (3.9) is the ratio of the maximum steady-state rated deflection of the blade (δ) to the total length of the blade (S). A consequence of matching both equations (3.8a) and (3.9) is the scaled mass and stiffness will both be appropriately scaled. Lastly, by keeping the tip-speed-ratio (TSR) in equation (3.10) constant, the approaching flow angles relative to the rotor blade will be preserved. The various parameters within the TSR are visually shown in Figure 3-3 where $\Omega S\cos(\beta)$ is the tip-speed, and U is the wind speed.

$$\bar{\omega} = \frac{\omega_{\text{flap}}}{\Omega} \tag{3.8a}$$

$$\omega_{\text{flap}} = \alpha_n^2 \sqrt{\frac{EI}{mS^3}} \tag{3.8b}$$

$$\bar{\delta} = {}^{\delta}/_{S} \tag{3.9}$$

$$TSR = \frac{\Omega S\cos(\beta)}{U} \tag{3.10}$$

Keeping equations (3.8a), (3.9), and (3.10) constant, the scaling of appropriate blade parameters are determined using equations (3.1)-(3.4). The factors are summarized in Table 3-1, and the steps used to obtain them are as follows.

To begin, the rotational speed scaling ($\eta^{-1/2}$) is found by keeping the ratio of equation (3.6) constant between full- and sub-scale and applying the scaling factor of equation (3.1). With this result and keeping the tip-speed-ratio constant in equation (3.10), the wind speed scaling ($\eta^{1/2}$) is obtained. Applying the scaling factor to both the chord and to the sectional blade length, as well as scaling the wind and rotational scaling by equation (3.7), the distributed blade mass scaling can be obtained. The result for the distributed blade mass scaling is η^2 if the air density does not vary, but if the full-scale and sub-scale systems operate at substantially different altitudes, then air density effects should be considered. From this, one can integrate to obtain the total blade mass scaling (η^3). With keeping the non-dimensional flapping frequency constant in equation (3.8a) and applying the rotational scaling previously determined, one obtains the scaling for the flap-wise frequency ($\eta^{-1/2}$). Applying the scaling for frequency, mass, length, and the assumption that the α_n term of equation (3.8b) remains constant between the full- and sub-scale models, the bending stiffness (EI) scaling can be obtained (η^5). When developing a scaled model with the same materials, the wall thickness scales by combining the stiffness scaling and the moment of inertia of a section. For example, the sectional moment of inertia for a hollow uniform circle of diameter, d, and wall thickness, t, is given as follows:

$$I = const.(d^3 t) \tag{3.11}$$

This same proportionality (with a different defined constant) applies for a wind turbine blade given a reference diameter and blade skin thickness. Assuming material similarity at full- and sub-scale the sectional moment of inertia, equation (3.11), scales with η^5 (assuming all material properties are unchanged), thus the material thickness is to be scaled by η^2, as opposed to the assumed scaling, η, in order to preserve the scaled blade stiffness.

Table 3-1. Various parameters for GAS scaling and their associated scaling factors.

Scaling Parameter	Scale Factor
Length Scaling: $\frac{S_s}{S_f}$	η
Rotational Scaling: $\frac{\Omega_s}{\Omega_f}$	$1/\sqrt{\eta}$
Wind Velocity Scaling: $\frac{U_s}{U_f}$	$\sqrt{\eta}$
Total Blade Mass Scaling: $\frac{m_s}{m_f}$	$\left(\frac{\rho_{\mathrm{wind,s}}}{\rho_{\mathrm{wind,f}}}\right)\eta^3$
Distributed Blade Mass Scaling: $\frac{m_s^{'}}{m_f^{'}}$	$\left(\frac{\rho_{\mathrm{wind,s}}}{\rho_{\mathrm{wind,f}}}\right)\eta^2$
Flap-wise Frequency Scaling: $\frac{\omega_{\mathrm{flap,s}}}{\omega_{\mathrm{flap,f}}}$	$1/\sqrt{\eta}$
Stiffness Scaling: $\frac{(EI)_s}{(EI)_f}$	$\left(\frac{\rho_{\mathrm{wind,s}}}{\rho_{\mathrm{wind,f}}}\right)\eta^5$
Reynolds Number Ratio: $\frac{Re_s}{Re_f}$	$\left(\frac{\rho_{\mathrm{wind,s}}}{\rho_{\mathrm{wind,f}}}\right)\left(\frac{\mu_{\mathrm{wind,f}}}{\mu_{\mathrm{wind,s}}}\right)\eta^{3/2}$
Mach Number Ratio: $\frac{Ma_s}{Ma_f}$	$\left(\frac{a_{\mathrm{wind,f}}}{a_{\mathrm{wind,s}}}\right)\sqrt{\eta}$
For Fixed Materials and Structural Design:	
Material Thickness Scaling: $\frac{t_s}{t_f}$	$\left(\frac{\rho_{\mathrm{wind,s}}}{\rho_{\mathrm{wind,f}}}\right)\eta^2$

When scaling in the same fluid density, there will be a difference in Reynolds number and Mach numbers. The difference in Mach number can be reasonably ignored if the Mach numbers are below compressibility effects [11]. For the Reynolds number mismatch, studies have shown the aerodynamics can be sensitive to such changes so that fixing the aerodynamic shape and flow angles will not preserve the thrust coefficient [26]. It should be noted that the objective of scaling flap-wise loads is to achieve the same moment ratios and overall aeroelastic loads. Thus, one may design the sub-scale model at a different C_p and change the pitch to match the thrust coefficient and flap-wise dynamics at a single operating point. Additional options to better match the thrust include, but are not limited to: tripping the boundary layer, redesigning the airfoil geometry, and applying an appropriate resisting motor to the turbine [16,27,28]. Note that matching the scaled flap-wise moments with such changes will generally prevent simultaneous scaling of the edgewise moments. However, the flap-wise deflections and dynamics are the focus herein as they are much greater than the corresponding edgewise values for the full-scale turbine. As such, the decision for adjustments is dependent on specific research goals.

3.2.2 The SNL100-03 Blade Reference Design

In the present study, the GAS method is applied to the 13.2 MW 100-meter SNL100-03 wind turbine blade [6] to determine a 1% model. This full-scale blade model is chosen based upon its advanced design as an extreme-scale wind turbine. The SNL100-03 is a fourth generation concept design [3–5] that introduces flatback airfoils to reduce the weight of the blades and includes the following blade materials (by percent of the total blade mass): E-Glass/Epoxy (E-LT-5500) - 15.5%, Saertex - 11.4%, Carbon Prepreg - 30.1%, Epoxy Resin (EP-3) - 32.5%, Balsa - 2.5%, Polyethelene Teraphalate (PET) Foam - 6.5%, and a Gel coat - 1.3%. The primary materials are located in Figure 3-4 which also depicts the internal structure of the full-scale SNL100-03 blade including the shear webs and the upper and lower spar caps [6].

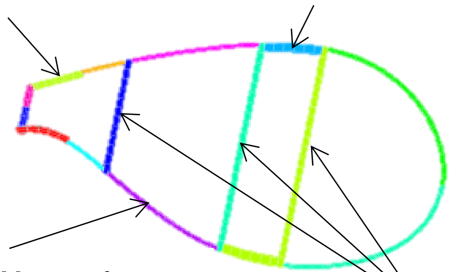

Figure 3-4: The primary structure and materials of the full-scale SNL100-03 blade.

3.2.3 Scaled Model Ground-Testing Method

To assess whether the GAS method can be successfully applied to models as small as 1/100th scale, equations (3.8a)-(3.10) are verified in terms of the gravo-elastic properties. In particular, ground testing is used to compare the blade mass (sectional distribution as well as total value), maximum steady state tip deflection, and first flap-wise frequency of the blade. Other aspects are of secondary influence on flap-wise deflections and thus are not scaled: the chord wise mass density, edgewise stiffness, rotational stiffness, and axial stiffness. These are secondary since the primary forces which impact blade flap-wise deflections for the full-scale rotor in operation are flap-wise gravitational, aerodynamic, and centrifugal forces. The total mass of a manufactured blade is obtained through weighing on a scale, accurate to ±0.1 grams, while the mass density (mass per unit span) is verified through SOLIDWORKS. The center of mass is also compared between the full- and sub-scale models through equation (3.12) and summing down the length of the blade.

$$s_{\mathrm{cm}} = \frac{\sum s_i m_i}{m} \tag{3.12}$$

Typical aeroelastic testing involves an interaction between the aerodynamic, elastic and inertial forces on a structure in a flow. Such operational testing for a study of this scale can be very difficult since, the Reynolds number mismatch can significantly affect the aerodynamics. Therefore, the blades are only static ground tested for flap-wise tip deflections by applying weights to represent the scaled operational root flap-wise bending moment at steady rated conditions. Figure 3-5 shows the setup for testing the tip-deflection and the first flap-wise frequency of the blade. The root of the blade is held in place creating a fixed root boundary condition. For testing of the maximum steady state tip deflection, various loads stepping up to the maximum scaled flap-wise moment of the full-scale blade are applied to the tip and the amount the tip deflects is measured from a static state shown in Figure 3-5c. This is compared to non-dimensional ANSYS deflections of the SNL100-03. Although the stiffness along the length of the blade varies, the maximum tip deflections (δ) are similar to a uniform, constant stiffness (EI) beam of length L, resulting from a tip load (P) as described in equation (3.13).

$$\delta = \frac{PL^3}{3EI} \tag{3.13}$$

This flap-wise deflection in a gravo-elastic ground test can be used to quantify the steady-state scaling properties of the fabricated blade. In particular, this deflection can be normalized by blade length to compare with the non-dimensional deflection values of the full-scale blade by using Table 3-1.

To consider the dynamic properties of this same blade, a step relaxation, or “pluck test”, is applied to determine the first flap-wise frequency shown in Figure 3-5a. This is achieved by applying a fixed load to the tip of the blade, and then removing it suddenly so the blade responds in an unsteady manner with free vibrations [29]. The flap-wise frequency of the blade is determined by the inverse of the time for the blade to complete one cycle of deflections as described by Figure 3-5b. These vibrations can be used to determine flap-wise frequency and can be compared to the non-dimensional values of the full-scale blade by using Table 3-1.

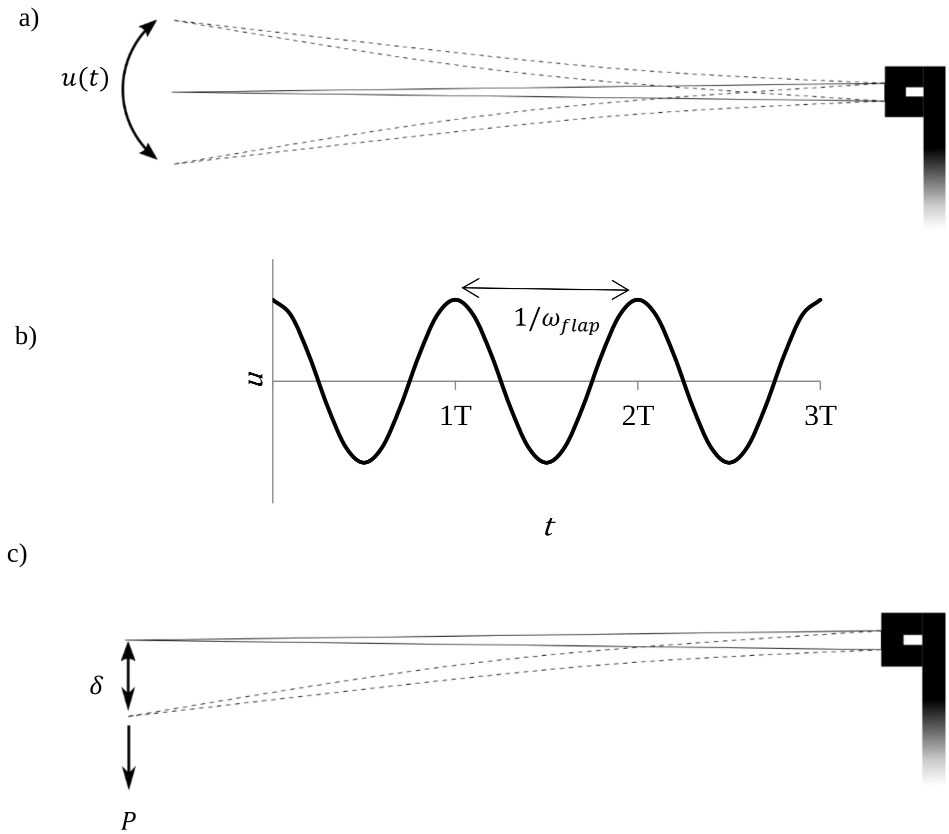

Figure 3-5: The experimental setup to test scaled blade deflections: a) unsteady deflections resulting from a pluck test, b) time evolution of deflections to obtain natural frequency, and c) steady state tip deflections based on a scaled load placed at the tip.

3.2.4 Scaled Model Materials, Manufacturing and Scaling Accuracy Parameter

For manufacturing the $1/100^{th}$ model, the material thickness-scaling factor from Table 3-1 is referenced. When scaling the familiar material of balsa at its maximum thickness of 39 mm, the 1% scaled model operating in the same air density would be 3.9 μm. This is an impractically small thickness (the thinnest available piece of balsa readily available for production is 0.5 mm) and one that would lead to buckling problems. Therefore, alternate materials and structural designs are needed to manufacture the scaled blade. Additive manufacturing of the blade was determined to be a highly effective solution for design since it allows for quick turnaround time between the design phase and the manufacturing phase [30]. Another benefit of additive manufacturing is the additional degrees of freedom of design topography as compared to subtractive manufacturing methods [31] permitting innovative structural designs and the ability to match the structural efficiency of the full-scale at a sub-scale size.

For the $1/100^{th}$ blade, the Stratasys PolyJet 3D printer was used due to its ability to print multiple materials on a single part, high tolerance, layer resolution, and accuracy [32]. The PolyJet 3D printer allows for the combination of materials utilized for manufacturing as outlined in Table 3-2. This range of material stiffness allows alterations in the deflections similar to the beam deflection equation (3.13) and can help to retain the main values outlined in equations (3.8a), (3.9), and (3.10). Additional materials such as a carbon fiber strip (for added blade stiffness) and the plastic wrap (for external blade shell) are also included in Table 3-2.

Table 3-2: Material properties of the elements for the 1% GAS SNL100-03 blade.

Material	Vendor & Name	Modulus of Elasticity (MPa)	Density (g/cm^3)
Rigid Resin	Stratasys- VeroWhite	2100	1.17
Rigid+Rubber Resin	Stratasys- RGD8505	1900	1.17
Rigid+Rubber Resin	Stratasys- RGD8510	1700	1.17
Rigid+Rubber Resin	Stratasys- RGD8515	1500	1.17
Rigid+Rubber Resin	Stratasys- RGD8520	1300	1.17
Rigid+Rubber Resin	Stratasys- RGD8525	1000	1.17
Rigid+Rubber Resin	Stratasys- RGD8530	700	1.17
Rubber Resin	Stratasys- Tango Black	~5.8	1.14
Carbon Fiber	The Composites Store- High Modulus Carbon Fiber Strip [33]	240000	1.59
Polyethylene	GLAD ClingWrap [34,35]	~113	1.68

Additive manufacturing presents limitations to the wall thickness. With this limitation, and the mass constraints presented in Table 3-1, the third shear web is removed through all iterations of the blade. The goal is to keep the remaining internal structure of the blade constant with the full-scale model; however, if needed, the internal structure can be altered so long as the blade retains the main values outline in equations (3.8a), (3.9), and (3.10). Even with the removal of the third shear web, structural optimization is required to satisfy these values at the subscale due to the low mass and high stiffness constraints of extreme-scale wind turbines.

Conventional manufacturing techniques at the sub-scale cannot match the full-scale blade dynamics due to design limitations in both the mass and stiffness constraints. Optimization of the structure to match these constraint requirements (such as stress, structural deflection, mass, etc.), is completed by reducing the mass and material within a given outer shape [36,37]. The optimized structures lead to designs with high stiffness, low mass, and designs with material solely in locations where it is needed, and voids where material is not needed. This design methodology is known as a bio-inspired structural design [37]. To test the efficiency of the design, a Blade Structural Scaling Error (BSSE) is defined for comparison with previous designs. For the case of the 1% blade, the design performance is based upon the tip deflections and the mass of the blade as defined in equation (3.14). If the BSSE is 0, then the stiffness and mass is scaled appropriately, and therefore the blade frequency (by Equation (3.8b)) is also scaled appropriately.

$$\mathrm{BSSE} = \sqrt{\left(\frac{\delta_{\mathrm{design}} - \delta_{\mathrm{ideal}}}{\delta_{\mathrm{ideal}}}\right)^2 + \left(\frac{m_{\mathrm{design}} - m_{\mathrm{ideal}}}{m_{\mathrm{ideal}}}\right)^2} \tag{3.14}$$

To reduce the BSSE of the design, the structure must closely match the mass and deflections of the full-scale model. To match each of these, it is intelligent to refer to the way in which the internal structure of bone is developed, namely, the spongy bone. This keeps the mass as low as possible, while also being able to withstand the given loadings resulting in an internal structure resembling Figure 3-2a. By replicating and adapting this design, the 1% model will ideally be able to match the difficult mass constraints of a scale model of this size, but also be able to match the tip deflections prescribed ultimately reducing the BSSE of the blade.

3.3 Results and Discussion

3.3.1 Gravo-Aeroelastic Scaling Results

Applying the GAS methods of Table 3-1 to a 1/100$^{\mathrm{th}}$ model of the SNL100-03 blade results in the scaling summarized in Table 3-3. The leftmost column contains the full-scale 100-meter values, the middle column contains the GAS scaled 1% values and, to compare extreme-scale values to conventional values, the rightmost column contains a conventional 0.9-meter length blade [38]. The conventional rotor mass, even though it uses fiberglass and carbon fiber, is about 4.5 times heavier than the sub-scaled version of an extreme-scale rotor of about the same length. This difference shows gravo-aeroelastic sub-scaling dramatically reduces the blade mass relative to what would be expected from a technology used for similar blade lengths. This is demonstrated in Figure 3-6 which shows the trends in mass scaling for gravo-aeroelastic scaled blades and conventional blades. The solid black line shows typical blade mass for rotors designed ideally for their respective size, and shows the SNL100-03 blade is consistent with this trend. This trendline shows mass changes with $S^{2.1}$ due to differing technological evolutions including manufacturing techniques and materials as blade rotor sizes increase. This proportionality is well documented [39,40]. The dashed blade line shows the mass of a blade scaled gravo-aeroelastically, following an S^3 line (Table 3-3). Using the SNL100-03 blade as the reference, a 1-meter gravo-aeroelastic blade is significantly lighter than a blade using conventional technologies at the same length. This highly reduced mass required for the gravo-aeroelastically scaled blade demonstrates a challenge of creating a very low mass design as compared to designs using conventional methods.

Table 3-3: The 1% Ideal GAS SNL100-03 blade and its full-scale counterpart compared to a conventional blade.

	Full-Scale SNL-100-03	**1% Ideal GAS SNL100-03**	**Carbon Fiber 0.9-Meter Blade** [38]
Design Innovation	Extreme-Scale	Extreme-Scale	Conventional-Scale
Rotor Radius (R)	100 m	1 m	0.9 m
Length Scaling Factor (η)	1	0.01	-
Blade Mass (m)	49,519 kg	49.52 g	220g
Rated Wind Speed (V_{rated})	11.3 m/s	1.13 m/s	12.5 m/s
Tip-Speed Ratio (λ)	9.5	9.5	11.6
Rated Rotor speed (Ω)	10.25 RPM	102.5 RPM	649 RPM
Flap-wise Frequency (ω_{flap})	0.49 Hz	4.9 Hz	-
Ref. Reynolds Number (Re)	$1.54\text{x}10^7$	$1.23\text{x}10^4$	$4.14\text{x}10^5$
Ref. Mach Number (Ma)	0.224	0.022	0.119

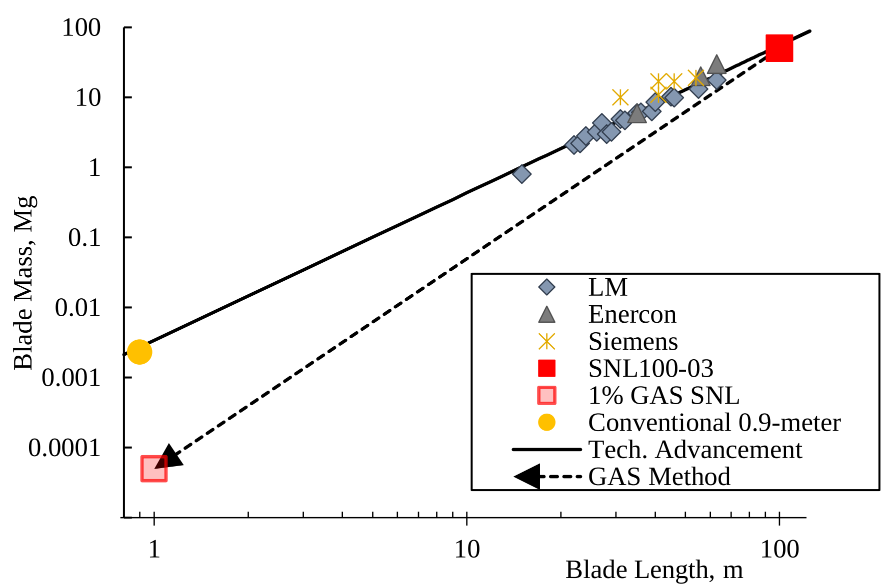

Figure 3-6: The technological advancement of blades (solid line) compared against GAS method blades (dashed line).

The primary reasons for the reduced blade mass when GAS is applied is illustrated in Figure 3-7, which shows the ratio of the moment due to gravitational loads to the moment due to centrifugal loads M_g/M_c. The solid black line again shows the conventional values for this ratio based on an assumption of constant tip-speed, which results in gravitational moments being much weaker at small scales. The dashed black line shows the constant value of this moment ratio needed to properly employ the GAS method including changes in tip-speed (Table 3-1). This plot shows the significance of gravitational loading for extreme-scale blades. In the following, various structural designs are considered in order to keep this moment ratio of Figure 3-7 constant with the low mass shown in Figure 3-6.

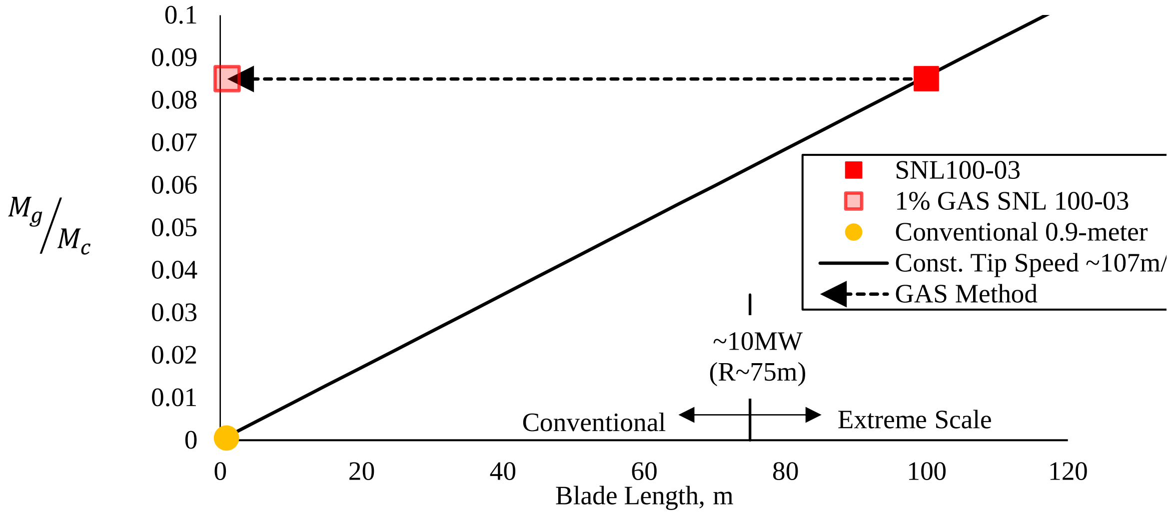

Figure 3-7: Ratio of gravitational to centrifugal moments using GAS methods as shown by the dashed line, where the solid diagonal black line is based on a fixed tip speed (~107 m/s) and as-fabricated blade masses.

3.3.2 Iterations of 1% GAS SNL100-03 Blade

The structural design iterations of the 1% GAS SNL100-03 blade are rendered in Figure 3-8 with mass and deflection summarized in Table 3-4. The different iterations start with Version 0 and lead up to the final blade design of Version 5CF. The Version 0 blade mimics the full-scale conventional skin-and-spar structural design excluding the third shear web (as mentioned in Section 3.2.4) and is far too heavy even if fabricated with the minimum thickness material allowed by additive manufacturing (it would weigh about 122 grams, which is 2.46 times more than ideal weight). As such, the blade was never fabricated and its high mass highlights the need to explore structural optimization and non-conventional geometries.

To design the structure to minimize the mass and maximize the stiffness, it is important to take into account both the aerodynamic shape of the blade as well as the structural loadings on the blade [41,42]. If only focusing on the aerodynamics, the resulting blade would be a solid blade with an aerodynamic shell. If only focusing on the structure of the blade, the resulting shape would be an I-beam with no external airfoil. Therefore, to fully optimize the blade for mass and stiffness, material must remain where loads act upon it and be removed where loads do not act upon it while simultaneously providing support for the outer shell to retain aerodynamic shape. In terms of material that must remain, the leading edges and trailing edges were unaltered due to their critical influence on aerodynamics [43]. Each design version presented is based upon authors' experience and the previous design results. In terms of material that could be removed, oval holes were employed on the upper and lower surfaces. The rounded corners reduce the stress concentrations as compared to the sharp corners if squares were removed [44] and the removed ovals are spaced evenly down the length of the blade to provide support for the outer shell, polyethylene wrap. This set of design decisions led to structural designs and methodologies similar to the spongy bone of Figure 3-2a, and therefore a bio-inspired structure.

The Version 1 blade takes the same shear web internal structure as Version 0, but removes material in the outer shell. This results in a blade with reasonable stiffness, but still too high of a mass (nearly 50%). The following discusses the remaining structural designs that attempt to match both the mass and stiffness with Table 3-4 summarizing the ground testing results, design considerations, and design successes. The remainder of the design versions are based upon manufacturing iteration and assessment with an emphasis on bio-inspiration.

	SOLIDWORKS Rendition of the Root	Maximum Chord Internal Structure
Version 0	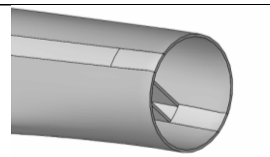	
Version 1	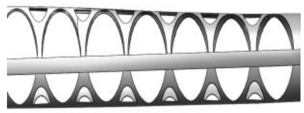	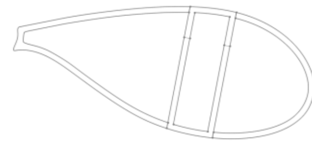
Version 2	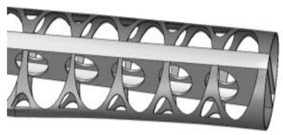	
Version 3 & 3CF	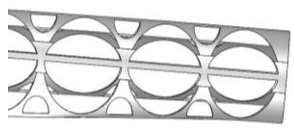	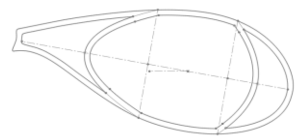
Version 4CF	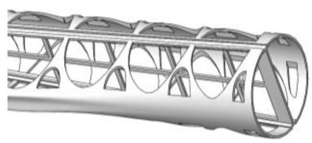	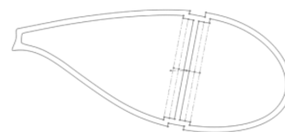
Version 5CF	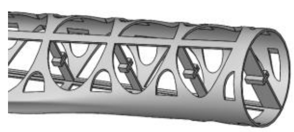	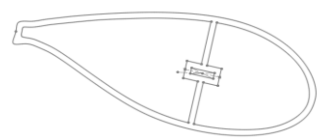

Figure 3-8: Design iterations of the 1% GAS SNL100-03 blade.

Table 3-4: Results of the fabricated 1% GAS SNL blades, by version iteration.

1% GAS SNL Version	Mass (g)	Max. Flap-wise Steady State Tip Deflection (cm)	Primary Material	Design Changes	Design Effect
Ideal	49.5	19.5	(-)	(-)	(-)
Version 1	69.2	17.9	Spar: RGD8530 Lead and Trailing Edges: RGD8525	Material removed from outer surface, full-scale internal structure	Reasonable flap-wise stiffness, too massive
Version 2	65.4	10.0	Spar: RGD8515 Lead and Trailing Edges: RGD8520	Material removed from spar, stiffer material	Too stiff flap-wise, too massive, significantly low edge stiffness
Version 3	54.2	23.3	VeroWhite	Widened spar, stiffest material	Too flexible flap-wise, reasonable mass
Version 3CF	56.2	9.8	VeroWhite	Superficial carbon-fiber spanwise strip	Too stiff flap-wise, reasonable mass
Version 4CF	52.0	7.3	VeroWhite	Single straight spar, carbon fiber on suction side	Too stiff flap-wise, reasonable mass
Version 5CF	51.0	16.45	RGD8505	Less stiff material, single straight spar, carbon fiber down center	Reasonable flap-wise stiffness, reasonable mass

Since the structural design of Version 1 yields too large of a mass, the Version 2 blade removes mass in the spar, also in the shape of ovals, down the length of the blade. This blade is printed with a stiffer material to offset the removal of this material. While there was improvement in the mass of the blade, it is still too massive, deflects too little, and has significantly lower edgewise stiffness (thought, edgewise stiffness is not a priority in the present GAS approach) as summarized in Table 3-4.

Version 3 blade sought to improve upon Version 2 by further invoking a bio-inspired internal structure. The shear webs are widened and rounded and the sizes of the empty spaces are increased in both the external and internal structure. This results in a much-improved mass similar to the ideal blade. However, even when printing with the stiffest material available, the blade is too flexible in the flap-wise direction. In order to increase this stiffness, a carbon fiber strip is superficially attached on the suction side of the blade similar to previous blade designs [13]. This design is denoted as Version 3CF, with the inclusion of carbon fiber indicated by the 'CF'. This addition of carbon fiber significantly increases the stiffness with little mass increase. Succeeding iterations continue to contain a carbon fiber strip. However, further iterations were needed as this blade was too stiff (tip deflection was too small) and too heavy.

Version 4CF employs the carbon fiber, as in Version 3CF, but uses a structure similar to Version 2, except with a singular shear web and a track for placement of the carbon fiber strip. This results in a blade with mass close to the ideal scaled mass, but a stiffness that is too high. Version 5CF continues with the same design, however the carbon fiber placement has been shifted to the middle of the blade. Although the carbon fiber is near the neutral axis (providing minimal changes to the blade inertia), the material stiffness is ~100 times greater than the PolyJet 3D printed materials causing a significant increase in stiffness as compared to a model with no carbon fiber included. The final Version 5CF blade has a total mass error of +3% and a gravo-elastic tip deflection error of -15.6%. The design evolution errors for both the total mass and flapping tip deflection are shown in Figure 3-9 with positive values referring a high mass and deflection.

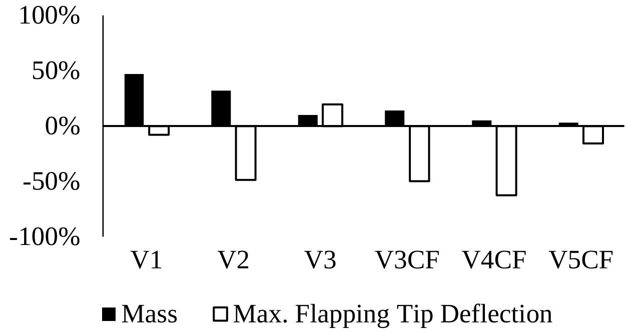

Figure 3-9: Percent difference from scaled values of the SNL100-03 blade of the total mass and maximum steady state tip deflection. Positive values are greater than the target, negative values are less than the target.

To quantify the net improvement in structural design through iteration, the BSSE values (equation (3.14)) are shown in Figure 3-10. As a reminder, the BSSE combines the mass and deflections errors of the designed model, to the ideal model. The closer the BSSE is to zero, the better the design. It can be seen that large changes in structural design did not necessarily reduce the BSSE but allowed for improvements towards the final version, which subsequently had the lowest BSSE. For example, the increase between Version 3 and Version 3CF, is due to the addition of the carbon fiber and helped drive the BSSE to its lowest value for Version 5CF. If the BSSE is zero, then the mass and stiffness of the blade natural flap-wise frequency can be expected to have scaled appropriately. As such, frequency was only measured for the final blade iteration, as discussed below.

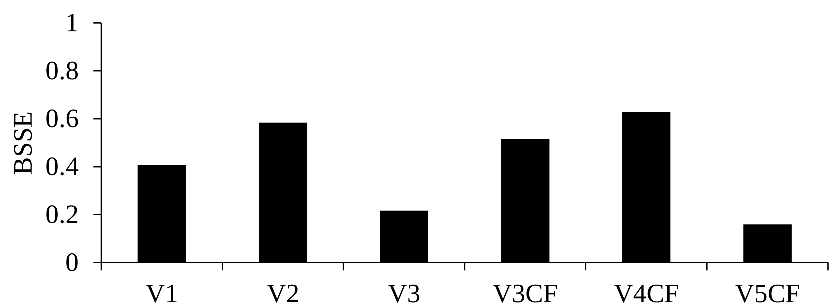

Figure 3-10: The Blade Structural Scaling Error for the design iterations of the 1% GAS SNL100-03 blade which all utilize PolyJet 3D printed materials and polyethylene wrap while the final three versions (denoted with the CF) also contain carbon fiber strips.

3.3.3 Final Version of 1% Scaled Blade

The top view of the final version (5CF) of the scaled wind turbine blade is shown in Figure 3-11. The blade design has similar characteristics as the bone structure in Figure 3-2a. As noted above, this blade has similar total mass and tip deflection properties, which would suggest that flap-wise frequency and stiffness distributions would also be reasonable. The idealized scaled natural flap-wise frequency is 4.9 Hz as shown in Table 3-3. The frequency of the 1% GAS SNL100-03 blade was measured with the technique shown in Figure 3-5a and Figure 3-5b, which yielded 4.5 Hz, an 8.1% decrease from ideal.

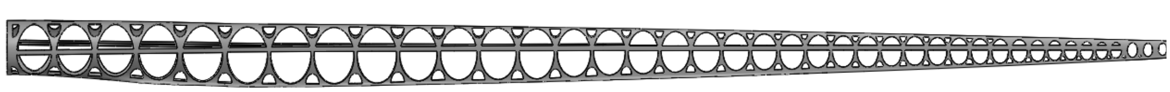

Figure 3-11: The top view of the blade structure of the Version 5CF 1% GAS SNL100-03 blade model.

Figure 3-12a depicts both a portion of the physically printed 1% GAS SNL100-03 blade, and Figure 3-12b shows the blade linear mass density (mass per unit span) over the length of the blade. Since the design has many local variations in the organic structure, the linear density (red squares) oscillates significantly. When these values are smoothed out to get a representative linear density distribution (the red dashed line), the result is similar to that of the ideal scaled values shown as the black solid line. Using the smoothed mass density and equation (3.12) for the radial center of mass of the blades, the full-scale center of mass is at 31.5% span and Version 5CF slightly more outboard at 40.7% span. This difference can be attributed to the higher mass density near the tip of the blade as seen in Figure 3-12b.

a)

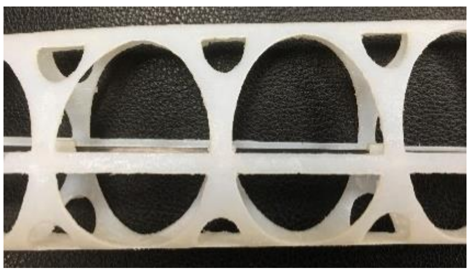

b)

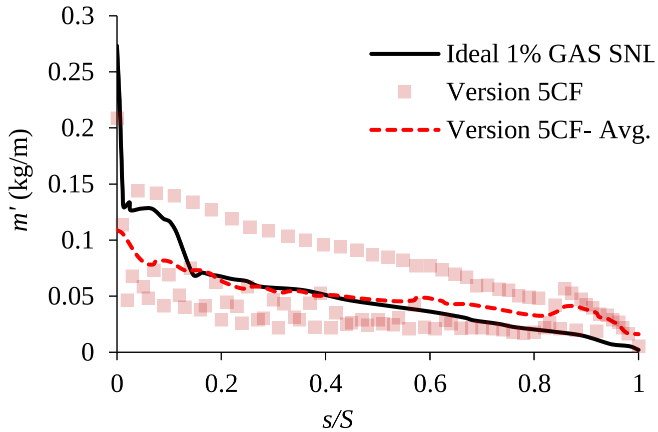

Figure 3-12: Version 5CF blade showing: a) the organic structure and b) discrete and smoothed linear mass density along the span as compared to the ideal 1% GAS SNL100-03 blade.

Fig. 3-13 shows the deflection of the full-scale and sub-scale blade when loaded in the static pull test (Figure 3-5c) with an applied moment using weights, which is consistent with steady-state rated operational conditions. The fabricated and full-scale shapes are similar inboard; however, the scaled blade is too stiff outboard yielding a smaller tip deflection. This is consistent with deflections at the tip of the blade as shown in Figure 3-14 for a range of loads up to the steady-state conditions.

The model deflection being 15.6% too low, correlates to the stiffness being 18.4% too high when following the trends of equation (3.13). This stiffness increase and the mass increase of 3%, applied to equation (3.8b), results in an increased predicted frequency error of 7.2%. However, the measured frequency is 8.1% too low. This can be attributed to the center of gravity being 9% farther out on the span. To improve upon the model, future iterations can remove additional material from outboard on the blade to reduce total mass, reduce outboard mass density, move the center of gravity inboard, and reduce outboard blade stiffness. These consequences may additionally increase the blade natural frequency closer to the target.

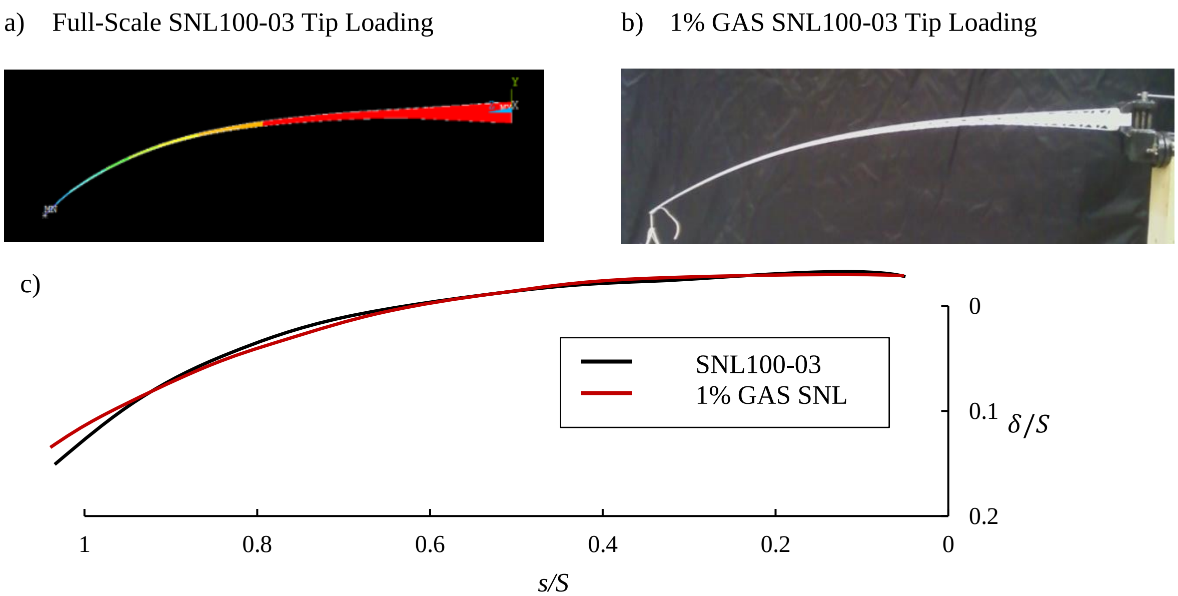

Fig. 3-13. Blade deflection under a steady-state flap-wise load equivalent to average load for rated conditions: a) ANSYS predictions of the full-scale SNL100-03, b) fabricated 1% GAS SNL100-03 blade, and c) a quantitative comparison of non-dimensional deflections.

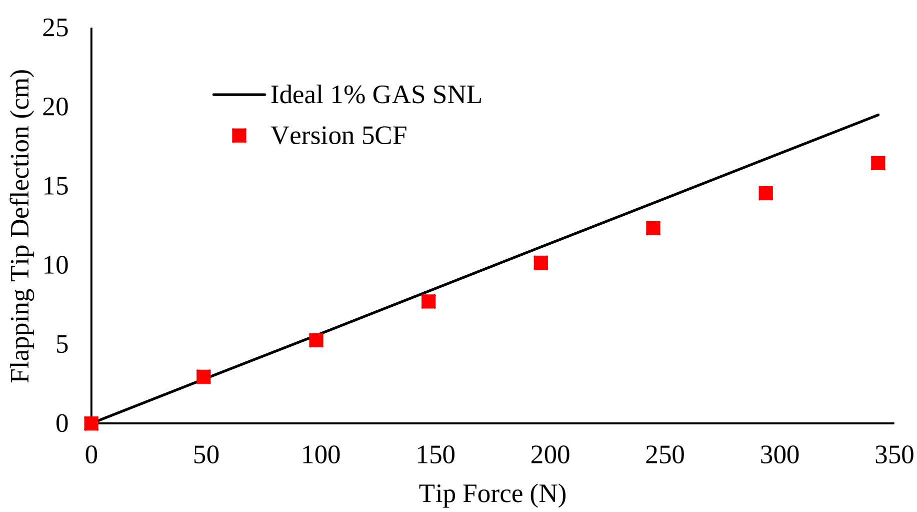

Figure 3-14: The flap-wise tip deflections of the 1% GAS SNL100-03 Version 5CF blade (red squares) compared to ideal scaled model (black line).

3.4 Conclusions and Recommendations

The current study presents a unique approach to structurally scaling wind turbine blades using the gravo-aeroelastic scaling (GAS) applied to a blade from an extreme-scale turbine (rated at 13.2 MW) to design a 1/100th model. The method allows for a low-cost fabricated model that can reflect the proper non-dimensional flap-wise dynamics and elastic deflections of the full-scale blade. The scaling was achieved by reasonably reproducing the non-dimensional flap-wise frequency, tip-deflection, deflection shapes and linear mass density distributions of the full-scale model. Notably, the scaled model requires extremely light mass while maintaining proper stiffness. This was achieved via additive manufacturing, structural designs inspired by bone growth, and the stiffness reinforcement of a carbon fiber spar. The scaling performance of the various blade structural designs were evaluated through gravo-elastic ground tests and quantified by the Blade Structural Scaling Error which considers the differences in total blade mass and blade deflections. The final blade had the lowest BSSE of 0.16 which based on a 3% mass error and a steady flap-wise tip deflection error of 15.6%. This design also had 8.1% error in flap-wise frequency and reasonable representation of linear mass density. However, the model was higher than ideal near the tip causing the center of mass of the blade to be more outboard (at 40.7% span as opposed to ideal at 31.5% span).

Recommendations for future work include the application of the GAS method to field-tested sub-scale rotors to investigate their ability to describe full-scale gravo-aeroelastic dynamics. It is suggested these field scaled tests use a rotor at a larger scale in order to alleviate the Reynolds number effects that would be highly exaggerated in a 1% model. Such work is underway in the form of a 20% scale Segmented Ultralight Morphing Rotor-Demonstrator for ground, parked, and operational testing [45–47]. Additionally, the success in using additive manufacturing with a structurally optimized bio-inspired design is suggested to be further explored for full-scale blades as an option to reduce blade mass while maintaining structural stiffness. Finally, while this study investigates the flap-wise blade performance in terms of structural response, alternate scaling models are proposed to explore the edgewise fatigue or design failures such as panels cracking or leading edge erosion as these are often the design drivers in extreme-scale turbines.

References

[1] U.S. Department of Energy (DOE). “Wind Vision. A New Era for Wind Power in the United States.” 2015, p. 350 pp. doi:DOE/GO-102015-4557.

[2] U.S. Energy Information Administration. “Annual Energy Outlook 2015.” *Office of Integrated and International Energy Analysis*, Vol. 1, 2015, pp. 1–244. doi:DOE/EIA-0383(2013).

[3] Griffith, D. T., and Ashwill, T. D. *The Sandia 100-Meter All-Glass Baseline Wind Turbine Blade : SNL100-00*. 2011.

[4] Griffith, D. T. *The SNL100-01 Blade: Carbon Design Studies for the Sandia 100-Meter Blade*. 2013.

[5] Griffith, D. T. *The SNL100-02 Blade : Advanced Core Material Design Studies for the Sandia 100- Meter Blade*. 2013.

[6] Griffith, D. T., and Richards, P. W. *The SNL100-03 Blade : Design Studies with Flatback Airfoils for the Sandia 100-Meter Blade*. 2014.

[7] Noyes, C., Qin, C., and Loth, E. “Pre-Aligned Downwind Rotor for a 13.2 MW Wind Turbine.” *Renewable Energy*, Vol. 116, 2018, pp. 749–754. doi:10.1016/j.renene.2017.10.019.

[8] Bergami, L., and Madsen, H. “A Two-Bladed Teetering Hub Configuration for the DTU 10 MW RWT: Loads Considerations.” *European Wind Energy*, 2014, pp. 1–8.

[9] Viselli, A. M., Goupee, A. J., and Dagher, H. J. “Model Test of a 1:8-Scale Floating Wind Turbine Offshore in the Gulf of Maine.” *Journal of Offshore Mechanics and Arctic Engineering*, 2015. doi:10.1115/1.4030381.

[10] Singleton, J. D., and Yeager, W. T. “Important Scaling Parameters for Testing Model-Scale Helicopter Rotors.” *Journal of Aircraft*, Vol. 37, No. 3, 2000, pp. 396–402. doi:10.2514/2.2639.

[11] Wan, Z., and Cesnik, C. E. S. Geometrically Nonlinear Aeroelastic Scaling for Very Flexible Aircraft. No. 52, 2013, pp. 1–10.

[12] Jain, A., Robertson, A., Jonkman, J. M., Goupee, A. J., Kimball, R., and Swift, A. H. “FAST Code Verification of Scaling Laws for DeepCwind Floating Wind System Tests.” *Proceedings of the Twenty-second (2012) International Offshore and Polar Engineering Conference*, Vol. 4, No. April, 2012, pp. 355–365.

[13] Campagnolo, F., Bottasso, C. L., and Bettini, P. “Design, Manufacturing and Characterization of Aero-Elastically Scaled Wind Turbine Blades for Testing Active and Passive Load Alleviation Techniques within a ABL Wind Tunnel.” *Journal of Physics: Conference Series*, Vol. 524, No. 1, 2014. doi:10.1088/1742-6596/524/1/012061.

[14] Du, W., Zhao, Y., He, Y., and Liu, Y. “Design, Analysis and Test of a Model Turbine Blade for a Wave Basin Test of Floating Wind Turbines.” *Renewable Energy*, Vol. 97, 2016, pp. 414–421. doi:10.1016/j.renene.2016.06.008.

[15] Robertson, A. N., Jonkman, J. M., Goupee, A. J., Coulling, A. J., Browning, J., Masciola, M. D., and Molta, P. *Summary of Conclusions and Recommendations Drawn from the DeepCwind Scaled Floating Offshore Wind System Test Campaign*. 2013.

[16] Loth, E., Kaminski, M., and Qin, C. “Gravo - Aeroelastic Scaling for Extreme - Scale Wind Turbines.” *AIAA Aviation Conference*, 2017, pp. 1–11.

[17] Kaminski, M., Loth, E., Qin, C., Griffith, D. T., and Scaling, G. “Gravo-Aeroelastic Scaling a 13.2 MW Wind Turbine Blade to a 1-Meter Model.” *AIAA SciTech*, 2018, pp. 1–12.

[18] Shen, W. Z., K Zakkam, V. A., Sørensen, J. N., -, al, Jiang, Y., Liu, S., Zhao, D., Canet, H., Bortolotti, P., and Bottasso, C. L. “Gravo-Aeroelastic Scaling of Very Large Wind Turbines to Wind Tunnel Size.” 2018, p. 42006. doi:10.1088/1742-6596/1037/4/042006.

[19] Aage, N., Andreassen, E., Lazarov, S., and Sigmund, O. “Giga-Voxel Computational Morphogenesis for Structural Design.” *Nature Publishing Group*, Vol. 550, 2017. doi:10.1038/nature23911.

[20] Wolff, J. *The Law of Bone Remodelling*. Springer, 1986.

[21] Thierry, B., Singh, M., and Kaumanns, W. “Who’s Afraid of the Big Bad Wolff?: ‘Wolff’s Law’ and Bone Funcational Adaptation.” *New York Cambridge University Press*, Vol. 1, No. May, 2004, pp. 80–83. doi:10.1002/ajpa.

[22] Campbell, Thomas Williams, Christopher Ivanova, Olga Garrett, B. “Could 3D Printing Change the World? Technologies, Potential, and Implications of Additive Manufacturing.” No. October, 2011, pp. 3–7.

[23] *More than 3D Printing. Design. Materials. Production*. 2017.

[24] Bishop, P. J., Hocknull, S. A., Clemente, C. J., Hutchinson, J. R., Farke, A. A., Beck, B. R., Barrett, R. S., and Lloyd, D. G. “Cancellous Bone and Theropod Dinosaur Locomotion. Part I—an Examination of Cancellous Bone Architecture in the Hindlimb Bones of Theropods.” *PeerJ*, 2018. doi:10.7717/peerj.5778.

[25] Brookes, K. J. A. “Europe Salutes Metal-Based AM.” *Metal Powder Report*, Vol. 73, No. 3, 2018, pp. 119–125. doi:10.1016/j.mprp.2018.02.004.

[26] Make, M., and Vaz, G. Analyzing Scaling Effects on Offshore Wind Turbines Using CFD. Renewable Energy, 83, 2015, pp. 1326–1340.
[27] Martin, H. R., Kimball, R. W., Viselli, A. M., and Goupee, A. J. “Methodology for Wind/Wave Basin Testing of Floating Offshore Wind Turbines.” 2014. doi:10.1115/1.4025030.
[28] Li, L., Gao, Y., Hu, Z., Yuan, Z., Day, S., and Li, H. “Model Test Research of a Semisubmersible Floating Wind Turbine with an Improved Deficient Thrust Force Correction Approach.” *Renewable Energy*, Vol. 119, 2018, pp. 95–105. doi:10.1016/j.renene.2017.12.019.
[29] Barker, A., Timco, G., Gravesen, H., and Vølund, P. “Ice Loading on Danish Wind Turbines. Part 1: Dynamic Model Tests.” *Cold Regions Science and Technology*, Vol. 41, No. 1, 2005, pp. 1–23. doi:10.1016/j.coldregions.2004.05.002.
[30] Post, B. K., Lind, R. F., Lloyd, P. D., Kunc, V., Linhal, J. M., and Love, L. J. “The Economics of Big Area Additive Manufacturing.” *Proceedings of the solid Freeform Fabrication Symposium*, 2016, pp. 1176–1182.
[31] Guo, N., and Leu, M. C. “Additive Manufacturing: Technology, Applications and Research Needs.” *Frontiers of Mechanical Engineering*, Vol. 8, No. 3, 2013, pp. 215–243. doi:10.1007/s11465-013-0248-8.
[32] Stratasys. “Digital Materials Data Sheet.” 2000.
[33] The Composites Store. http://www.cstsales.com/.
[34] GLAD Cling Wrap. https://www.glad.com/food-storage/plastic-wrap/clingwrap/.
[35] Foreman, J., Gill, P. S., and Sauerbrunn, S. R. *Tensile Modulus of Plastic Films*.
[36] Liang1, Q. Q., Xie1, Y. M., and Steven2, G. P. “Optimal Selection of Topologies for the Minimum-Weight Design of Continuum Structures with Stress Constraints.”
[37] Aulig, N., and Olhofer, M. “Evolutionary Computation for Topology Optimization of Mechanical Structures: An Overview of Representations.”
[38] “2 - Blades (Carbon Fibre), 1 . 8 Metre Diameter & Induction Motor to PMA Conversion.”
[39] Jamieson, P. *Innovation in Wind Turbine Design*. Wiley, 2011.
[40] Loth, E., Steele, A., Ichter, B., Selig, M. S., and Moriarty, P. Segmented Ultralight Pre - Aligned Rotor for Extreme - Scale Wind Turbines. 2012.
[41] Pourrajabian, A., Nazmi Afshar, P. A., Ahmadizadeh, M., and Wood, D. “Aero-Structural Design and Optimization of a Small Wind Turbine Blade.” *Renewable Energy*, 2016. doi:10.1016/j.renene.2015.09.002.
[42] Wakayama, S. R. *Lifting Surface Design Using Multidisciplinary Optimization*. 1995.
[43] Gaudern, N. A Practical Study of the Aerodynamic Impact of Wind Turbine Blade Leading Edge Erosion. 2014.
[44] Motok, M. D. “Stress Concentration on the Contour of a Plate Opening of an Arbitrary Corner Radius of Curvature.” *Marine Structures*, 1997. doi:10.1016/s0951-8339(96)00012-3.
[45] Ananda, G. K., Bansal, S., and Selig, M. S. “Aerodynamic Design of the 13.2 MW SUMR-13i Wind Turbine Rotor.” *AIAA SciTech Forum*, 2018. doi:10.2514/6.2018-0994.
[46] Bay, C. J., Damiani, R., Jay Fingersh, L., Hughes, S., Chetan, M., Yao, S., Todd Griffith, D., Ananda, G. K., Selig, M. S., Zalkind, D. S., Pao, L. Y., Martin, D., Johnson, K. E., Kaminski, M., and Loth, E. “Design and Testing of a Scaled Demonstrator Turbine at the National Wind Technology Center.” *AIAA Scitech Forum*, 2019.
[47] Yao, S., Griffith, D. T., Chetan, M., Bay, C. J., Damiani, R., Kaminski, M., and Loth, E. “Structural Design of a 1/5 Th Scale Gravo-Aeroelastically Scaled Wind Turbine Demonstrator Blade for Field Testing.” *AIAA SciTech*, 2019, pp. 1–9. doi:10.2514/6.2019-1067.

4. Gravo-Aeroelastic Scaling of a 13-MW Downwind Rotor for 20% Scale Blades

Abstract:

A 105-meter, 13-MW two-bladed downwind Segmented Ultralight Morphing Rotor (SUMR-13) blade was gravo-aeroelastically scaled by 20% to a 20.87-meter-long demonstrator blade and confirmed through structural ground testing. The sub-scale model was achieved through geometric scaling and by aeroelastic scaling principles based on operational flapwise deflections combined with rotational and structural frequencies while retaining the turbine tip-speed ratio. In particular, the sub-scale demonstrator was designed to replicate, as closely as possible, the non-dimensional geometry, the ratio of centrifugal to gravitational moments, the tip-speed ratio, and the non-dimensional rotation rate. The intent for this demonstrator was to achieve the same non-dimensional flap-wise blade deflections and dynamics of the full-scale 13-MW rotor. The manufactured SUMR-D blade resulted in less than half of the mass of the conventional Controls Advanced Research Turbine (CART2) rotor blade based on scaling and a lower power rating, though with some differences in mass and stiffness from the ideal scaled-down design to meet safety requirements at the test site. To achieve proper scaling, operational pitch control set points were altered to account for the differences by evaluating simulated operation of both the SUMR-13 and SUMR-D rotors. Structural-testing of the SUMR-D blade investigated the response to well-defined flap-wise loads and indicated that the sub-scale blade had the appropriate elastic properties needed for both scaling and for safe operational field testing.

Nomenclature

α	=	axial induction factor
α_n	=	constant blade property
a_{air}	=	speed of sound in air
c	=	chord length
c_x	=	coefficient
EI	=	blade stiffness
F	=	force
Fr_{moment}	=	moment based Froude number
g	=	gravitational constant
m	=	blade mass
M	=	moment
Ma	=	Mach number
P	=	applied load
r	=	distance
Re	=	Reynolds number
s	=	spanwise location
S	=	total blade length
t	=	material thickness
U	=	wind speed
x,y,z	=	cartesian space coordinates
β	=	pre-cone angle
δ	=	deflection
η	=	scaling factor
λ	=	tip-speed ratio
μ	=	viscosity
θ	=	blade pitch
ρ	=	density
τ	=	shaft tilt
ψ	=	azimuthal angle
Ω	=	rotational speed
ω_{flap}	=	flapwise frequency

Subscripts

$()_{\mathrm{adapter}}$	=	adapter value
$()_{\mathrm{c}}$	=	centrifugal
$()_{\mathrm{f}}$	=	full-scale value
$()_{\mathrm{g}}$	=	gravitational
$()_{\mathrm{hub}}$	=	hub value
$()_{\mathrm{p}}$	=	power
$()_{\mathrm{Q}}$	=	centrifugal, thrust, or gravitational value
$()_{\mathrm{q}}$	=	torque
$()_{\mathrm{rated}}$	=	rated value
$()_{\mathrm{rms}}$	=	root-mean-square about mean
$()_{\mathrm{s}}$	=	sub-scale value
$()_{\mathrm{t}}$	=	thrust
$()_{\mathrm{tip}}$	=	tip value
$()_{\mathrm{wind}}$	=	wind value
$()_{xx}$	=	non-dimensional spanwise location
$()_1$	=	Reference Frame 1
$()_2$	=	Reference Frame 2
$()_3$	=	Reference Frame 3

Superscripts

$()'$	=	spanwise distributed value
$\overline{()}$	=	non-dimensional value

4.1 Introduction

Over time, the power produced by wind turbines has improved by increasing the rotor swept area. In particular, rotor diameters have been progressively growing larger with a 135% growth from 1998 to 2017 leading to an average rotor diameter of 113 meters in 2017 [1]. Predictions show that wind turbines will continue this upward trend, and rotors of such significant size will be denoted as extreme-scale rotors and have a rated power of 10 MW and above [2]. The design of the next-generation extreme turbines, which incorporate nonconventional concept designs and/or high blade flexibility and high load angles, will require ever more important attention to aeroelastic characteristics and associated load control performance. Whereas numerical simulations could, in principle, be used to investigate these extreme-scale rotors, their complex dynamics (coupled with large deflection angles and low blade natural frequencies) are not typically present in conventional rotors and are still a challenge for most computational methods. Therefore, ad hoc sub-scale experimental models are critical to understanding the dynamics and performance of the full-scale systems without the cost penalty of the full-scale prototype. Ideally, this scaling includes the influence of all the aerodynamic, gravitational, and inertial loads on the blades with a control scheme that can replicate the blade response and dynamics in turbulent field operational conditions. While this type of comprehensive gravo-aeroelastic scaling has never been demonstrated for extreme-scale wind turbines (the subject of the current investigation), other types of scaling has been applied to wind turbines with different objectives.

For example, the DeepCwind project sought to investigate full-structure dynamics of floating wind turbines via hydrodynamic and aerodynamic scaling [3–5]. This project developed testing platforms, starting with a 1/50 scale model of a 5-MW upwind three-bladed turbine in a variety of wind/wave conditions in a water basin [5]. Another example is the VolturnUS project, a one-eighth scaled floating wind turbine based on a full-scale 6-MW turbine with a 152-meter diameter [3,4,6]. Each of these turbines were Froude-scaled to match the ratio of the aerodynamic and wave loads on the structure dynamics of the entire turbine. Such wind-wave dynamics are of key interest for a floating turbine; however, for a fixed-bottom extreme-scale turbine, as is considered herein, the rotor blade dynamics and vibrations are of greater significance to turbine design than the wind-wave interactions. These dynamics are heavily influenced by the nonlinear combination of aerodynamic, centrifugal, and gravitational forces related to structural stiffness and blade mass and cannot be accurately scaled by solely matching the aerodynamic loadings [7].

The National Renewable Energy Laboratory’s Unsteady Aerodynamic Experiments [8] that included the use of a 10-meter diameter, 20-kW, downwind rotor, is another scaling project available in the literature. This project provides highly valuable information with respect to blade aerodynamics; however, the relatively stiff blades did not replicate the coupled dynamics associated with the longer and more flexible blades of extreme-scale rotors.

Finally, the Scaled Wind Farm Technology (SWiFT) V27 rotors are being scaled for similar solidity and aerodynamics as megawatt-scale rotors to have similar induction factors and power coefficients, in order to replicate rotor loads and wake deficits while also scaling the distance between turbines [9,10]. This approach allows for the high-fidelity, field-based investigation of turbine-to-turbine wake interaction. This example of scaling is important to understand how conventionally designed turbines can behave and interact in a wind farm however, the SWiFT scaling does not consider the aeroelasticity of the blades themselves.

Thus, a new type of scaling is needed to design sub-scale rotors that can capture the complex nature of highly flexible rotor blades for testing purposes. Gravitational and aerodynamic loadings, as well as blade stiffness, must all be considered, thus we make use of the Gravo-Aeroelastic Scaling (GAS) method [11]. The GAS approach was recently applied to a 1-meter blade to achieve a 1% structurally tested scale model of the 100-meter SNL100-03 [12]. The sub-scale additively manufactured 1-meter blade model rotor [13] reasonably matched non-dimensional mass and stiffness of the 100-meter blade; however, this small-scale blade demonstration was simply a proof of concept of the scaling methodology and did not include any planned operational testing on an actual turbine.

The objective of this study was to develop a 1/5$^{\text{th}}$ gravo-aeroelastically scaled model of the Segmented Ultralight Morphing Rotor 13-MW (SUMR-13) turbine [14–16] to exhibit the same flapwise deflections and dynamics at high loadings (between rated and cut-out wind speeds). The 20.87-meter-long demonstrator blade made use of the same airfoils as the full-scale blade in order to preserve aeroelastic characteristics. Ground testing and numerical simulation of operational conditions are used to investigate the blade scaling methodology [17,18]. The scaled rotor is denoted the SUMR-Demonstrator (SUMR-D) [19] and was designed for operational field testing on a research turbine and employs the GAS method previously employed for a 1% model [13] but with modifications due to safety constraints for operational (flight) testing at the National Renewable Energy Laboratory’s Flatirons Campus (NREL FC) on the two-bladed Controls Advanced Research Turbine (CART2) [20,21]. To retain the desired scaled aeroelastic dynamics with the non-ideal blade mass and stiffness, controller set points are altered to achieve an aeroelastically scaled blade. To the authors’ knowledge, in the open literature, this is the first gravo-aeroelastic-scaling of downwind rotors suitable for field testing that can represent the full-scale deflections and the first flapwise mode of an extreme-scale turbine.

This approach can be used in the future to reduce the cost of experimental field assessment of advanced technology for other extreme-scale wind turbines and precedes a field test campaign to verify the included scaling approach.

Section 4.2 explains the GAS method, the structural testing facility, the expected field testing platform, and control system, as well as the simulation software used for comparisons. Section 4.3 includes the results and discussions of the scaling and manufacturing of the SUMR-D blade, the structural testing measurements and predictions, as well as the predicted operational dynamics of SUMR-D compared to the full-scale turbine. Finally, Section 4.4 provides concluding remarks and recommended direction of future testing.

4.2 Methods

4.2.1 Ideal GAS Scaling

The key geometric ratio use herein for scaling is the ratio of sub-scale blade-length (S_s) to full-scale blade length (S_f). For aerodynamic scaling, the key scaling is blade radius including the hub radius and turbine coning angle. Since the coning angle will be preserved, the blade length will be a unique function of the blade radius and thus is generally used for scaling. In general, all external blade dimensions would employ this linear scaling factor such that the airfoil cross-sectional shape and local twist angles are preserved as a function of non-dimensional spanwise length (*s/S*), where *s* is the spanwise distance along the blade.

$$\eta = \frac{S_s}{S_f} \tag{4.1}$$

Having applied this scaling method to the blade planform (which thus uses the same airfoil distribution as the full-scale blade), the scaled model is considered a "geometrically" scaled blade. Whereas this affects the aerodynamics due to Reynolds number mismatch (as will be clarified in Section 4.3.1) it provides the opportunity to retain the airfoil thickness to chord ratio and the blade structural internal architecture.

While this scaling ratio is based on rotor length and primarily applied to the rotor geometry, other portions of the turbine utilize this ratio. For example, the scaled blades are ideally mounted on a tower and drivetrain that are also geometrically scaled[11,13]; however, if the blades are to mount to a pre-existing system (e.g., the CART2), the non-dimensional hub-radii, as well as the shaft tilt and coning angles may be different from the full-scale values. In this case, one needs to carefully consider the moments the blade experiences and the aerodynamic and structural natural frequencies to achieve the best possible similitude for operational dynamics on the scaled model. Moreover, fabrication issues, testing center restrictions, and actual environmental conditions to be contended with may prevent the ideal scaling from being achieved in full. For example, the NREL FC requires rotors to be able to withstand the high wind speeds typical of the site (where gusts in excess of 40 m/s are common each year). Before considering all these practical issues, we will address the key factors that must be accounted for to achieve proper gravo-aeroelastic scaling.

First and foremost, flap-wise bending moments should be appropriately scaled due to their major impact on the out-of-plane deflections and vibrations of extreme-scale rotors [22]. Figure 4-1 depicts the different components of the flap-wise moments experienced by the blades during operation with three different coordinate frames. Figure 4-1a is a side view of the entire system, Figure 4-1b is a side view of the rotor and hub configuration, and Figure 4-1c is a front view of the turbine, where the viewpoint is facing downwind. There are three x,y,z coordinate systems to describe the transformation from sectional forces on the blades (F_Q) to the sectional flapwise bending moments (M'_Q) where Q is a generic variable representing either centrifugal (c), gravitational (g), or thrust (t) components. Frame (1) is non-rotating and attached to the nacelle, Frame (2) is rotating and attached to the hub and accounts for shaft tilt, and Frame (3) is rotating, at rotor speed, Ω, and attached to the blade root. Subscripts (1, 2, and 3) refer to the specific frame. These frames account for: β, blade pre-cone angle; τ, shaft tilt; ψ, azimuth position; $r_{adapter}$, blade-root connection and coning adapter offset; r_{hub}, hub radius; and U, incoming wind speed. Transformations and further explanations of the coordinate systems are found in Figure 4-1.

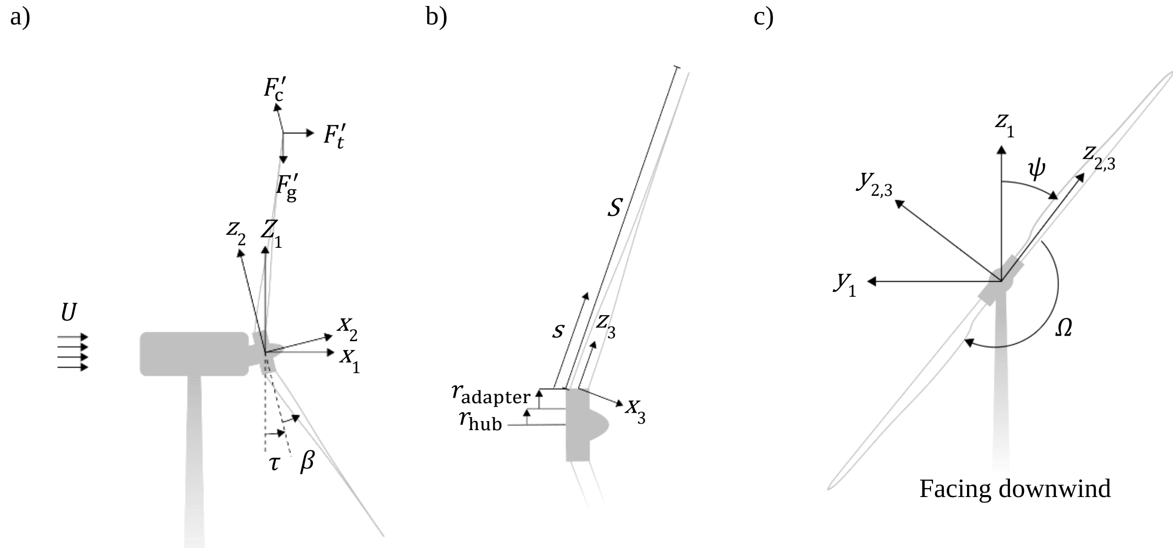

Figure 4-1: Turbine coordinate systems, parameters, and moments felt at the root from a) the side view, b) the hub and blade configuration, and c) the front view facing downwind

To match the angles between the rotor plane and the inflow velocity vector in a rotational frame, the sub-scale rotor must have the same tip-speed ratio as the full-scale rotor, where the ratio is defined as:

$$\lambda = \frac{\Omega[r_{\text{hub}} + r_{\text{adapter}} + S * \cos\beta]}{U} \tag{4.2}$$

This scaling also ensures that the aerodynamic performance is reasonably maintained since the power coefficient for a given geometry depends primarily on tip-speed ratio and blade pitch angle (θ) assuming negligible Reynolds number effects.

Next, the scaling considers the angles of root flap-wise bending moments as a function of azimuthal angle. These angles are related to the ratios of the various moment components, which are, in turn, related to the forces acting on the blade. The main forces per unit span imparted on the blades are generally defined as (F_Q') occurring at blade length locations (s), which can range from the root (s = 0) to the blade tip (s = S). Equations (4.3)-(4.5) define these three forces with the following additional parameters: m', blade mass density; Ω, rotational speed; g, the gravitational constant; ρ_{wind}, air density; U, wind speed; a, axial induction factor; and the sectional airfoil characteristics of coefficient of thrust (c_t) and chord (c). The centrifugal force is expressed in Frame (2) and along the z_2-direction while the gravitational and thrust forces are expressed in Frame (1) in the z_1- and x_1-directions respectively.

$$F_c' = \langle m'\Omega^2(r_{\text{hub}} + r_{\text{adapter}} + s * \cos\beta) \rangle\, \hat{z}_2 \tag{4.3}$$

$$F_g' = \langle -m'g \rangle\, z_1 \tag{4.4}$$

$$F_t' = \left\langle \frac{1}{2}\rho_{\text{wind}} c_t c (U^2(1-a)^2 + [\Omega\{r_{\text{hub}} + r_{\text{adapter}} + s * \cos(\beta-\tau)\}]^2) \right\rangle \hat{x}_1 \tag{4.5}$$

The forces are transformed into Frame (3) in the flap-wise (x_3-) direction. The respective sectional contribution to root flapwise bending moments (M_Q') are found in Equations (4.6)-(4.9) in the y_3-direction. The blade flapwise moments are in a rotating frame and therefore depend on the blade azimuthal angle (ψ). Equation (4.9) integrates these sectional root flapwise bending moments to yield total root moments.

$$M_c' = \langle -sm'\Omega^2[r_{\text{hub}} + r_{\text{adapter}} + s * \cos\beta] * \sin\,\beta \rangle\, \hat{y}_3 \tag{4.6}$$

$$M'_{\mathrm{g}} = \langle m' g\, s\, [\cos(\beta)\sin(\tau) + \sin(\beta)\cos(\psi)\cos(\tau)]\rangle\, \hat{y}_3 \tag{4.7}$$

$$M'_{\mathrm{t}} = \Big\langle \frac{1}{2}\rho_{\mathrm{wind}} c_{\mathrm{t}} c (U^2_{\mathrm{rated}} + [\Omega\{r_{\mathrm{hub}} + r_{\mathrm{adapter}} + s * \cos(\beta - \tau)\}]^2) * \{\cos(\tau)\cos(\beta) - \sin(\tau)\cos(\psi)\sin(\beta)\}\Big\rangle\, \hat{y}_3 \tag{4.8}$$

$$M_{\mathrm{Q}} = \int_0^S M'_{\mathrm{Q}}\mathrm{d}s \tag{4.9}$$

With the blade in the Ψ=0 position, a total rotational blade moment Froude number (Fr_{moment}) is found by integrating the blade length from s = 0 to $s = S$ as defined by the ratio in Equation (4.10) based upon the centrifugal and gravitational moments.

$$Fr_{\mathrm{moment}} = \frac{\Omega^2[r_{\mathrm{hub}} + r_{\mathrm{adapter}} + S\cos\beta]\sin\beta}{g\,[\cos(\beta)\sin(\tau) - \sin(\beta)\cos(\tau)]} \tag{4.10}$$

Keeping this rotational Froude number fixed between the sub-scale and full-scale turbines ensures the ratio of net centrifugal to net gravitational loads, and associated angles, scale appropriately. Note that if one were to be able to preserve the coning angle (β), the shaft tilt (τ), and the non-dimensional hub and adapter radii (r_{hub}/S and r_{adapter}/S) between the full-scale and sub-scale turbines, then fixing this Froude number is equivalent to fixing the ratio (Ω^2/g). As such, Equation (4.10) can be used to determine the appropriate rpm of the scaled turbine at rated conditions, which scales with $\eta^{-1/2}$. Applying the rotor speed scaling and the assumption of an appropriately scaled rotor radius (including hub radius, adapter length, blade length, and coning angle) to Equation (4.2) and keeping the tip-speed ratio constant between the full- and sub-scale models, the sub-scale wind speed is scaled by $\eta^{1/2}$.

To match the non-dimensional flapwise deflections and dynamics of the full-scale system, one must also consider the aeroelastic response of the blade to these moments. It is therefore important to preserve the non-dimensional sectional mass density as a function of s/S such that the spanwise inertial distribution is consistently scaled with aerodynamic forces. This can be achieved by normalizing by the air density and spanwise lengths as

$$\overline{m'} = \frac{m'}{\rho_{\mathrm{wind}} S^2} \tag{4.11}$$

Holding $\overline{m'}$ as a function of s/S constant, while also matching Fr_{moment} of Equation (4.10), ensures that the local ratio of gravitational to centrifugal moments correctly scaled as well.

The next ratio to ideally hold constant is the non-dimensional rotation rate ($\bar{\Omega}$). This ratio is critical for aeroelastic dynamics since the dimensional natural flap-wise frequency (ω_{flap}) determines the level of response of the blade to imparted forces and frequencies, where the latter is primarily driven by the rotating frequency set by the fixed tip-speed ratio of Equation (4.2). The dimensional flapwise natural frequencies and non-dimensional rotation rate are given below, where the latter is rotor angular speed, Ω, normalized by the flapwise natural frequencies and the former is based on the blade structural response as a function of: α_n, a constant which is based on boundary conditions and blade property distributions; EI, the total blade flapwise stiffness; m, the total mass; m', blade mass distribution; and S, and the total blade length.

$$\omega_{\mathrm{flap}} = \alpha_n^2\sqrt{\frac{EI}{mS^4}} \tag{4.12}$$

$$\bar{\Omega} = \frac{\Omega}{\omega_{\mathrm{flap}}} \tag{4.13}$$

The blade natural frequency may vary due to centrifugal stiffening and is therefore a function of the rotational speed of the rotor as well has the length of the hub radius, and thus only taken at the rated conditions for the purpose of ideal scaling.

Since the stiffness varies considerably along the length of the blade, ensuring matched blade deflection also requires the non-dimensional sectional stiffness be preserved as a function of *s/S*. To retain deflection angles between the sub-scale and full-scale, the non-dimensional stiffness per unit length must be preserved.

$$\overline{EI'} = \frac{EI'}{\rho_{\text{wind}} g S^5} \tag{4.14}$$

This η^5 scaling, along with Equations (4.2) and (4.11), ensures that the flapwise tip deflection per span (*s/S*) is preserved between the sub-scale and full-scale models per Euler-Bernoulli beam theory and further assures that the relative influence of gravitational, thrust, and centrifugal loads on this deflection are preserved.

If the same materials are employed for both the sub-scale and full-scale model (such that *E* is held constant), one may use the theory of thin-walled tubes, whereby the matching of the deflection angles for a scaled load leads to an η^2 scaling relationship of wall thickness [2].

Based on the derivations in this section, the scaling parameters are summarized in Table 4-1 where the subscripts *s* and *f* represent the sub-scale and full-scale models, respectively.

Table 4-1: Scaling parameters for GAS in terms of the scaling factor (η)

Scaling Parameter	Scale Factor
Length Scaling: $\frac{S_s}{S_f}$	η
Rotational Scaling: $\frac{\Omega_s}{\Omega_f}$	$1/\sqrt{\eta}$
Wind Velocity Scaling: $\frac{U_s}{U_f}$	$\sqrt{\eta}$
Total Blade Mass Scaling: $\frac{m_s}{m_f}$	$\left(\frac{\rho_{\text{wind,s}}}{\rho_{\text{wind,f}}}\right)\eta^3$
Distributed Blade Mass Scaling: $\frac{m'_s}{m'_f}$	$\left(\frac{\rho_{\text{wind,s}}}{\rho_{\text{wind,f}}}\right)\eta^2$
Flapwise Frequency Scaling: $\frac{\omega_{\text{flap, s}}}{\omega_{\text{flap, f}}}$	$1/\sqrt{\eta}$
Stiffness Scaling: $\frac{(EI')_s}{(EI')_f}$	$\left(\frac{\rho_{\text{wind,s}}}{\rho_{\text{wind,f}}}\right)\eta^5$
Reynolds Number Ratio: $\frac{Re_s}{Re_f}$	$\left(\frac{\rho_{\text{wind,s}}}{\rho_{\text{wind,f}}}\right)\left(\frac{\mu_{\text{wind,f}}}{\mu_{\text{wind,s}}}\right)\eta^{3/2}$
Mach Number Ratio: $\frac{Ma_s}{Ma_f}$	$\left(\frac{a_{\text{wind,f}}}{a_{\text{wind,s}}}\right)\sqrt{\eta}$

If all the ratios in Table 4-1 are matched and the operational controller is suitably adjusted, then the first-order flapwise dynamics and deflection angles will be preserved. Higher order frequencies as well as edgewise and twistwise modes generally require additional scaling, but these other modes will be considered to see how much they change. The accuracy of this flapwise scaling can be evaluated by investigating the non-dimensional first flapwise mode shape as well as the mean operational tip deflections and the RMS deviations about said mean. The non-dimensional flapwise and edgewise deflections respectively and the subscript -tip describes the deflections at the tip of the blade. Do note, torsional deflections are based on blade length as

$$\bar{\delta}_{\text{flap}} = {}^{\delta_{\text{flap}}}/_{S} \tag{4.15a}$$

$$\bar{\delta}_{\text{edge}} = {}^{\delta_{\text{edge}}}/_{S}. \tag{14b}$$

Torsional deflections, $\bar{\delta}_{\text{tor}}$, are reported with units of degrees, and therefore normalization is not used.

It is also important to note the Reynolds and Mach numbers will generally not be held constant when large-scale turbines are scaled down to experimental demonstrators, which can impact the aerodynamic response. In addition, fabrication issues, site platforms and testing requirements may not allow these parameters to be ideally set. Therefore, some adjustments to controller set points may be needed to best match the mean value and its deviations of the deflections of Equations (4.15a) to test the accuracy of scaling. Such adjustments can be made specific to the rotor and test site.

4.2.2 Full-Scale Rotor Model and Site

The SUMR-13 rotor is a two-bladed, downwind design with a morphing hinge at the root and individual pitch control [15,22–25]. The airfoil distribution and four shear webs of the SUMR-13 blade are shown in the wireframe representation of Figure 4-2. The turbine is designed for International Electrotechnical Commission (IEC) Class IIB wind speeds at sea level conditions what are appropriate to deployment in the Dominion power offshore lease zone off the coast of Virginia, which has an average wind speed of about 8.5 m/s at a 90-meter hub height [26]. Due to its highly flexible nature, the lowest frequency is the first edgewise frequency mode where the second lowest is a flapwise dominated mode.

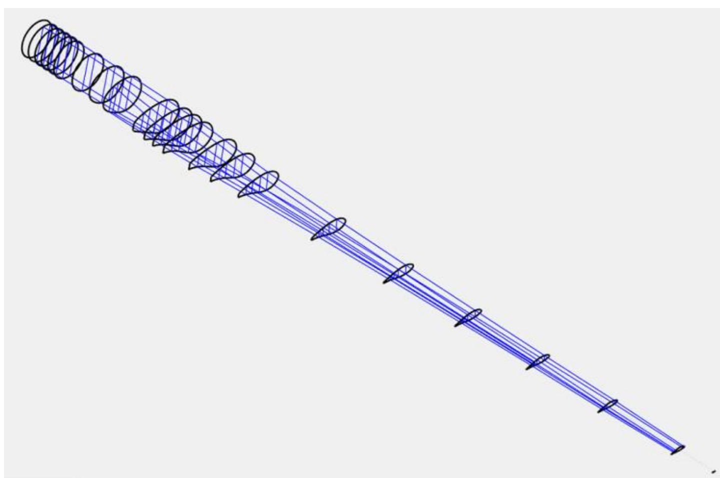

Figure 4-2: Wireframe representation of the SUMR-13 blade

4.2.3 Test Facility and Platform

The SUMR-D blades are mounted on the CART2 at the NREL FC. The NREL FC provides IEC Class IA wind speeds with a 50-year gust of 70 m/s, mean air density of 0.96 kg/m^3, and a turbulence intensity of 0.18. The CART2 testing platform is a two-bladed, land-based upwind turbine. The SUMR-D is a downwind rotor and therefore the CART2 must operate in a downwind configuration [27]. The SUMR-D test was conceived with no morphing hinge but a blade root adapter to create a constant 12.5-degree coning angle. Additionally, the CART2 turbine has a 3.77-degree shaft tilt and the ability to teeter, each not present in the SUMR-13 rotor; however, the application of a teeter brake eliminates the teeter degree of freedom. The blades and drivetrain are outfit with sensors such as: a camera at the root with three reflectors for distributed spanwise displacement, strain gauges distributed down the blade length, rpm, shaft torque encoders, and blade root moments.

4.2.4 Blade Input Files

There are three digital input files for the SUMR-D and SUMR-13 rotors: a FAST model, a BMODES model, and an ANSYS model. The ANSYS model was based on the prefabricated design of the blade [18] (denoted as SUMR-D Pre-Fab), and was used to compare to structural tests. The FAST and BMODES models were based on the fabricated blade, which have slightly higher mass than the original design (noted simply as SUMR-D). The FAST blade model was used for comparing the operational dynamics between the SUMR-13 and SUMR-D. All structural properties (mass and stiffness) were also reported from the FAST model. The BMODES model was also used for obtaining the blade frequencies and mode shapes. Table 4-2 summarizes the input, analysis, and output from the computational approaches used to evaluate the fidelity of the scaling in simulated operational conditions.

Table 4-2: Outline of the simulations performed and their respective input files, analysis software, and output obtained

	Structural Test Simulation	**Operational Simulation**	**Blade Structural Characteristics**
Input	NuMAD file from prefabricated blade design	Fabricated Digital Twin and SUMR-D Operational Controller	Fabricated Digital Twin
Analysis	Load vs. Time Results ANSYS	FAST: Aerodynamics and Blade Dynamics BMODES: Structural Frequencies	FAST: Blade Structures
Output	Static Deflection vs Time	Wind Speeds, Unsteady Flapwise Tip Deflections, C_p, C_q, Tip-Speed Ratio, rpm, Natural Frequency	Mass Density, Sectional Stiffness

4.2.5 Ground-Based Structural Testing Procedure

To determine the natural flapwise frequency, one of the manufactured blades was tested through an impact hammer test. To determine the stiffness response and safety limits, the blades underwent a static pull-test to ensure the blades can withstand predicted extreme static flap-wise loads. With the blade root fixed to a test-stand, loads were applied at three stations along the span (28%, 50%, and 74.5%) and ramped from 0N up to the target loads, held at the target load for at least 10 seconds, then gradually removed. The maximum blade loads at these locations were calibrated to render the scaled moment distribution calculated for Design Load Case (DLC) 6.2 based on FAST simulations [17] and IEC 61400-1 prescriptions [28]. while the wind turbine to extreme loads, due to the combination of the 50-year gust wind speeds and a unlimited large yaw errors (simulating a fault). Out load simulations showed proved that DLC 6.2 is the main ultimate limit-state design driver. The applied loads are in addition to the blade weight contributions for the total loads. Figure 4-3 shows the testing setup. Deflections were measured at 26%, 48%, and 74.5% spans.

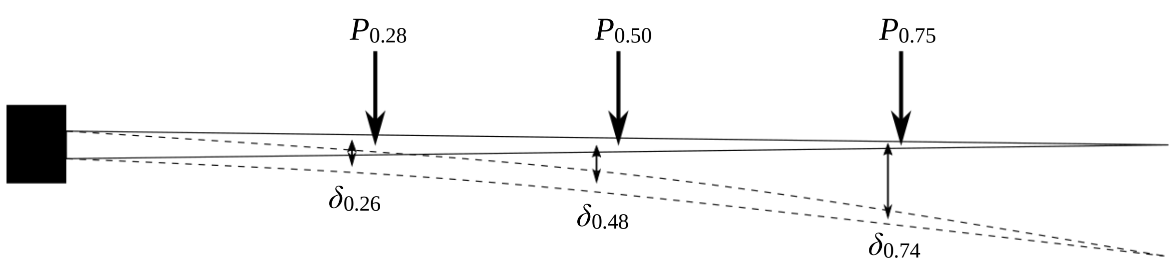

Figure 4-3: Static ground testing setup for SUMR-D blades with loads (*P*) applied at 28%, 50%, and 75% span, and deflections (δ) measured at 26%, 48%, and 74% span

The static ground testing was recreated in ANSYS Mechanical ANSYS Parametric Design Language (APDL)[29] for both the SUMR-13 turbine with scaled loadings and the current SUMR-D prefabricated model. The non-dimensional values for distributed mass (Equation (4.11)) and stiffness (Equation (4.14)) for the blades from FAST input files are compared for the manufactured SUMR-D and SUMR-13 blades to determine how well these aspects scaled. The non-dimensional flapwise deflections of Equation (4.15a) are used to compare the full- and sub-scale model properties under applied loads to determine the overall fidelity of predicting deflections due to large loading.

4.2.6 *Computational Operational Dynamics*

Prior to physical operational testing of the SUMR-D turbine, the system was computationally compared to the SUMR-13 turbine using FAST [30] simulation software. Both systems use a constant 12.5-degree coning angle and a fixed base tower. FAST can be used to compare the non-dimensional rotational rate, tip-speed ratio, and coefficients of power and torque in steady conditions and the non-dimensional deflections in both steady and turbulent wind conditions. The coefficients of thrust and power are defined in Equations (4.16) and (4.17) with the torque and power outputs from FAST simulations.

$$c_{\mathrm{t}} = \frac{Thrust}{\frac{1}{2}\rho_{\mathrm{wind}}\pi U^2 S^2} \tag{4.16}$$

$$c_{\mathrm{p}} = \frac{Power}{\frac{1}{2}\rho_{\mathrm{wind}}\pi U^3 S^2} \tag{4.17}$$

The non-dimensional rotational rate and respective mode shapes are evaluated using the output rpm from FAST and BMODES. The turbulent input files were created using TurbSim[31] software. These results were used to determine set points in order to best preserve the scaling performance evaluated for gravo-aeroelastic scaling fidelity through measurement of the following non-dimensional characteristics reported in order of importance: flapping tip deflections through the entirety of the operating regime to retain aeroelastic effects in operation; tip-speed ratio to retain flow angles over the blade; rated non-dimensional operating rotational rate to ensure consistencies between input (RPM) and output (blade) frequencies.

4.3 Results and Discussion

4.3.1 *Fabricated SUMR-D*

To develop the SUMR-D blade, a 0.2 scaling factor is applied to the SUMR-13 rotor's 104-meter blade. The first column of Table 4-3 summarizes the various parameters of the full-scale rotor. The second column applies the scaling laws listed in Table 4-1 with this 0.2 scaling factor to achieve parameters for an ideally scaled rotor if one ignores the influence of the changing Reynolds and Mach numbers between the full-scale and the ideally scaled rotors. For each system, the Mach number is below where compressibility comes into effect and it can be reasonably ignored; however, the difference in Reynolds number cannot be ignored as it changes the aerodynamic performance, which can result, for example, in a 6% reduction in the aerodynamic thrust coefficient keeping the same pitch setting for both SUMR-D and SUMR-13. This reduction in thrust can significantly affect the load and moment ratios. Similar issues arise with respect to the fabrication safety constraints (higher inboard mass) and platform used (differences in blade mass, hub radius, shaft tilt, and so on) as will be discussed.

Table 4-3: Various parameters for the full-scale SUMR-13 model, the ideally scaled SUMR-D, the fabricated (as-built) SUMR-D mounted on the CART2, and the conventional CART2 blades and tower

	SUMR-13	Ideal Scaled SUMR-D	SUMR-D Fabricated	CART2
Design Innovation	Extreme Scale	Extreme Scale	Extreme Scale	Conventional
Length Scaling Factor (η)	1	0.2	0.2	-
Blade Length (S)	104.36 m	20.87 m	20.87 m	19.96 m
Hub Radius (r_{hub})	2.5 m	0.5 m	1.38 m	1.38 m
Adapter Length (r_{adapter})	0 m	0 m	0.5 m	0 m
Coning Angle (β)	Variable	12.5 degrees	12.5 degrees	0 degrees
Shaft Tilt (τ)	0 degrees	0 degrees	3.77 degrees	3.77 degrees
Tip-Speed Ratio (λ)	9.5	9.5	9.5	7.32
Rated Wind Speed (U_{rated})	11.3 m/s	5.05 m/s	5.75 m/s	12.7 m/s
Rated Rotor Speed (Ω_{rated})	9.82 rpm	21.96 rpm	21.47 rpm	41.7 rpm
Rated Froude Moment (Fr_{moment})	10.39	10.39	8.61	(-)
Blade Mass (m)	54787 kg	350.6 kg	985.6 kg	2126 kg
Non-D Rotational Rate ($\bar{\Omega}$) at Ω_{rated}	0.23	0.23	0.28	0.32
Ref. Reynolds Number (Re)/10^6	16.3	1.16	1.27	4.55
Ref. Mach Number (Ma)	0.227	0.101	0.111	0.196

The rotor summarized in Table 4-3, column 2 represents the ideal GAS scaled system when ignoring Reynolds number effects; however, as previously noted, environmental and manufacturing constraints also required that the fabricated SUMR-D parameters differ from the ideal. Shulong *et al*. (2020)[19] provides a detailed summary of the blade structural design. The blade mass of the as-built model (summarized in Table 4-3, column 3) is three times the ideal blade mass with the extra mass concentrated near the blade root; however, the blade mass remains less than half the weight of the conventional blades typically mounted on the CART2 turbine [20,21] due to scaling and the lower power rating as summarized in Table 4-3, column 4. However, the fabricated SUMR-D blade is less than half the mass of the original CART-2 blade.

The environmental differences cause the mass and stiffness distributions of the manufactured blade to differ from ideal through the length of the blade. As will be shown, this resulted in some degradation of the non-dimensional stiffness and frequency scaling of Equations (4.13) and (4.14),

In terms of frequency, it can be seen that the fabricated SUMR-D flapwise frequency is about 8% to 18% (depending on the rotation rate) of the ideally-scaled SUMR-D flapwise frequency, and is substantially lower than that of the CART-2 original blade (indicating increased flexibility). Notably, the flapwise stiffness of a rotor blade relative to an applied force is proportional to $S\rho_{\text{wind}}U_{\text{rated}}^2/(m\omega_{\text{flap}}^2)$. As such, the overall fabricated SUMR-D blade is about half the stiffness of the original CART-2 blade. However, it is even more flexible at the tip, since most of the mass of the SUMR-D blade is located near the root. This is because scaling for the non-dimensional tip-speed ratios and tip deflections in Equations (4.2) and (4.15a) were held at a premium.

Table 4-4 presents the environmental conditions expected for the SUMR-13 turbine, the ideal SUMR-D turbine, the fabricated SUMR-D turbine, and the theoretical conditions of the fabricated SUMR-D environment at full-scale. The 50-year gusts and turbulence intensities of the SUMR-13 and fabricated SUMR-D turbines are based upon values defined under IEC Class IIB wind speeds and IEC Class IA wind speeds respectively. The ideal SUMR-D values and fabricated SUMR-D at full-scale values are based upon scaling of Table 4-1 with the fabricated SUMR-D values being scaled up to full-scale based upon the fabricated SUMR-D environment.

Table 4-4: Comparison of the conditions of the SUMR-13 environment, the ideal environment for the SUMR-D turbine, the environment of the fabricated SUMR-D turbine, and the fabricated SUMR-D environment scaled back up to full-scale (with schematics shown below with relative turbine size)

	SUMR-13 Full-Scale	Downscaled SUMR-13 (Ideal SUMR-D)	As-Built SUMR-D for NREL FC Testing	Up-scaled Version of As-Built SUMR-D
Length Scaling Factor (η)	1	0.2	0.2	1
Air Density (ρ_{air})	1.2 kg/m^3	1.2 kg/m^3	0.96 kg/m^3	0.96 kg/m^3
$U_{50\text{-}year,\ gust}$	70 m/s	31.3 m/s	70 m/s	156.5 m/s
Turbulence Intensity	0.14	0.14	0.18	0.18

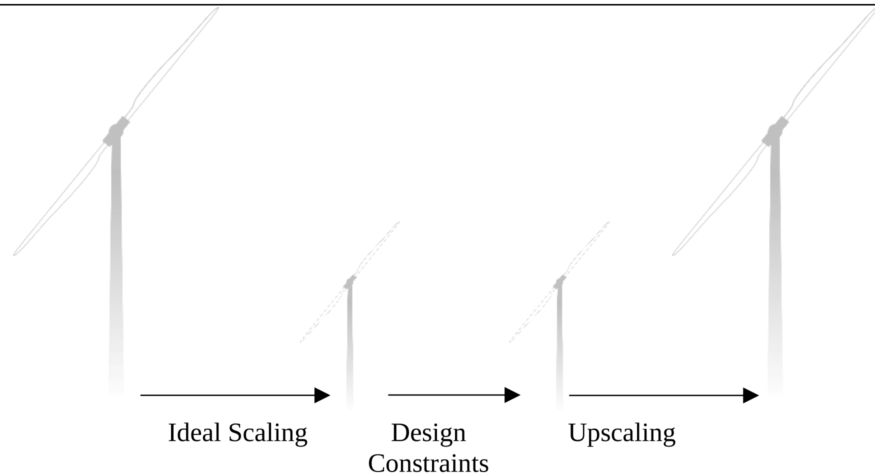

The NREL FC, where the manufactured SUMR-D blades are being tested, is much harsher than the ideal scaled environment with a 39 m/s (87 mph) increase in the 50-year-gust and a 4% increase in turbulence intensity. Additionally, one can appreciate the conditions a back-to-full-scale SUMR-D rotor would need to withstand. As such, while it is ideal to match the non-dimensional distributed blade mass density and stiffness values for scaling, it is infeasible due to the higher and more turbulent wind conditions at the NREL FC. Once these environmental constraints are combined with those coming from manufacturing, it becomes clear why a heavier than the ideal GAS blade was achieved; however, the SUMR-D blades were fabricated maintaining the desired natural flapwise frequencies and, as will be discussed, the control set points were set such that the deflection angles due to aerodynamics are preserved. These expedients allow for faithful capturing of the main aeroelastic scaling; however, the higher mass of the manufactured SUMR-D blade indicates that deflection angles due to gravitational forces and moments will be larger than expected. As such, the blade was not able to achieve a full *gravo*-aeroelastic scaling. This is reflected in the lower Froude number for the SUMR-D.

Figure 4-4 presents the structural layout differences between the SUMR-13 and SUMR-D blades at 25% span. The SUMR-13 turbine contains four shear webs which range from 13.53 degrees twist at the root to 0 degrees twist at the tip [15]. The fabricated SUMR-D blade contains two shear webs that do not twist throughout the length of the blade [18]. A root adapter is included for SUMR-D to both allow for a transition to the oval root of the CART2 hub, as well as to create the sought 12.5-degree pre-cone angle since the CART2 had no such coning [17].

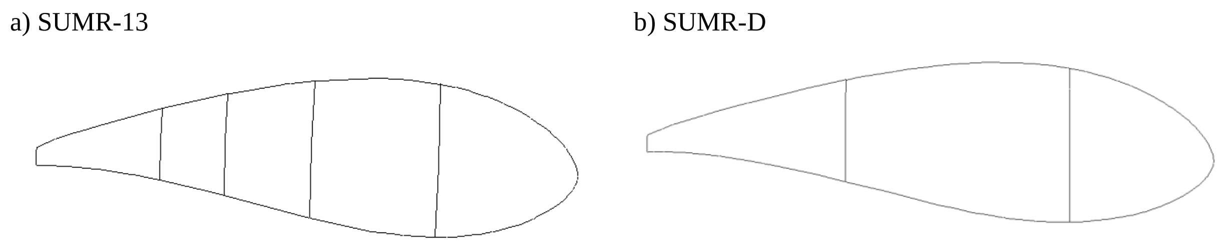

Figure 4-4: Internal structure comparison at 25% span of a) the SUMR-13 blade and b) the SUMR-D blade

The non-dimensional blade mass density and distributed flapwise stiffness values are plotted in Figure 4-5. The inboard mass density and stiffness is higher than the ideal values for what has been discussed; however, the difference is also due to the additional mass required for root hardware, which was not included in the ideal model. Notably, the aeroelastic flapwise operational blade tip deflections are primarily controlled by the outboard flapwise stiffness. Thus, as will be shown, the SUMR-D blade on the CART2 platform can still be used to achieve reasonable aeroelastic flapwise scaling of the extreme-scale SUMR-13.

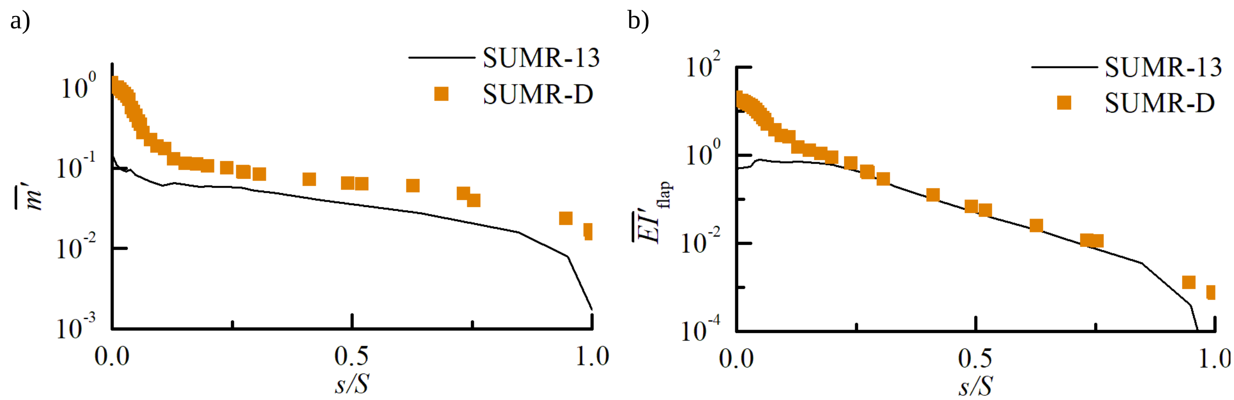

Figure 4-5: Non-dimensional sectional spanwise (*s/S*) blade properties shown on a log-scale as a) the blade mass density ($\overline{m'}$) and b) the flapwise stiffness ($\overline{EI'}$)

4.3.2 Static Pull Test

Before mounting the blades on the CART2 turbine, the blades were structurally tested on a ground stand to extract actual deflections under load and its frequencies. An impact hammer test revealed a blade-first flapwise natural frequency of 1.13 Hz, which represents only a 6.6% difference with the ideal frequency response (as noted in Table 4-3). This indicates that fabrication was able to reasonably emulate the desired natural frequency response.

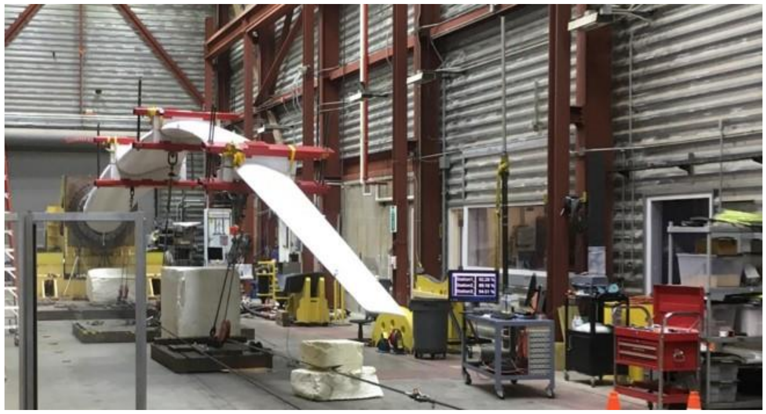

Figure 4-6: Ground-based structural testing of the manufactured SUMR-D blade at the NREL FC
Photo by Scott Hughes, NREL

In terms of stiffness, the deflections measured by the static pull test were compared to ANSYS results to check the fidelity of the digital model of the SUMR-D prefabricated blade and the performance of deflection scaling under a static load (slowly varying ramp). The blade is loaded as described by Figure 4-3 and the resulting test is depicted in Figure 4-6. Figure 4-7 depicts the non-dimensional deflection measured during the ramp-up/sustain/ramp-down load cycle as compared to the ANSYS-predicted non-dimensional deflections for the SUMR-13 and ideal SUMR-D blades. The ANSYS-predicted non-dimensional deflections (solid and dashed lines) are very similar, indicating that the linearized theoretical scaling of Table 4-2 is appropriate to use for these blades of both complex design and construction.

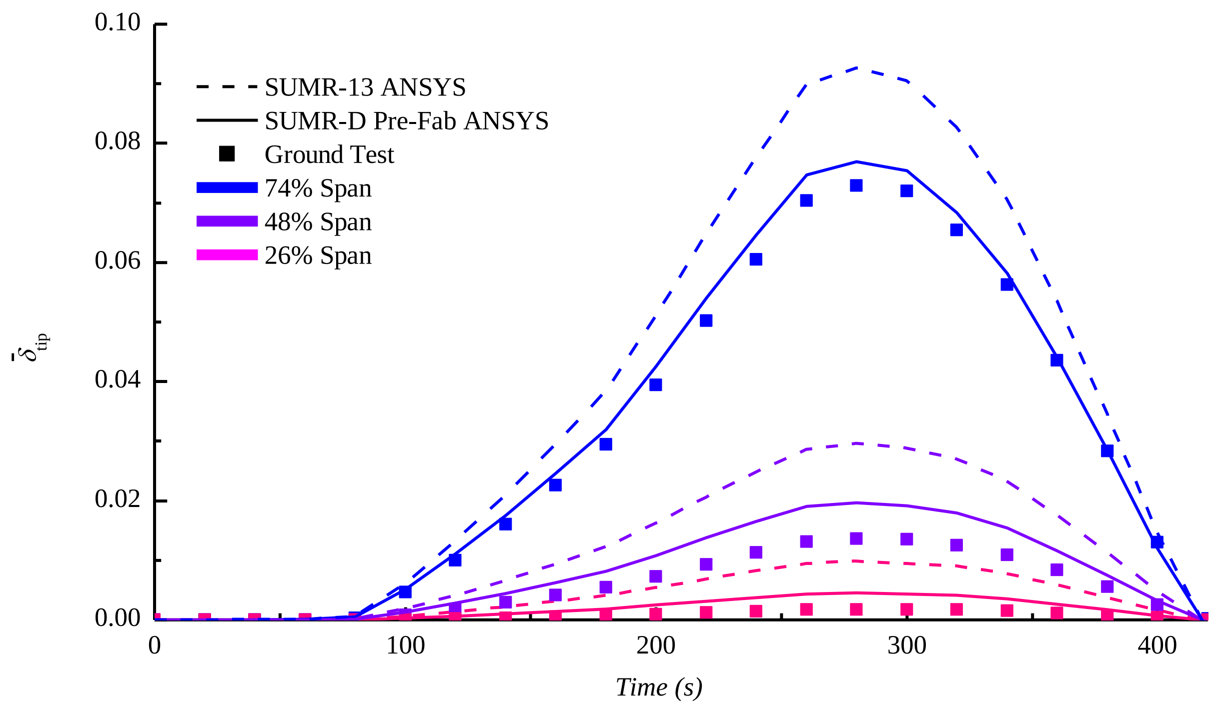

Figure 4-7: Measured (as-built SUMR-D blade, square symbols) and ANSYS predicted (solid [SUMR-D] and dashed [SUMR-13] lines) non-dimensional deflections ($\delta/_S$) at 26% (pink), 48% (purple), and 74% (blue) span.

4.3.3 *Numerically Predicted Operational Dynamics*

For operational conditions where aerodynamic differences associated with Reynolds number effects must also be considered, various set points of the ideal SUMR-D rotor can be altered, matching the full-scale non-dimensional deflections and dynamics of Equations (4.2), (4.13), and (4.15a). FAST [30] simulations were completed to determine these new control conditions. The FAST model accounts for the actual manufactured blade stiffness and mass. Additionally, it is important to note that the SUMR-13 blade was designed for individual pitch control, and the SUMR-D baseline controller will use collective pitch control.

The pitch angle in Power Region 2 and the power coefficient were investigated as a function of non-dimensional wind speed. These are plotted for the digital SUMR-D model and the SUMR-13 model in Figure 4-8b and c, respectively. Due to low Reynolds number operations, the SUMR-D turbine would render a lower C_p at a given tip-speed ratio and blade pitch. To compensate for this underperformance, the fine pitch of the blade was decreased to the lower limit implied by the turbine (-5-degrees). This is achievable because the blades were designed with a high stall margin (i.e., a significant difference between rated angle of attack and the angle of attack at maximum lift).

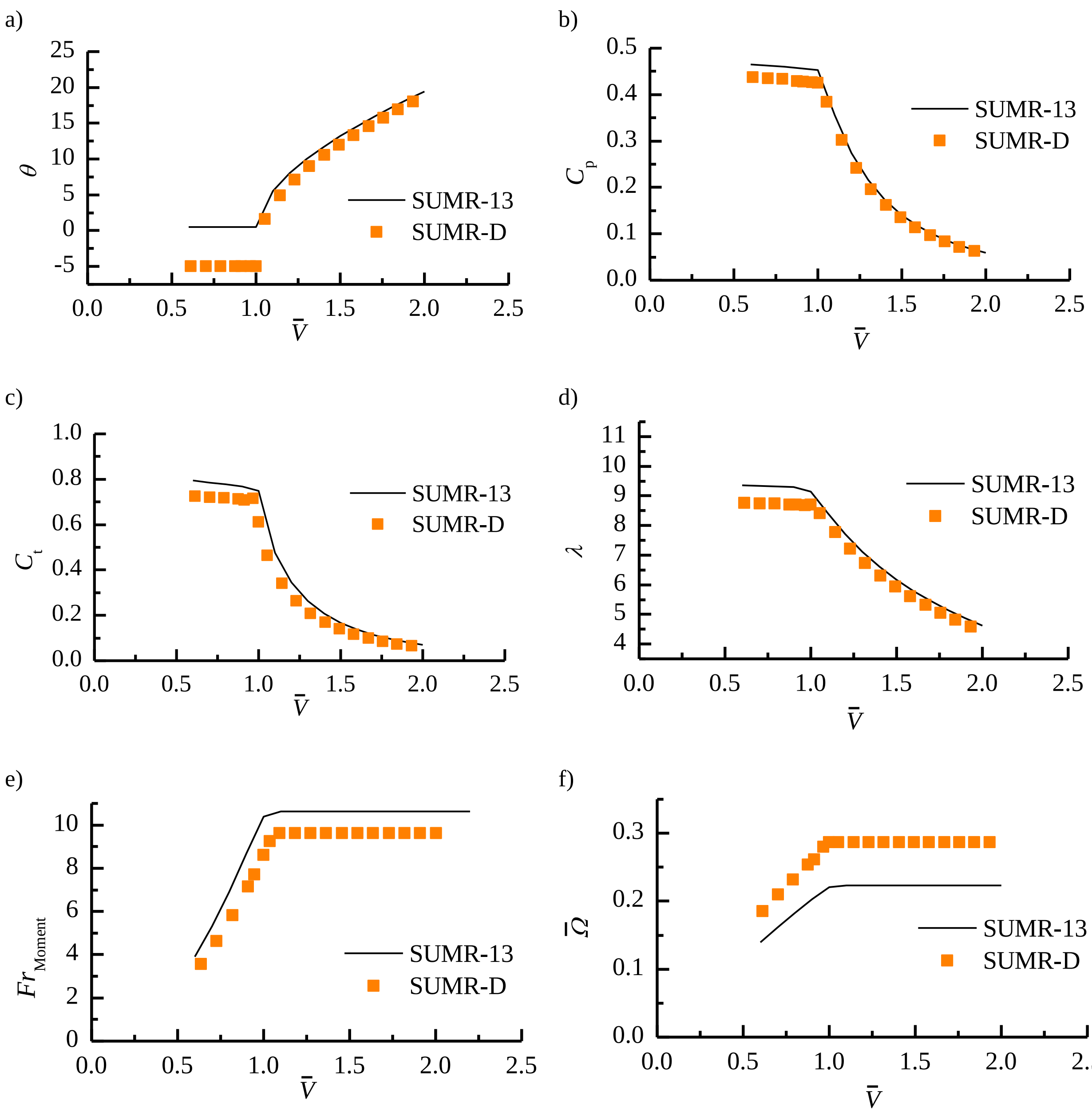

Figure 4-8: Steady-wind operational dynamic parameters calculated by using FAST: a) blade pitch angle (θ), b) power coefficient (C_p), c) aerodynamic thrust coefficient (C_t), d) tip-speed ratio (λ), and e) the rotational moment based Froude number (Fr_{moment}), and f) non-dimensional rotation rate ($\overline{\Omega}$).

At above rated wind speed conditions, the operational control goal is to keep the rpm constant while also holding the generator torque constant for constant power. To achieve this goal, the system adjusts the blade pitch angle to slightly lower values compared to the SUMR-13. To increase the loads on the blade, the aerodynamic torque is increased by reducing the operational pitch which subsequently increases the rotor rpm. The resulting coefficients of thrust are plotted in Figure 4-8d. While the system was able to make up for some losses due to Reynolds number mismatch, the demonstrator coefficient of thrust values still lies below the ideal values.

Due to the blades having higher than ideal mass and stiffness distributions, they exhibit a higher non-dimensional rotation rate compared to ideal as shown in Figure 4-8f. While this is non-ideal for the SUMR-Demonstrator, Figure 4-9 shows the first flapwise, edgewise, and torsional mode shapes, each exhibiting similar shapes between the full- and sub-scale rotors. The SUMR-13 non-dimensional first flapwise and edgewise rotational rates at rated conditions are 0.23 and 0.28 respectively and the SUMR-D non-dimensional first flapwise and edgewise rotational rates at rated conditions are 0.28 and 0.16 respectively.

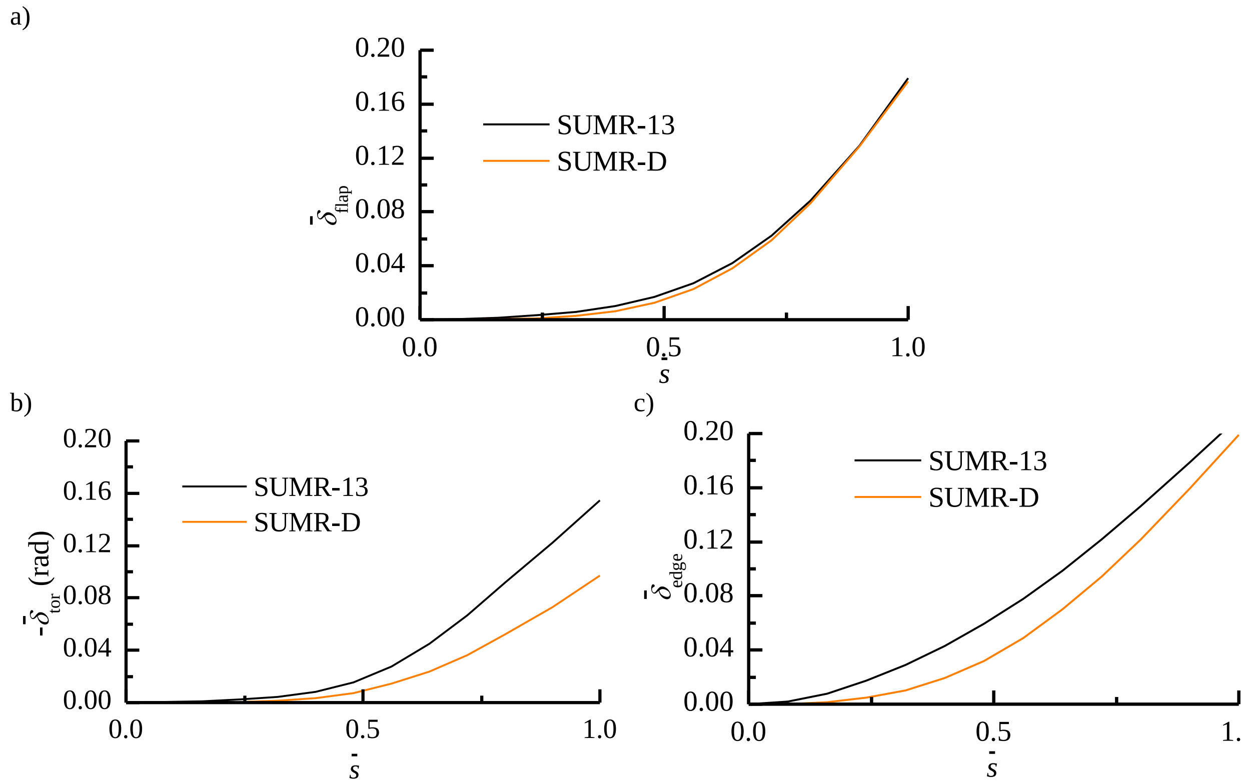

Figure 4-9: Comparison of the non-dimensional first mode shapes during steady rated RPM conditions for the a) flapwise direction, b) torsional direction, and c) edgewise direction.

To achieve the best matching of the non-dimensional flapwise frequencies (discussed above) and the non-dimensional flapwise deflections (to be discussed below) several parameters were adjusted to take into account the fabrication constraints. For example, the velocity at which rated conditions occur was shifted slightly from the idealized conditions to better match the tip-speed ratio (as shown in Figure 4-8e) and change pitch settings and other parameters were adjusted as shown in Table 4-5. These adjustments helped address changes in the aerodynamic performance of the turbine due to Reynolds number effects. Additionally, Figure 4-8f shows the rotational flapwise moment-based Froude number. The SUMR-D rotor lies below the SUMR-13 values as expected given the larger than ideal mass but there is generally good agreement.

Table 4-5: Design set points of the ideal SUMR-D compared against the set points for the as built SUMR-D once modified to increase the GAS fidelity

	Ideal SUMR-D	SUMR-D Fabricated
Below Rated Blade Pitch	0.5 degrees	-5 degrees
Rated Wind Speed (U_{rated})	5.05 m/s	5.75 m/s
Rated Rotor Speed (Ω_{rated})	21.96 rpm	21.47 rpm
Coefficient of Torque (C_{q})	1.89E-3	2.61E-3

Finally, we consider the overall fidelity of the scale model from a simulation point of view by comparing the expected blade deflections and dynamics during operation. Figure 4-10a and b represent the simulated blade flapwise tip deflections under steady winds and turbulent wind conditions, respectively. Both the mean, as well as the variations (the hatched region represents the +/-1-standard deviation), are depicted. Note that the variations in tip deflections for steady wind conditions are induced primarily by changes in gravitational loadings as the blades move azimuthally. Based on the historical wind data at the NREL FC, it is expected that 30% of the time, wind conditions will be within the above rated wind region. When referencing the predicted turbulent dynamics of Figure 4-10b, the above rated conditions of the demonstrator are projected to have similar non-dimensional tip deflections as that of the SUMR-13 model. Conversely, the rated and below-rated deflections of the SUMR-D blades are predicted to fall below the SUMR-13 predictions which is partially a result of pitch setting limitations deriving from retrofitting the CART2 as a downwind machine [17]. Due to the system primarily being tested in above-rated conditions, the trade-off between matching above-rated and below-rated conditions was deemed adequate. Based on these results, a field testing campaign is now scheduled to demonstrate the experimental fidelity of the GAS approach.

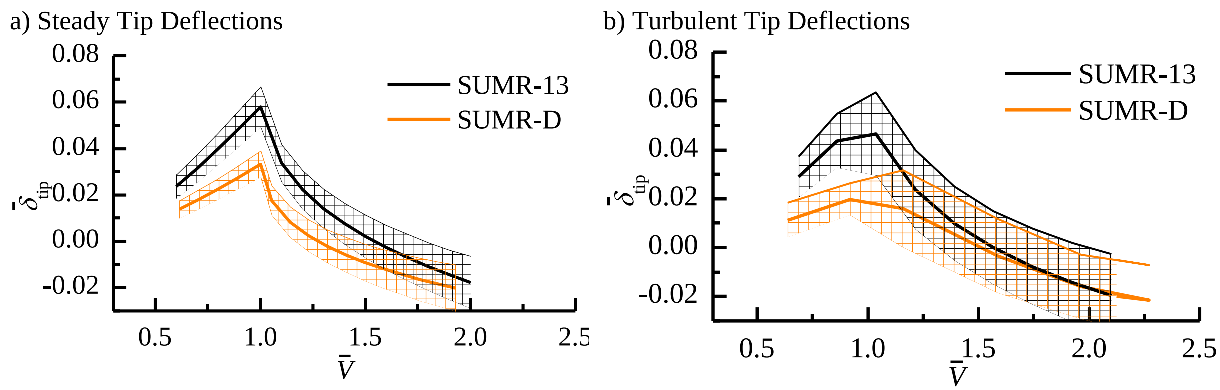

Figure 4-10: Simulated mean (solid line) and RMS (hatched) tip deflections ($^{\delta}/_{S}$) in both a) steady conditions and b) turbulent conditions for the entire range of non-dimensional wind speeds ($^{V}/_{V_{\mathrm{rated}}}$)

4.4 Conclusions and Recommendations

This study presents the scaling specifications used to gravo-aeroelastically design a 20-meter sub-scale model of a 104-meter blade, which intends to replicate the full-scale structural flapwise dynamics and deflections in field tests. The full-scale model is a two-bladed downwind turbine (SUMR-13). The scaled model (SUMR-D) was designed with a gravo-aeroelastic scaling (GAS) method, which aims to match the non-dimensional tip deflections, tip-speed ratio, and the non-dimensional rotational rate for testing at the NREL FC on the two-bladed (upwind) Controls Advanced Research Turbine (CART2), while ensuring all NREL FC safety constraints for operational and parked testing are maintained.

For such a GAS approach, a host of challenges present themselves when applied to extreme-scale downwind rotor designs. These challenges include mismatch in Reynolds numbers (and thus loss in aerodynamic performance); sub-scale manufacturing constraints; downwind retrofit of an upwind platform; and site meteorological conditions characterized, among other aspects, by high wind speeds that require significant safety measures. The GAS method and the constraints arising from these challenges present conflicting design goals, whereby idealized scaling drives the blade design to reduce mass and stiffness whereas the other aspects generally warrant an increase in blade mass and stiffness. As a result, the as-built blade deviated from the ideal GAS blade. For example, the fabricated SUMR-D is approximately three times heavier than the ideal GAS blade, despite being half the weight of the CART2 conventional blade it replaced. Despite these differences, careful attention to outboard stiffness and mass distributions, along with careful design of operational control rendered a design that scales the mean and fluctuating blade tip deflections reasonably well in above-rated conditions, the primary testing region of at the NREL FC. Some of the control set points had to be adjusted to compensate for some of the differences between ideal and as-built scaled blades. This included shifting the blade pitch and the rated values for wind speed, rotational speed, and torque, while maintaining the tip-speed ratio and the non-dimensional rotational rate.

Despite the non-dimensional rotational rate being higher than ideal, the ground testing under prescribed loads of the as-built SUMR-D blades demonstrated that the intended aeroelastic structural behavior was achieved in terms of both predicted flapwise deflections and first flapwise, edgewise, and torsional mode shapes. A field testing campaign is now scheduled to verify these results and further validate the gravo-aeroelastic scaling method. Recommended future work includes analyzing the field data to compare against the computational predicted operational dynamics to experimentally assess the fidelity of the GAS approach. A field testing campaign is currently scheduled to Additionally, this will lead to considering the GAS approach for other advanced technology extreme-scale wind turbines to reduce the cost of field assessment via sub-scale demonstrators that may provide equivalent gravo-aeroelastic behavior in terms of deflections and dynamics.

References

[1] Wiser, R., and Bolinger, M. *2017 Wind Technologies Market Report*. 2017.

[2] Kaminski, M., Loth, E., Griffith, D. T., and Qin, C. (Chris). “Ground Testing of a 1% Gravo-Aeroelastically Scaled Additively- Manufactured Wind Turbine Blade with Bio-Inspired Structural Design.” *Journal of Renewable Energy*, Vol. 148, 2020, pp. 639–650. doi:10.1016/j.renene.2019.10.152.

[3] Viselli, A. M., Goupee, A. J., and Dagher, H. J. “Model Test of a 1:8-Scale Floating Wind Turbine Offshore in the Gulf of Maine.” *Journal of Offshore Mechanics and Arctic Engineering*, 2015. doi:10.1115/1.4030381.

[4] Dagher, H. J., Viselli, A. M., Goupee, A. J., Kimball, R., and Allen, C. *The VulturnUS 1:8 Floating Wind Turbine*.

[5] Robertson, A. N., Jonkman, J. M., Goupee, A. J., Coulling, A. J., Browning, J., Masciola, M. D., and Molta, P. *Summary of Conclusions and Recommendations Drawn from the DeepCwind Scaled Floating Offshore Wind System Test Campaign*. 2013.

[6] Viselli, A. M., Goupee, A. J., Dagher, H. J., and Allen, C. “Design and Model Confirmation of the Intermediate Scale VolturnUS Floating Wind Turbine Subjected to Its Extreme Design Conditions Offshore Maine.” *Wind Energy*, Vol. 19, No. 6, 2016, pp. 1161–1177. doi:10.1002/we.

[7] Griffith, D. T., and Ashwill, T. D. *The Sandia 100-Meter All-Glass Baseline Wind Turbine Blade : SNL100-00*. 2011.

[8] Fingersh, L. J., Sinuns, D., Hand, M., Jager, D., Cotrell, J., Robinson, M., Schreck, S., and Larwood, S. “Wind Tunnel Testing of NREL’s Unsteady Aerodynamics Experiment.” 2001. doi:10.2514/6.2001-35.

[9] Berg, J., Bryant, J., LeBlanc, B., Maniaci, D., Naughton, B., Paquette, J., Resor, B., and White, J. “Scaled Wind Farm Technology Facility Overview.” *AIAA SciTech*, 2014.

[10] Resor, B. R., and Maniaci, D. C. “Definition of the National Rotor Testbed: An Aeroelastically Relevant Research-Scale Wind Turbine Rotor.” *AIAA SciTech*, 2014. doi:10.2514/6.2014-0357.

[11] Loth, E., Kaminski, M., and Qin, C. “Gravo - Aeroelastic Scaling for Extreme - Scale Wind Turbines.” *AIAA Aviation Conference*, 2017, pp. 1–11.

[12] Griffith, D. T., and Richards, P. W. *The SNL100-03 Blade : Design Studies with Flatback Airfoils for the Sandia 100-Meter Blade*. 2014.

[13] Kaminski, M., Loth, E., Qin, C., Griffith, D. T., and Scaling, G. “Gravo-Aeroelastic Scaling a 13.2 MW Wind Turbine Blade to a 1-Meter Model.” *AIAA SciTech*, 2018, pp. 1–12.

[14] Loth, E., Steele, A., Qin, C., Ichter, B., Selig, M. S., and Moriarty, P. “Downwind Pre-Aligned Rotors for Extreme-Scale Wind Turbines.” *Wind Energy*, Vol. 20, No. 7, 2017, pp. 1241–1259. doi:10.1002/we.

[15] Ananda, G. K., Bansal, S., and Selig, M. S. “Aerodynamic Design of the 13.2 MW SUMR-13i Wind Turbine Rotor.” *AIAA SciTech Forum*, 2018. doi:10.2514/6.2018-0994.

[16] Ichter, B., Steele, A., Loth, E., Moriarty, P., and Selig, M. S. “Amorphing Downwind-Aligned Rotor Concept Based on a 13-MW Wind Turbine.” *Wind Energy*, Vol. 19, No. 4, 2016, pp. 625–637. doi:10.1002/we.

[17] Bay, C. J., Damiani, R., Jay Fingersh, L., Hughes, S., Chetan, M., Yao, S., Todd Griffith, D., Ananda, G. K., Selig, M. S., Zalkind, D. S., Pao, L. Y., Martin, D., Johnson, K. E., Kaminski, M., and Loth, E. “Design and Testing of a Scaled Demonstrator Turbine at the National Wind Technology Center.” *AIAA Scitech Forum*, 2019.

[18] Yao, S., Griffith, D. T., Chetan, M., Bay, C. J., Damiani, R., Kaminski, M., and Loth, E. “Structural Design of a 1/5 Th Scale Gravo-Aeroelastically Scaled Wind Turbine Demonstrator Blade for Field Testing.” *AIAA SciTech*, 2019, pp. 1–9. doi:10.2514/6.2019-1067.

[19] Yao, S., Griffith, D. T., Chetan, M., Bay, C. J., Damiani, R., Kaminski, M., and Loth, E. “A Gravo-Aeroelastically Scaled Wind Turbine Rotor at Field-Prototype Scale with Strict Structural Requirements.” *Renewable Energy*, 2020. doi:10.1016/j.renene.2020.03.157.

[20] Bossanyi, E. A., Wright, A. D., and Fleming, P. A. *Controller Field Tests on the NREL CART2 Turbine*. 2010.

[21] K.A. Stol. “Geometry and Structural Properties for the Controls Advanced Research Turbine (CART) from Model Tuning.” *Nrel/Sr*, No. September, 2004, pp. 500–32087.

[22] Noyes, C., Qin, C., and Loth, E. “Pre-Aligned Downwind Rotor for a 13.2 MW Wind Turbine.” *Renewable Energy*, Vol. 116, 2018, pp. 749–754. doi:10.1016/j.renene.2017.10.019.

[23] Loth, E., Selig, M. S., and Moriarty, P. “Morphing Segmented Wind Turbine Concept.” *AIAA Applied Aerodynamics Conference*, No. July, 2010, pp. 1–6. doi:10.2514/6.2010-4400.

[24] Loth, E., Steele, A., Ichter, B., Selig, M. S., and Moriarty, P. Segmented Ultralight Pre - Aligned Rotor for Extreme - Scale Wind Turbines. 2012.

[25] Noyes, C., Qin, C., and Loth, E. Ultralight, Morphing Rotor for Extreme-Scale Wind Turbines. 2017.

[26] Virginia Offshore 90-Meter Wind Map and Wind Resource Potential. https://windexchange.energy.gov/maps-

data/237. Accessed Dec. 9, 2019.

[27] Wanke, G., Bergami, L., Larsen, T. J., and Hansen, M. H. “Changes in Design Driving Load Cases: Operating an Upwind Turbine with a Downwind Rotor Configuration.” *Wind Energy*, Vol. 22, No. 11, 2019, pp. 1500–1511. doi:10.1002/we.2384.

[28] International Eletrotechnical Commision. “IEC 61400-1 Wind Turbines - Part 1: Design Requirements.” *Wind turbines – Part 1: Design requirements*, Vol. 2005, 2005, pp. 1–92. doi:10.1055/s-2007-985912.

[29] Ansys inc. “Mechanical APDL Modeling and Meshing Guide.” Vol. 3304, No. November, 2010, pp. 724–746. doi:www.ansys.com.

[30] Jonkman, J. M., and Buhl, M. L. *FAST User’s Guide*. 2005.

[31] Jonkman, J. M., and Kilcher, L. *TurbSim User’s Guide: Version 1.06.00*. 2012.

Appendix A

(X_1,Y_1,Z_1):

Frame (1) is a fixed frame connected to the nacelle. The X_1 axis points downwind along the nacelle centerline, the Z_1 axis is in the vertical direction and the Y_1 axis is perpendicular to the X_1 and Z_1 axis to form a right-handed coordinate system. The gravitational force is in the negative Z_1 direction and the thrust force is in the X_1 direction.

(X_2,Y_2,Z_2):

Frame (2) is a rotating coordinate system connected to the hub. This coordinate system is transformed from Frame (1) by rotating about the Y_1 axis in the positive direction by τ to take into account the shaft tilt with the following transformation matrix:

$$\begin{bmatrix} cos\,(\tau) & 0 & sin\,(\tau) \\ 0 & 1 & 0 \\ -sin\,(\tau) & 0 & cos\,(\tau) \end{bmatrix} \tag{A1}$$

The coordinate frame then rotates about the intermediate x-axis in the positive direction by ψ to take into account the azimuthal position of the rotor with the following transformation matrix:

$$\begin{bmatrix} 1 & 0 & 0 \\ 0 & cos\,(\psi) & -sin\,(\psi) \\ 0 & sin\,(\psi) & cos\,(\psi) \end{bmatrix} \tag{A2}$$

A1 and A2 multiplied together form the transformation matrix starting in Frame (1) and ending in Frame (2).

$$\begin{bmatrix} x_2 \\ y_2 \\ z_2 \end{bmatrix} = \begin{bmatrix} cos\,(\tau) & 0 & sin\,(\tau) \\ sin\,(\psi) sin\,(\tau) & cos\,(\psi) & -sin\,(\psi) cos\,(\tau) \\ -sin\,(\tau) cos\,(\psi) & sin\,(\psi) & cos\,(\psi) cos\,(\tau) \end{bmatrix} \begin{bmatrix} x_1 \\ y_1 \\ z_1 \end{bmatrix} \tag{A3}$$

The X_2 axis points downwind along the shaft axis, the Z_2 axis points radially in the direction of blade length and perpendicular to the x-axis, and the Y_2 axis is perpendicular to the X_2 and Z_2 axis to form a right-handed coordinate system. The blade centrifugal force is in the Z_2 direction.

(X_3,Y_3,Z_3):

Frame (3) is a rotating coordinate system connected to the blade. This coordinate system is transformed from Frame (2) by rotating about the Y_2 axis in the positive direction by β to take into account the coning angle with the following transformation matrix:

$$\begin{bmatrix} cos\,(\beta) & 0 & sin\,(\beta) \\ 0 & 1 & 0 \\ -sin\,(\beta) & 0 & cos\,(\beta) \end{bmatrix} \tag{A4}$$

The above matrix is multiplied by Frame (2) to transform to Frame (3) through as follows:

$$\begin{bmatrix} x_3 \\ y_3 \\ z_3 \end{bmatrix} = \begin{bmatrix} cos\,(\beta) & 0 & sin\,(\beta) \\ 0 & 1 & 0 \\ -sin\,(\beta) & 0 & cos\,(\beta) \end{bmatrix} \begin{bmatrix} x_2 \\ y_2 \\ z_2 \end{bmatrix} \tag{A5}$$

Substituting A3 in A5, the following transforms between Frame (1) and Frame (3).

$$\begin{bmatrix} x_3 \\ y_3 \\ z_3 \end{bmatrix} = \\ = \begin{bmatrix} cos(\tau)\,cos(\beta) - sin\,(\tau)cos\,(\psi)sin\,(\beta) & sin\,(\beta)sin\,(\psi) & cos(\beta)\,sin(\tau) + sin\,(\beta)cos\,(\psi)cos\,(\tau) \\ sin\,(\psi)sin\,(\tau) & cos\,(\psi) & -sin\,(\psi)cos\,(\tau) \\ cos\,(\tau)sin\,(\beta) & sin\,(\psi)cos\,(\beta) & -sin(\tau)\,sin(\beta) + cos\,(\beta)cos\,(\psi)cos\,(\tau) \end{bmatrix} \begin{bmatrix} x_1 \\ y_1 \\ z_1 \end{bmatrix} \qquad \text{A6}$$

The X_3 axis is in the blade root flap direction, the Z_3 axis is radially attached to the blade and is the blade axial direction, and the Y_3 axis is perpendicular to the X_2 and Z_2 axis to form a right-handed coordinate system and is also the negative edgewise direction of the blade.

5. Parked Testing of a 20% Scaled Demonstrator Representing the Aeroelasticity of a 13-MW Downwind Turbine

Abstract

Aeroelastic parked testing of a unique downwind 2-bladed rotor is designed and built to replicate the response of an extreme-scale turbine in high winds. Such parked conditions (at high wind speeds above cut-out) represent an important design load case for rotor structural design. The turbine in this study is a 20% sub-scale model of the 13-MW Segmented Ultralight Morphing Rotor (SUMR-13) and was tested on the Controls Advanced Research Turbine at the National Renewable Energy Lab's Flatiron Campus (NREL FC). The blades for the demonstrator (SUMR-D) were designed using aeroelastic scaling to generally replicate the non-dimensional structural elastic deflections induced by parked aerodynamics of a highly-flexible lightweight, 13-MW rotor designed for Class IIB wind speeds. The aeroelastic scaling was adjusted to accommodate the test site which has a 50-year gust of about 70 m/s which is significantly higher than the idealized 50-year gust of 26.6 m/s. Thus, the SUMR-D was designed and fabricated to handle much higher loads than that of the theoretical aeroelastically scaled blade. The horizontal parked testing included both horizontal pitch-to-run and pitch-to-feather configurations with detailed measurements of inflow wind conditions along with root bending moments and tip deflections. The flapwise bending moments were based on strain gauges located in the root section while tip deflections are measured by way of a video camera on the hub of the turbine pointed towards the tip of the blade. These results are compared against computational predictions using the SUMR-D structural digital twin to analyze the fidelity of FAST predictions for this novel configuration. In general, FAST provided reasonable predictions of the bending moments and deflections of the experimental data. However, it was found that the predicted coefficient of drag in stall conditions for the SUMR-D rotor was overestimated by the FAST aerodynamic model. FAST was also used to analyze and assess the efficacy of the scaling method used for the sub-scale blade design. The results indicated that SUMR-D has similar non-dimensional moments and deflections in terms of both mean and standard deviations demonstrating the success of the first such aeroelastically-scaled turbine test and providing opportunities for high-fidelity sub-scale testing for novel extreme-scale turbine designs.

Nomenclature

EI	=	blade stiffness
h	=	height
g	=	gravitational constant
L	=	RMS error
l	=	distance between tabs
m	=	blade mass
M	=	moment
P	=	applied load
p	=	pixel
r	=	distance
s	=	spanwise location
S	=	total blade length
t	=	time
U	=	wind speed
β	=	cone angle
δ	=	deflection
η	=	scaling factor
ρ	=	density
ϕ	=	blade pitch
φ	=	local airfoil twist angle
τ	=	shaft tilt

Subscripts

$()_0$	=	reference value
$()_{50-\mathrm{year}}$	=	50-year gust
$()_{\mathrm{cut-out}}$	=	cut-out value
$()_{\mathrm{edge}}$	=	edgewise value
$()_{\mathrm{f}}$	=	full-scale value
$()_{\mathrm{flap}}$	=	flapwise value
$()_{\mathrm{hub}}$	=	hub value
$()_{\mathrm{horiz}}$	=	horizontal value
$()_{\mathrm{met}}$	=	meteorological tower value
$()_{\mathrm{pixel}}$	=	pixel to distance conversion
$()_{\mathrm{rated}}$	=	rated value
$()_{\mathrm{s}}$	=	sub-scale value
$()_{\mathrm{tip}}$	=	tip tab
$()_{\mathrm{tot}}$	=	distance value
$()_{\mathrm{tip}}$	=	tip value
$()_{\mathrm{wind}}$	=	wind value
$()_{xx}$	=	spanwise location
$()_{x,y,z}$	=	coordinate frame
$()'$	=	spanwise distributed value
$\overline{()}$	=	non-dimensional value

5.1 Introduction

5.1.1 Motivation for Parked Testing of Rotors Designed for Extreme-Scale Turbines

Wind turbine sizes are increasingly growing in height as well as blade length to increase the capture area and increase the power produced. This increase in blade length is coupled with an increase in flexibility not seen in conventionally-sized wind turbines [1]. This blade flexibility can limit upwind turbine sizes due to the increased potential of blade-tower strike due to a combination of high thrust loads and blade dynamics caused by turbulence. One way to address this is to employ downwind turbines which lessen the probability of tower strike since thrust bends the blade away from the tower. In addition, this downwind turbine uses load-aligning rotors to reduce the flapwise loads and corresponding structural requirements, creating lighter blades which can reduce the Levelized Cost of Energy [2]. As such, downwind extreme-scale turbines (rated power in excess of 10-MW) need to consider extreme-wind speeds that may occur (e.g. hurricane conditions) [3]. Such loads occur when the turbine is parked and experiencing wind speeds significantly greater than the rated wind speed; therefore, Design Load Cases (DLCs) for parked conditions are of greater importance as design drivers for downwind extreme-scale turbines than they are for conventional-scale upwind turbines [4]. In some cases, parked conditions for an extreme-scale downwind turbine are the most important design drivers [5]. Typically, modern turbine designs for parked conditions are based on simulations to ensure the turbines ability to withstand extreme situations [6,7]. However, the accuracy of these simulations for new generation of downwind extreme-scale turbines (which have highly flexible, coned, and complex geometry rotors) is not known. Therefore, experimental parked testing can be highly beneficial for understanding the gravitational and aerodynamic loads on the turbine and their interactions with blade dynamics [8]. Since the cost of testing a full-scale 13-MW turbine (or other extreme-scale system) is extremely high, there is a strong motivation for developing sub-scale experimental demonstrators that capture the same non-dimensional behavior as the full-scale but at a small fraction of the testing cost [9–11].

5.1.2 Previous Scaled Testing of Wind Turbines

There have been previous sub-scale testing of wind turbines that have focused on other aspects. For example, floating sub-scale turbines have been tested experimentally in parked situations where scaling was used to replicate the influence of wave dynamics on the turbine and to evaluate computational tools used for full-scale off-shore turbine structures in unsteady sea-state conditions [12,13]. In particular, a 1/50th scale model was tested in parked conditions [12,14] and was a scaled down version of the NREL 5-MW 126-meter reference turbine [15]. This testing included hydrodynamic comparison of three distinct floating wind turbine concepts [12] in order to measure the entire wind turbine structural surge and pitch responses due to wave motion. While this test achieved its objectives to understand wind-wave-turbine interactions, there was no examination of the blade aeroelastic interactions (instead the scaled rotor blades were designed to be rigid). Similarly, the VulturnUS turbine was tested offshore on the coast of Maine using a 12.5% scaling of a 6-MW, 152-meter diameter turbine. The sub-scale turbine was designed based on Froude scaling to match the ratio of aerodynamic and wave loads during operation [7,12,16]. The hydrodynamic scale model was tested in a survival load case with scaled conditions consistent with 500-year significant wave heights and mean associated wind speeds and currents [12,13]. Again, the primary objective was to measure the wind-wave interactions on the turbine response and the blade aeroelastic aspects were not considered.

Another example of sub-scale testing was the National Renewable Energy Lab's Unsteady Aerodynamics Experiment (UAE) campaigns [17]. These tests were helpful to assess unsteady computational capabilities for stiff blades in stall conditions. Parked conditions were also considered, and the aerodynamic blade loads were studied [4]. The UAE employed rigid blades so the aeroelastic behavior is very different than what one would expect for an extreme-scale turbine where the blades tend to be quite flexible [18]. To date, there have been no sub-scale parked testing that has sought to replicate the aeroelastic behavior of extreme-scale turbines (neither for upwind nor downwind rotor configurations). As a result, there has been no assessment of current computational capabilities to predict blade deflections and loads in high gust conditions for a flexible rotor.

To develop a methodology for designing sub-scale rotors, a gravo-aeroelastic scaling (GAS) method was developed for operational conditions [19]. This type of scaling considers geometric aspects (including aerodynamic shapes and angles of attack), dynamic aspects (such as blade frequencies relative to rotor RPM and non-dimensional tip-speed ratio), as well as loads (gravitational, centrifugal, and aerodynamic forces and moments) to ensure proper load angles, dynamics, and aeroelastic deflections of the blades are considered in a non-dimensional frame work that replicates full-scale conditions. The GAS concept has been theoretically proposed for operational conditions, for which it seeks to match the non-dimensional turbine tip-speed ratio, the ratio of rotor rotational speed and blade first flapping frequency, operational tip deflections (normalized by blade length), and blade moments (normalized by a combination of air density, rated wind speeds, and blade lengths) [19].

The theoretical operational scaling was recently used to scale the 100-meter, 13.2 MW, upwind SNL 100-03 blade [20] down to a 1% scale blade model and the scaling fidelity was investigated with ground testing [19]. The scaled blade showed that additive manufacturing techniques can provide experimental sub-scale models that can statically deflect and dynamically fluctuate under pull and pluck ground tests in a non-dimensional manner (using scaled loads similar to that of a full-scale blade). The additive manufacturing of a sub-scale model also allowed for lower cost and rapid fabrication as compared to full-scale manufacturing and testing, and further provided the opportunity to experimentally investigate several novel designs with appropriate structural responses. However, this blade was not field tested since the 1/100th scale yields very large differences in Reynolds number which would provide significant changes in aerodynamics.

More recently, GAS was used to design a 20% scaled blade to mimic the highly flexible 104-meter blade of the Segmented Ultralight Morphing Rotor (SUMR-13), a 13.2 MW downwind turbine blade with high flexibility and coning intended for offshore deployment. The SUMR-13 extreme-scale design indicates significant potential savings in the Levelized Cost of Energy due to its lightweight, load-aligned design [21–24]. The 20% scale version of this rotor is termed the SUMR-Demonstrator (SUMR-D). The scaled rotor blades were fabricated and installed at the National Renewable Energy Laboratory's Flatirons Campus (NREL FC) on the Controls Advanced Research Turbine (CART-2) testing tower and nacelle [9,10]. The SUMR-D represents the largest downwind highly flexible research wind turbine demonstrator designed and built in the US in the last decade, and this study presents the first installed test results associated with this highly novel rotor design.

5.1.3 Study Objectives

The primary objective of the present study is to experimentally investigate parked conditions of a 20% scale model of an extreme-scale highly flexible rotor. To accomplish this, the SUMR-Demonstrator (SUMR-D) was tested in horizontal parked conditions in both pitch-to-run and pitch-to-feather configurations for a large range of wind speeds at significant turbulence levels. The data collected focused on the unsteady flapwise loadings in the form of flapwise bending moments and aeroelastic blade deflections. The results are also compared against the computational predictions which use the structural digital twin of the SUMR-D turbine to investigate the capability of computational simulations to predict loading for this novel, flexible, and downwind rotor for which the aeroelastic behavior is highly non-linear. In addition, the results are compared to the predicted full-scale SUMR-13 turbine response in order to assess the efficacy of the gravo-aeroelastic scaling method.

To the authors' knowledge, this is the first study that experimentally and computationally investigate parked conditions using a gravo-aeroelastically scaled rotor. Additionally, this is the first parked test of a flexible downwind, 2-bladed rotor using extreme-scale turbine design technology. It is also the first study to combine experimental and computational results to evaluate the efficacy of gravo-aeroelastic scaling for parked conditions and the first to evaluate computational predictive capabilities of blade deflections and loads in high gust conditions for a flexible rotor.

In the following, Section 5.2 presents the methods for the experimental setup, data collection, scaling approach, and computational methods. Section 5.3 provides the experimental data, the comparison to the FAST predictions with the digital twin of the SUMR-D blade, and comparison to the FAST predictions of the SUMR-13 blade to predict full-scale behavior. Finally, Section 5.4 provides the conclusions and recommendations for further studies.

5.2 Methods: Experimental

5.2.1 Gravo-Aeroelastic Scaling

For radically new designs, such as the Segmented Ultralight Morphing Rotor (SUMR) concept, experimental testing is critical for a proof of concept as the expected fidelity of present computational codes for turbine performance is largely unknown for such novel configurations which can exhibit highly non-linear aeroelastic behavior [3]. Since the full-scale design (SUMR-13) is a 13.2 MW system, full-scale testing is highly prohibitive from a cost point of view. Therefore, experimental testing of a scaled version (in this case 20% scale) is highly appropriate if it can suitably replicate the aeroelastic behavior, especially since this novel design includes flexible blades in a downwind coned configuration. In particular, experimental testing would ideally replicate the non-dimensional blade moments, deflections, and dynamics for the given aero-structural design. Therefore, a sub-scaled demonstrator (SUMR-D) was designed and fabricated to replicate as closely as possible the non-dimensional geometric, dynamic, and load-based aspects within the constraints of the well-characterized, highly-instrumented field test site.

For the parked testing aspects, the geometric scaling was based on the geometric ratio (η) of the blade length. For the SUMR-D, η is based on 20% of the SUMR-13 design. This scaling is applied to all the critical aerodynamic dimensions. For example, the ratio of the scaled blade length (S_s) to the full-scale blade length (S_f) is set equal to η.

Using this approach, the local spanwise positions along the blade length (s ,where s = 0 is the blade root) for both the sub-scale and full-scale rotors can be normalized as:

$$\bar{s} = {}^{s}/_{S} \tag{5.1}$$

In this expression, the overbar ($\bar{}$) denotes a non-dimensional value. This same geometric scaling was then employed to ensure the same non-dimensional blade chord length and thickness for both rotors as a function of the non-dimensional blade length. In addition, the same airfoil shapes along both rotor blades were also employed.

Geometric angles between SUMR-D and SUMR-13 were maintained to the greatest degree possible by employing the same twist angle distribution along the non-dimensional span, as well as the same angles of blade pitch, rotor coning, and blade azimuthal position. In particular, the current parked tests focused on braked conditions (for which the rotor loads are highest) in the default T-position, so that the rotor had both blades parallel to the horizon. This fixed azimuthal configuration is a critical design load condition for two-bladed offshore wind turbines [25].

In general, turbines are designed such that the rated and cut-out operating conditions are relative to the average wind speeds. For the SUMR-13 design, the wind characteristics at hub-height are based on Class IIB conditions using the IEC 61400 standards [26]. This yields an average wind speed of 8.5 m/s and a 50-year gust wind speed of 59.5 m/s. The cut-in, rated, and cut-out wind speeds for SUMR-13 design were based on the NREL 5-MW (which is also a Class IIB turbine) wind speeds of 3 m/s, 11.3 m/s, and 25 m/s [15]. For a sub-scale system in operational conditions, the aerodynamic angles of attack and ratio of thrust to centrifugal loads can be consistently maintained between the scale and full-scale systems by employing the same tip-speed ratio and by scaling the wind speeds by $\eta^{1/2}$ [19]. Since the SUMR-D was designed to have the same aeroelastic scaling for both parked and operational conditions, this $\eta^{1/2}$ scaling also applies to cut-out conditions and the 50-year gust. Therefore, the cut-in, rated, and cut-out wind speeds for an ideally-scaled demonstrator are 1.34 m/s, 5.1 m/s, and 11.2 m/s while the ideally-scaled 50-year gust speed is 26.6 m/s. For ideal aeroelastic scaling, the SUMR-D should thus produce the same non-dimensional deflections at the same non-dimensional wind speeds as seen by SUMR-13. For example, the tip deflection (δ_{tip}) is normalized by blade length and the horizontal wind velocity upstream of the rotor (U_{horiz}) is normalized by the rated wind speed (U_{rated}) while a non-dimensional time is based on the ratio of the reference velocity and length scales. Based on the above, the non-dimensional blade tip deflections, wind speeds and time values are given as

$$\bar{\delta}_{\text{tip}} = {}^{\delta_{\text{tip}}}/_{S} \tag{5.2}$$

$$\bar{U}_{\text{horiz}} = {}^{U_{\text{horiz}}}/_{U_{\text{rated}}} \tag{5.3}$$

$$\bar{t} = {}^{tU_{\text{rated}}}/_{S} \tag{5.4}$$

To investigate the efficacy of this scaling, the non-dimensional aeroelastic tip deflections of the scaled system ($\bar{\delta}_{\text{tip,s}}$) can be compared to that of the full-scale system ($\bar{\delta}_{\text{tip,f}}$) at the same non-dimensional wind speed ($\bar{U}_{\text{horiz}}$).

This scaling can also be applied to the flapwise aerodynamic moments on the blade (M_{flap}). If one considers the parked blade in the pitch-to-run configuration, the blade is approximately perpendicular to the incoming flow so that the primary force is a drag force (as on a perpendicularly-oriented flat plate) for which the drag coefficient is about unity [27]. Assuming the drag coefficient is independent for the SUMR-D and SUMR-13 system scales (a reasonable assumption for their high Reynolds numbers [27]), the steady force on such a blade is proportional to the surface area (which scales with η^2) and the dynamic pressure of the incoming wind ($\frac{1}{2}\rho_{\text{wind}}U_{\text{horiz}}^2$), where ρ_{wind} is the air density at hub-height. The bending moments will be proportional to blade length and this force and so the overall moment scaling is $\left(\frac{\rho_{\text{wind,s}}}{\rho_{\text{wind,f}}}\right)\eta^4$. As such, the non-dimensional flapwise moment ($\bar{M}_{\text{flap}}$) for parked conditions can be defined as:

$$\bar{M}_{\text{flap}} = {}^{M_{\text{flap}}}\Big/_{S\rho_{wind}U_{\text{rated}}^2 S^4} \tag{5.5}$$

This same scaling occurs for a pitch-to-feather configuration where lift forces dominate so long as the angles of attack and non-dimensional blade geometry are consistent and so long as the lift coefficient curve does not vary significantly with Reynolds number.

Another key parameter needed for aeroelastic scaling is the overall blade flexibility. Since the non-dimensional tip deflection of a beam is proportional to the product of the moment applied and the beam length normalized by the overall beam stiffness (*EI*), this blade stiffness will scale with $\left(\frac{\rho_{\mathrm{wind,s}}}{\rho_{wind,\mathrm{f}}}\right)\eta^5$ since time scales as $\eta^{-1/2}$ based on Equation (5.4). Scaling the stiffness and frequency in this way for a simple beam with the same material density and structural design, would result in the blade mass scaling as η^3 [19]. However, the stiffness varies greatly along the length of the blade for the SUMR-13 design (as the case with most turbine blades), therefore ensuring matched blade deflections also requires the non-dimensional sectional stiffness (*EI*', stiffness per unit length) to be properly scaled which should be non-dimensionally preserved as a function of *s*/*S*, where

$$\overline{EI'} = {EI'}/{\rho_{wind} g S^5} \tag{5.6}$$

For parked conditions, the blade stiffness can be based on zero velocity conditions (since there is no centrifugal blade stiffening). Based on the above, the geometry, velocity, time, moment, and stiffness scaling relationships developed are listed in Table 5-1.

Table 5-1: Summarization of select scaling factors for the gravo-aeroelastic scaling method

Scaling Parameter	Scale Factor
Length Scaling: $\frac{\boldsymbol{S}_{\mathbf{s}}}{\boldsymbol{S}_{\mathbf{f}}}$	η
Wind Velocity Scaling: $\frac{\boldsymbol{U}_{\mathbf{s}}}{\boldsymbol{U}_{\mathbf{f}}}$	$\sqrt{\eta}$
Distributed Blade Mass Scaling: $\frac{\boldsymbol{m}'_{\mathbf{s}}}{\boldsymbol{m}'_{\mathbf{f}}}$	$\left(\frac{\rho_{\mathrm{wind,s}}}{\rho_{\mathrm{wind,f}}}\right)\eta^2$
Stiffness Scaling: $\frac{(\boldsymbol{EI'})_{\mathbf{s}}}{(\boldsymbol{EI'})_{\mathbf{f}}}$	$\left(\frac{\rho_{\mathrm{wind,s}}}{\rho_{\mathrm{wind,f}}}\right)\eta^5$

5.2.2 Test Facility and Demonstrator Turbine

As discussed above, the Segmented Ultralight Morphing Rotor (SUMR-13) was designed with 104-meter blades and includes a morphing hinge at the root in order to reduce loadings during operation [21,22,28–30]. The SUMR-Demonstrator (SUMR-D) is a 20% scaled model [9,10] designed to be tested on the 2-bladed Controls Advanced Research Turbine platform (CART-2) [31,32] at the National Renewable Energy Lab's Flatirons Campus (NREL FC). Parked conditions can generally include either idle conditions (blade is free to rotate) or braked conditions (blade is fixed at an azimuthal condition). Because braked conditions have the highest loads which provide a more direct computational evaluation, only the braked conditions were employed in this study. Consistent with IEC design load suggestions, the braked conditions focused on the blades parallel to the ground, so they are in a horizontal orientation. Furthermore, parked conditions are generally preferred to be in pitch-to-feather condition to reduce loads but the worst-case, fault in the pitch controller, pitch-to-run conditions should be investigated as a design load case. Figure 5-1 shows the SUMR-D blades as mounted on the CART-2 tower at the NREL FC with the blades parked in a horizontal T-position in a pitch-to-run configuration. The test included both pitch-to-run and pitch-to-feather configurations in the braked horizontal T-position.

Figure 5-1: The SUMR-D blades mounted on the 2-bladed Controls Advanced Research Turbine at the National Renewable Energy Lab's Flatirons Campus and placed in parked conditions.
Photo by Lee Jay Fingersh, NREL

As noted above, the full-scale SUMR-13 turbine is designed for Class IIB wind speeds (based on deployment in the Dominion offshore lease zone off the coast of Virginia) which prescribes a 50-year gust of 59.5 m/s and a turbulence intensity of 14% [33]. Based on the ideal wind scaling noted in Table 5-1, the aeroelastic design of the SUMR-D would be ideally tested at a site with a 50-year wind gust of 31.3 m/s and a turbulence intensity of 14%. Furthermore, the scaled rated wind speed (using for wind speed normalization per Eq. 5.3) is 5.1m/s and the scaled cut-out speed is 11.2 m/s. However, the sub-scale SUMR-D turbine was tested at the NREL FC and this site includes IEC Class IS (S: Special) winds which include 50-year gusts of ~70 m/s and a turbulence intensity of 18%. A positive consequence of the higher wind speeds is the NREL FC has a higher probability of wind speeds above the SUMR-D scaled cut-out wind speed (of 11.2 m/s) which helps in obtaining test data in high relative wind speeds for parked conditinos.

However, the high wind speeds and turbulence levels of the NREL FC testing site are much more than an ideally-scaled test site. This required the SUMR-D design to be much more structurally robust than would be dictated using ideal scaling. In particular, the inboard portion of the blade required extra structural mass than would be ideal based on Table 5-1 scaling. Figure 5-2 shows the non-dimensional distributed blade stiffness with higher values at the root due to the extra structural mass, which resulted in an overall heavier blade than the ideally scaled blade (Table 5-2). However, the outboard section had a mass and stiffness distribution which was more consistent with the scaled values. Since the outboard portion stiffness was more important for the blade deflection, this design compromise was intended to allow both aeroelastic scaling for the SUMR-D while ensuring safe deployment at the NREL FC.

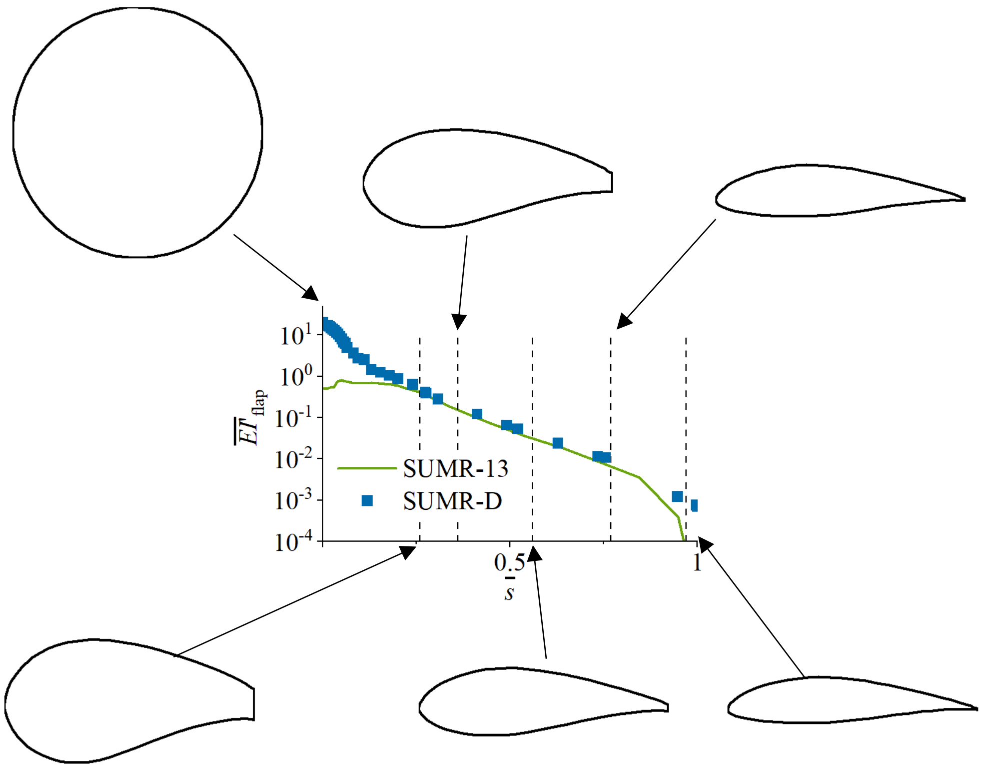

Figure 5-2: Non-dimensional blade sectional stiffness ($\overline{EI'}$) as a function of the non-dimensional span ($\bar{s}$) of the 13-MW Segmented Ultralight Morphing Rotor and the 20% scaled SUMR-Demonstrator; airfoil shapes (which were the same for both rotors) are also shown at select spanwise locations for the root, 26%, 36%, 56%, 77%, and 97% span.

Another constraint that needed to be considered was the blade coning angle. The CART-2 platform at the NREL FC contains an additional 3.7-degree shaft tilt which is not present in the SUMR-13 design and the platform lacks the ability for variable coning angle. To address these issues in the sub-scale rotor, a constant 12.5-degree coning angle adapter is attached at the root outboard of the pitch system. Since the coning angle for SUMR-13 for operation in above-rated conditions was designed to be in a constant angle of 12.5-degrees, this ensured that the coning angle for the SUMR-D was consistent with that for SUMR-13 in the worst-case condition of a pitch actuator fault and a pitch-to-run configuration. However, the employment of an adapter outboard of the pitch control system resulted in a pitch-coning coupling as function of pitch angle. In particular, a 12.5-degrees of coning (β = 12.5°) resulted when pitched to run (ϕ = 0°) while zero-degrees of coning (β = 0°) resulted when the pitched to feather (ϕ = 90°).

A summary of differences in characteristics between the SUMR-13 turbine, an ideal scaled SUMR-D turbine, and the as-built SUMR-D turbine are listed in Table 5-2. The ideal SUMR-D values are based upon the structure and environment of the full-scale SUMR-13 model with a 20% scaling factor applied. Due to the structural changes (as seen in Figure 5-2) to account for the wind speed differences between the NREL FC and the ideal test site environments, the rated velocity is increased in order to maximize the tip deflections during operation to match the full-scale system.

Table 5-2: Dimensional characteristics for the SUMR-D as fabricated and tested, the SUMR-D based on ideal aeroelastic scaling, and SUMR-13 as designed.

	SUMR-D	Ideal SUMR-D	SUMR-13
Blade length (S)	20.87 m	20.87 m	104.36 m
Rated velocity (U_{rated})	5.75 m/s	5.05 m/s	11.3 m/s
Cut-out velocity (U_{cut})	11.3 m/s	11.2 m/s	25 m/s
50-year gust ($U_{\text{50-year}}$)	~70 m/s	26.6 m/s	59.5 m/s
Blade mass (m)	985.6 kg	350.6 kg	54787 kg
Flapwise frequency (Hz)	1.13 Hz	1.21 Hz	0.54 Hz

5.2.3 Measurement of Wind Characteristics

To compare with tip deflections and root flap bending moments in parked conditions, detailed wind characteristics are recorded for the SUMR-D field tests at 400 Hz over a given test interval. A typical test interval was about 5-minutes (300 seconds) and about 20 test intervals were used for total averaging. The wind speeds are read by the sonic anemometer of the meteorological tower, which was located 86-meters west of the CART-2 platform. The three components of the wind speed (in the x, y, and z directions) are recorded at hub-height. The x-direction was aligned with the primary wind direction pointing towards the CART-2 turbine. Figure 5-3 shows the general layout of the CART-2 platform operating as a downwind rotor with the meteorological tower located 86 meters upwind of the turbine. The average wind shear is determined by averaging the gradient of the mean wind speed for a given test interval based on four cup anemometers distributed at 3 m, 15 m, 36.6 m and 52.8 m above ground level on the meteorological tower as shown in Figure 5-3. Additionally, a cup anemometer is located on the hub of the rotor to determine instantaneous horizontal wind speeds (U_{horiz}) acting on the rotor plane.

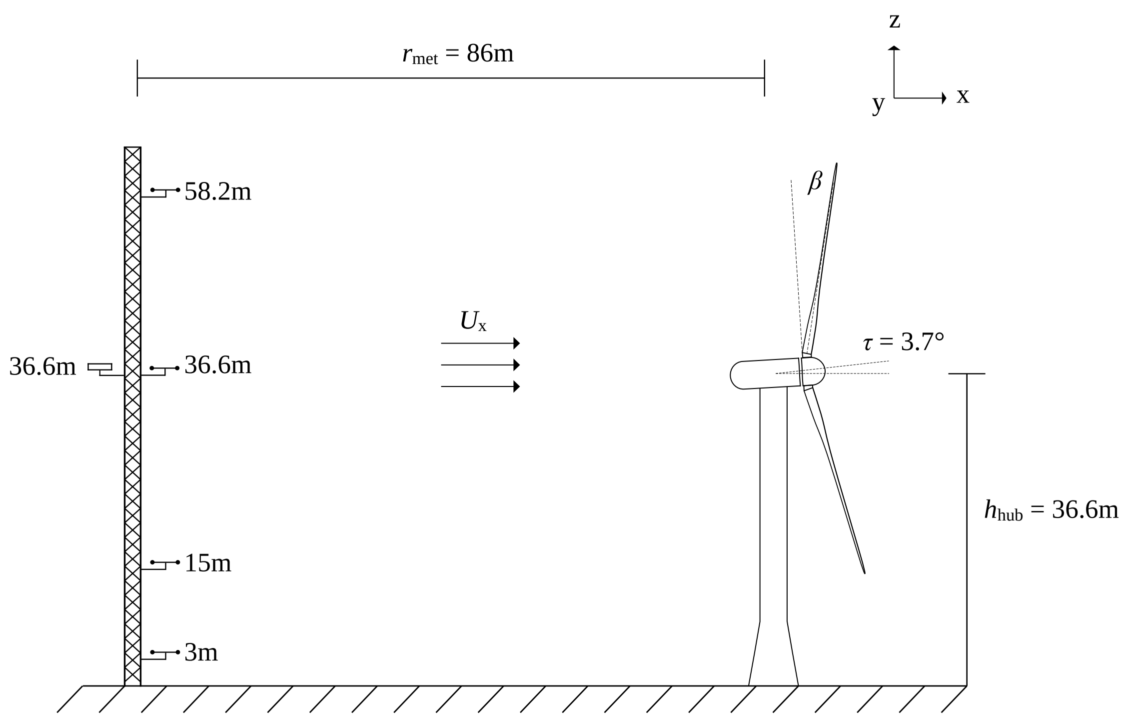

Figure 5-3: The 2-bladed Controls Advanced Research Turbine tower with a 3.7-degree shaft tilt (τ) outfitted with the 20% scale Segmented Ultralight Morphing Rotor blades and a variable coning angle (β) based upon blade pitch. A meteorological tower is located 36.6-meters upwind of the CART-2 turbine and contains four distributed cup anemometers and a sonic anemometer at hub-height.

Three data sets are analyzed within, one for each set of experimental results in the horizontal parked conditions: pitch-to-feather moments, pitch-to-run moments, and pitch-to-run deflections. Examples of horizontal wind speed data for a 300-second interval for moment data sets are shown in Figure 5-4. The data sets were selected to ensure well-characterized inflow conditions. In particular, the data were chosen based upon low cross wind conditions (less than 2 m/s average cross winds) so that the average cross-wind angle for all data would be less than 10-degrees. The data presented here were taken in October and November 2019, with the parked pitch-to-feather experiments from November 16 to 18 and the pitch-to run experiments on October 11 and 22. The total analyzed lengths of data sets were 105-minutes for the moments in the pitch-to-feather configuration, 105-minutes in pitch-to-run configuration, and about 100-minutes of data for blade deflections. Table 5-3 offers a summary of each of these datasets and the average mean characteristics over the entire dataset. The cross-wind angle was computed using the meteorological tower U_x, U_y, U_z wind speeds.

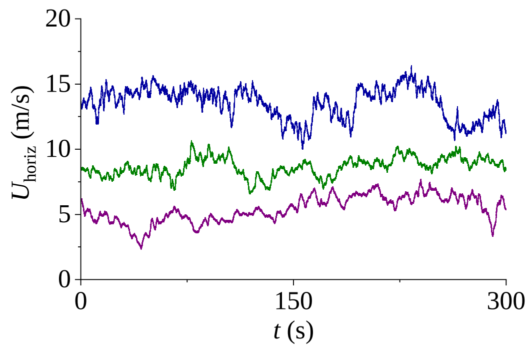

Figure 5-4: Three typical measured time variations of experimental wind speeds for the parked horizontal rotor configurations of the SUMR-D turbine for 5-minute intervals for a typical low, medium, and high average wind.

Table 5-3: Average wind characteristics of the SUMR-Demonstrator parked experiments

	Total Data Length (min)	Sampling Rate (Hz)	Mean Velocity (m/s)	Mean Turbulence Intensity (%)	Mean Crosswind Angle (degrees)
Pitch to Feather: Moments	105	400	9.7	18.8	6.5±16.9
Pitch to Run: Moments	105	400	13.4	22.6	-2.2±22.4
Pitch to Run: Deflections	100	30	12.9	30.8	-9.7±34.6

5.2.4 Moments

The turbine root bending strain gauges are located 48 cm outboard from the root of Blade 1 of the SUMR-D rotor. The Blade 1 strain gauges for the flapwise and edgewise components are oriented based on 0-degrees pitch of the blade. The strain gauge output was converted into blade moments with the blades mounted on the turbine and compared against predicted root bending moments. Due to the blades having higher mass than ideal, the low-wind gravitational moments are removed from the output bending moments. Additionally, temperature drift causes the calibrations of the strain gauges to shift; therefore, to remove the gravitational moments in low wind speeds, a quadratic best fit of moment relative to wind speed (which assumes loads are proportional to the dynamic pressure) is applied to the data in 15-minute increments to determine the zero-wind gravitational-only moments. This calibration approach minimizes the effects of temperature drift and allows removal of the calibrated zero-wind bending moments. As such, the bending moments presented herein are due solely due to aeroelastic effects.

It should be noted that the strain gauges are rated for a maximum of +/- 700 kN-m bending moments but the presented parked conditions rarely exceeded 10% of the total available strain gauge limits and typical operational values range from -100 kN-m to 100 kN-m. Combined with the aforementioned temperature drift and calibration, it is estimated the root bending strain gauges are accurate to about 5% of the average values.

5.2.5 Aeroelastic Deflections

In order to obtain the aeroelastic blade deflections, optical measurements were made of the tip deflection. To accomplish this, a video camera was mounted on the hub and captures an image of the field of view towards the tip of the blade at 30 frames per second. The camera is azimuthally attached to the blade but is mounted inboard of the pitch system and therefore the pitch-coning coupling limited the effective camera range of view. In particular, the camera is mounted such that the blade is in frame while pitched-to-run (12.5-degrees of coning), but out of frame while pitched-to-feather (0-degrees of coning). This is due to the coning occurring outboard of the pitch system, as summarized in Section 5.2.2. Therefore, only deflections in the pitch-to-run configuration are obtained.

To analyze deflections due to aeroelastic effects, a reference state was used for the blade in a static, low-wind, horizontal pitch-to-run state. Tabs are mounted at 8 m, 13 m and the tip of the blade, where these three tabs are denoted by the subscripts r, m, and t respectively. Figure 5-5a shows the reference image which refers to this reference state with the green arrows pointing towards the three tabs located along the blade and their pixel locations ($p_{x,0}$ and $p_{y,0}$). The number of pixels for the three reference distances between a set of two tabs ($l_{\text{tip}-8,0}$, $l_{\text{tip}-13,0}$, $l_{13-8,0}$) are found for no wind (no aeroelastic deflection) and these distances define the reference blade shape. The set of three pixel distance values during parked testing ($l_{\text{tip}-8}$, $l_{\text{tip}-13}$, l_{13-8}) for each frame of the desired video are found for each interval. Figure 5-5b shows an example frame during testing with the green x-marks depicting the locations of each tab. To determine when image corresponds to the reference frame (no net deflection), the root-mean-square error (L) of these values is determined as:

$$L = \sqrt{(l_{\text{tip}-8} - l_{\text{tip}-8,0})^2 + (l_{\text{tip}-13} - l_{\text{tip}-13,0})^2 + (l_{13-8} - l_{13-8,0})^2} \tag{5.7}$$

The frame of the desired video which minimizes this error is defined as the reference locations for each tab and the subsequent pixel deflection distances for aeroelastic deflection for an interval are found relative to these values.

a) b)

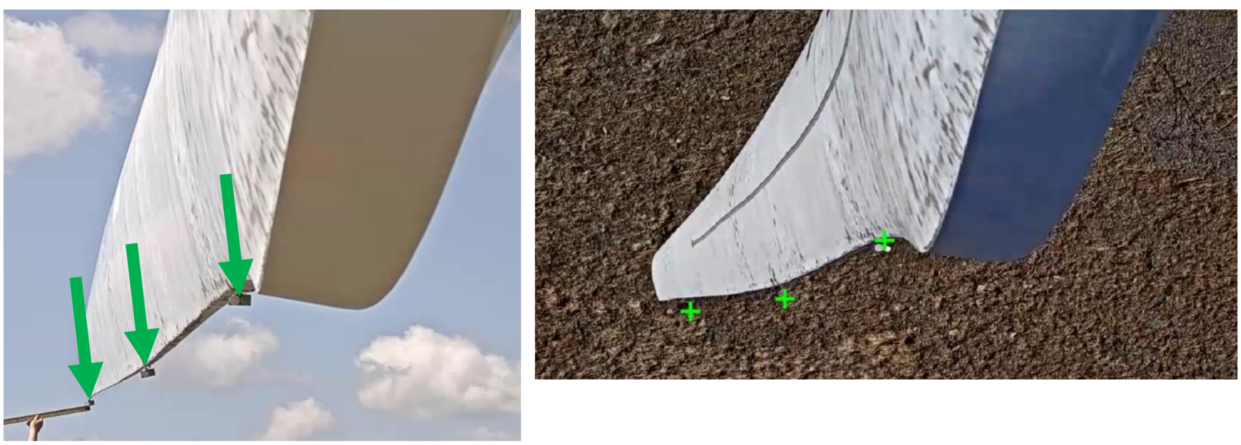

Figure 5-5: Tip deflection techniques showing a) the pixel calibration and b) a parked case with green plus (+) markers for all three tabs in the non-deflected state.
Photo by Lee Jay Fingersh, NREL

Figure 5-5a is also used for the blade deflection pixel-to-distance calibration at the tip of the blade. This pixel-to-distance conversion for the tip of the blade was measured to be 3.17 mm/pixel. The total distance of deflections is reported (δ_{tot}) by converting the current frame's pixel distances from the zero-location.

$$\delta_{\text{tot}} = \delta_{\text{tip,pixel}} \sqrt{(p_{\text{tip,x}} - p_{\text{tip,x,0}})^2 + (p_{\text{tip,y}} - p_{\text{tip,y,0}})^2} \tag{5.8}$$

Since the camera angle presents a singular two-dimensional plane of the blade, the deflection measured is based on a combination of bending or torsional deflection but does not include any out-of-place bending that can occur since the tabs are not location at the aeroelastic center of the blades. Such out-of-plane deflection is expected to be small such that the deflection errors are less than 5% of the average values.

5.2.6 *Computational Methods*

The experimental parked results are non-dimensionally compared against the computational SUMR-D and the computational SUMR-13 using FAST [34]. FAST is a wind turbine simulation software developed and maintained by NREL. The aerodynamic predictions employ two-dimensional airfoil results to evaluate three-dimensional rotor-blade performance. The FAST simulations use TurbSim v2 to create wind inputs designed to match the experimental wind field. These wind files are based on the sonic anemometer located on the meteorological tower to define the time series, average horizontal flow angles, and average vertical flow angles. Additionally, the cup anemometers on the meteorological tower are used to determine the power law exponent of the wind profile. An example of the horizontal velocity time-series as measured and as used by FAST for SUMR-D and SUMR-13 is shown in Figure 5-6 based on the non-dimensional velocity and time variables using Equations (5.3) and (5.4). While there are slight differences in the time series, the non-dimensional average mean and fluctuations for the simulations are consistent with experimental wind speeds.

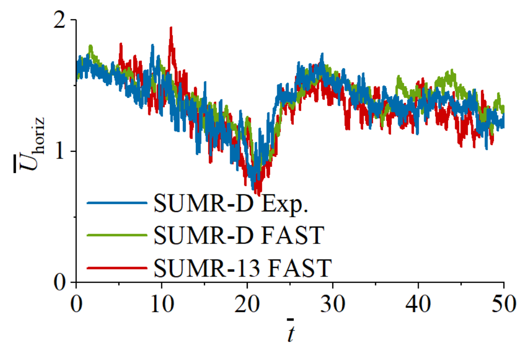

Figure 5-6: Example test interval of hub-height non-dimensional horizontal wind speeds normalized by the rated wind speed as a function of non-dimensional time for the SUMR-D experiments and the representative SUMR-D FAST and SUMR-13 FAST simulations.

The SUMR-13 structural and aerodynamic characteristics are based on computational designs [21] while the structural characteristics of the manufactured SUMR-D are respectively based on ground testing results. The SUMR-D structural characteristics employ a 'digital twin' of the stiffness distribution (Figure 5-2) which was constructed based on the manufactured model, ground testing, and total mass down the length of the blade [9].

FAST predicts the edgewise and flapwise moments in the rotor reference frame as a function of time at a variety of stations along the blade length. To compare the predicted moments with those that were measured, a consistent reference frame was needed. The experimental moments are located at the 48 cm marked on the blade (2.3% of blade length) and are aligned with 0-degree pitch on the blade (this data does not consider blade twist). In comparison, FAST predicted moments at the 2.3% span are aligned with the local airfoil twist (φ) of 13.5-degrees for the SUMR-13 blade and 34.3-degrees for the SUMR-D blade (and so do consider blade twist). To account for the differences in in reference frames due to blade twist, the flap and edge moments predicted by FAST are rotated and aligned (to be consistent with the experimental flapwise moment coordinate frame) as

$$M_{\text{flap}} = M_{\text{flap},\varphi} \cos\varphi - M_{\text{edge},\varphi} \sin\varphi \tag{5.9}$$

To analyze the effects of aerodynamics and compare to experimental data, each of the simulations are first run in zero-wind conditions for both pitch-to-run and pitch-to-feather to determine the moments due solely to gravity. These gravitational moments are then removed from the predicted moments allowing so only the effects of aeroelastic behavior on the blade bending moments are compared.

FAST also predicts both the edgewise and flapwise deflections separately. To compare these with the experimental total deflections, the two predicted deflection distances combine as

$$\delta_{\text{tot}} = \sqrt{\delta_{\text{flap}}^2 + \delta_{\text{edge}}^2} \tag{5.10}$$

Likewise with moments, each simulation is run in zero-wind conditions for both pitch-to-feather configuration and pitch-to-run configuration in order to obtain the deflections solely due to gravity. These effects are removed from the data to analyze the results of the aeroelastic behavior.

5.3 Results and Discussion

The following results first consider the experimental data moments to show overall data trends and statistical convergence. This is followed by comparisons with the SUMR-D simulations to assess FAST predictive ability and then by comparisons with SUMR-13 predictions to analyze the effectiveness of the gravo-aeroelastic scaling achieved by the SUMR-D turbine as fabricated. In all cases, the blades were in a horizontal position. Since FAST cannot capture the effects of an adapter located outboard of the pitch actuator, a 12.5-degrees of coning (β = 12.5°) was used in FAST when comparing with pitched to run (ϕ = 0°) while zero-degrees of coning (β = 0°) was used in FAST when predicting the pitched to feather conditions (ϕ = 90°).

5.3.1 Experimental Results

All the flapwise moment data are shown at the 2.3% span in the reference frame of the experimental strain gauges. For the parked experimental results, pitch-to-feather moments are first presented in Figure 5-7, which shows the Probability Distribution Function of the wind speeds in the data set based on 1 m/s bins. It can be seen that there is a significant amount of data above 11.2 m/s, the scaled cut-out wind speed of the SUMR-D rotor. This was due to the advantage of testing at NREL FC where there is a high probability of high wind speeds.

Figure 5-7b shows the mean and +/- one standard deviation of the flapwise moment for two sample bins (8-9 m/s and 16-17 m/s) as a function of percent of total available data per wind speed bin. As seen, the data shows reasonable convergence, e.g. there are only small differences between the results for 75% vs. 100% of the total data collected. This suggests that the mean data for each bin are converged to within about 5% of the mean. Using all data, Figure 5-7c shows the instantaneous flapwise bending moments as grey dots as well as the binned mean and standard deviations shown as blue solid and dashed lines. Since the blade is in a pitch-to-feather configuration for this data, the positive slope is attributed to lift and the new aerodynamic angle seen by the rotor (note quadratically with wind speed which is expected since the blade loads scale with U_{horiz}^2. Since the moment is defined as positive in the upwards direction and the blade surface has its suction surface pointed downward, the net aerodynamic angle is negative. , this results is consistent with the blade being suction side down. It can also be seen that there is a large variation of the instantaneous moment about the mean, especially at high wind speeds. This can be attributed to the large turbulence at NREL FC and influence of vertical velocity variations coupled with blade flexibility and dynamics which combine to produce in significant changes in the instantaneous aerodynamic angle.

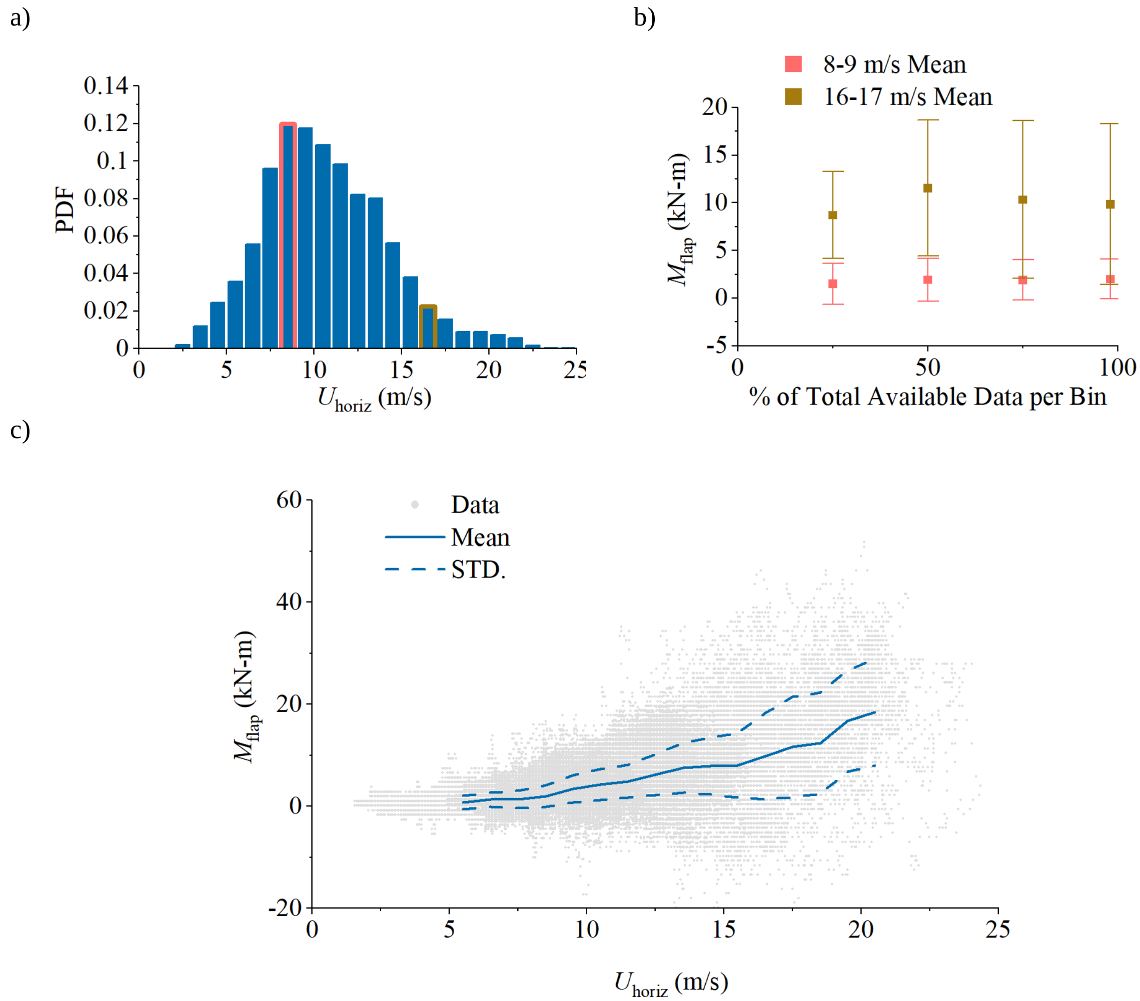

Figure 5-7: SUMR-D Experimental horizontal pitch-to-feather moment simulations with 105-minutes of data sampled at 400 Hz showing: a) the probability density of non-dimensional wind speeds with bins used for the convergence analysis highlighted, b) convergence analysis of the mean and standard deviations for two representative bins (8-9 m/s and 16-17 m/s) and c) the instantaneous non-dimensional flapwise bending moments as a function of the non-dimensional wind speeds along with the mean and ± one standard deviation based on 1 m/s bins.

Using similar analysis as in Figure 5-7, Figure 5-8 presents the flapwise bending moments for the experimental SUMR-D results in a pitch-to-run configuration. Figure 5-8a shows the distribution of windspeeds used for this study. Here it can be seen that the data resulted in even higher probability of high wind speeds, with as much as 50% of wind at speeds above the scaled cut-out speed of 11.2 m/s (for which the turbine is normally parked). Figure 5-8b again shows the convergence of average bending moments and their standard deviations based upon the percent of total data per bin. Again, the pitch-to-run moment data shows good convergence, with little changes occurring between the 75% and 100% data sets. This again suggests that the mean data for each bin are converged to within 5% of the mean values. The wind and moment data is shown in Figure 5-8c with grey symbols indicating instantaneous pitch-to-run moments and the blue solid and dashed lines respectively representing the mean and +/- one standard deviation about the mean. With the blades in a pitch-to-run configuration, the increase in bending moments as a function of windspeeds is due to the increase in drag on the rotor and as expected, the means scale with U_{horiz}^2. The mean values for the pitch-to-run condition are higher than that of the pitch to feather condition which is expected as the drag on a blade perpendicular to the wind his higher than the lift when aligned with the wind. Again, there is a large variation of the instantaneous moment about the mean, which can be attributed to the large turbulence at the NREL FC. In particular, the influence of streamwise velocity variations coupled with blade flexibility and dynamics combine to produce highly unsteady loadings.

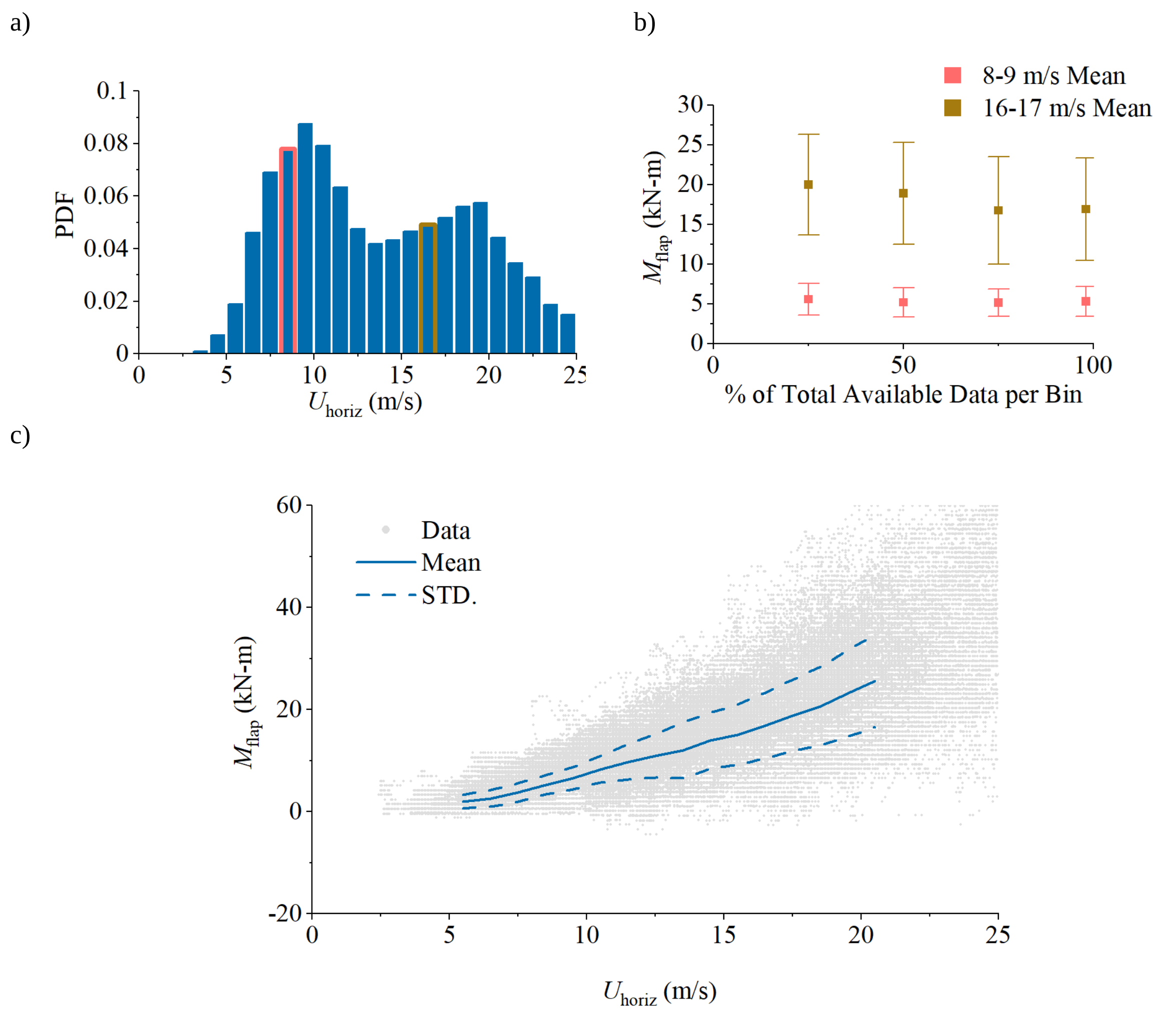

Figure 5-8: SUMR-D Experimental horizontal pitch-to-run moment simulations with 105-minutes of data sampled at 400 Hz showing a) the probability density of non-dimensional wind speeds with bins used for the convergence analysis highlighted, b) a visualization of the convergence of the mean and standard deviations for two representative bins (8-9 m/s and 16-17 m/s) and c) the distribution of non-dimensional flapwise bending moments over non-dimensional wind speeds showing the mean and ± one standard deviation.

Next, Figure 5-9 presents the blade deflections while in a pitch-to-run configuration for the distribution of wind speeds while Figure 5-9b shows the convergence of tip deflections. Again, there is substantial wind speed data above normal cut-out conditions and reasonable convergence is demonstrated. This results in Figure 5-9c which shows the horizontal, parked, pitch-to-run deflections. Again, grey symbols indicate instantaneous deflections while the solid and dashed blue lines represent the mean and +/- one standard deviation about said mean respectively. Similar to Figure 5-8c, the increase in tip deflections as a function of wind speeds is a result of an increase of drag on the blades and therefore scales with U_{horiz}^2. Again, there are large standard deviations which increase as the wind speed increases. It can be seen that the aeroelastic deflections can reach 600 mm (3% of blade length) during these conditions. For a full-scale system, this is consistent with deflections of 3.13 meters in parked conditions.

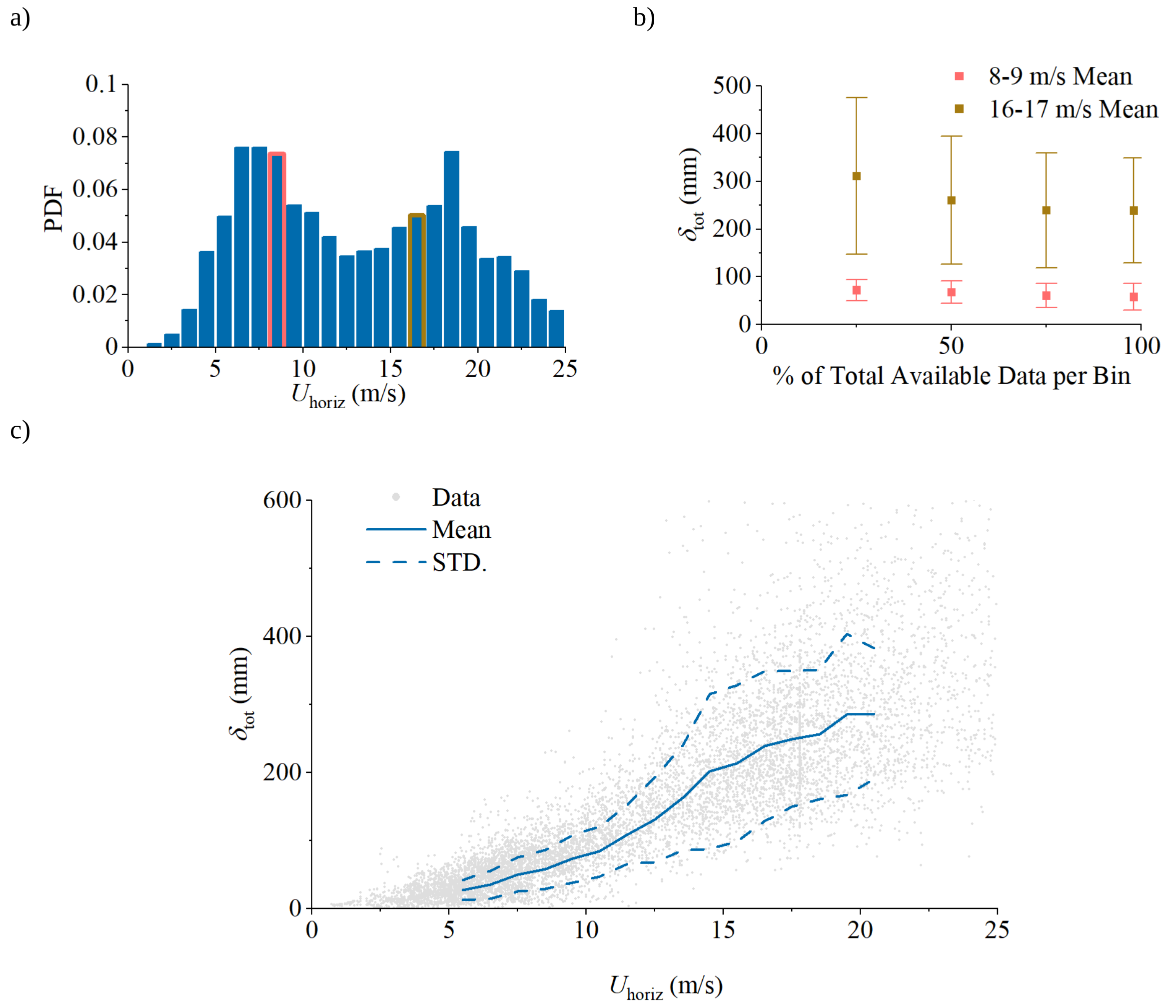

Figure 5-9: SUMR-D Experimental horizontal pitch-to-run deflections simulations with 100-minutes of data sampled at 30 Hz showing a) the probability density of non-dimensional wind speeds with bins used for the convergence analysis highlighted, b) a visualization of the convergence of the mean and standard deviations for two representative bins (8-9 m/s and 16-17 m/s) and c) the distribution of non-dimensional flapwise bending moments over non-dimensional wind speeds showing the mean and ± one standard deviation.

5.3.2 SUMR-D FAST Predictions

In order to assess the fidelity of FAST to predict the moments and deflections of a coned downwind turbine with advanced flatback airfoil design and highly flexible blades, the SUMR-D experimental results were compared to the SUMR-D FAST predictions with the same wind profiles. The FAST results are based on the same horizontal braked configuration as in the experimental results and are subjected to similar non-dimensional wind speeds as developed and summarized in Sections 5.2.3 and 0. For the following predictions and experiments, the data is again collected in 1 m/s bins.

Figure 5-10 presents the comparison of the SUMR-D experimental results against the SUMR-D FAST results for the parked, horizontal, pitch-to-run configurations. The solid lines represent the mean moments of each bin and the shading and dashed lines represent the standard deviations about said mean. The results show very good alignment between the experimental and computational data, where the mean moments and standard deviations similarly increase as the wind speeds increase. In general, the predictions tend to somewhat overpredict the experimental moments, indicating that the computational models for the SUMR-D blade aerodynamics may be over-predicting the coefficients of lift. However, the standard deviations of the moments for the predictions and experiments align quite well which indicates that the wind flow input files for turbulence intensity and the models of the structural characteristics (especially blade stiffness) are allowing the unsteady fluctuations of the blade be reasonable captured. Such good predictions are surprisingly good given the novel rotor design (downwind, coned, and high flexibility) and the high turbulence levels.

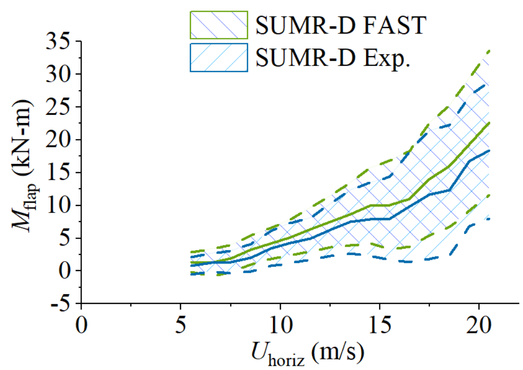

Figure 5-10: Comparison of SUMR-D experimental results to the SUMR-D FAST results with the solid lines depicting the means bending moments for the bins and the shaded regions and dashed lines depicting ± one standard deviations in a horizontal pitch-to-feather configuration.

Figure 5-11 continues the comparison of experimental SUMR-D results to computational SUMR-D results by analyzing the horizontal, parked, pitch-to-run moments and deflections. In this configuration, the flapwise bending moments are primarily due to airfoil drag (associated with highly separated flow conditions). It is apparent the computational results show a higher mean moment as compared to experimental results. The differences in mean values increase with an increase in wind speeds suggesting that the computational drag coefficient is significantly over-predicted. As currently specified, all the airfoils in the FAST simulations employ a two-dimensional drag coefficient of 2.01 at 90-degree angle of attack. This value is consistent with previous studies for flat plates. However, it is shown that three-dimensional results from wind tunnel testing of wind turbine blades indicate a significantly lower coefficient of drag [35]. Nonetheless, the standard deviations are quite similar for the FAST and experimental values further indicating, FAST has good capability in terms of predicting the unsteady loads despite the combination of high turbulence, high flexibility, and a complex rotor design.

a) b)

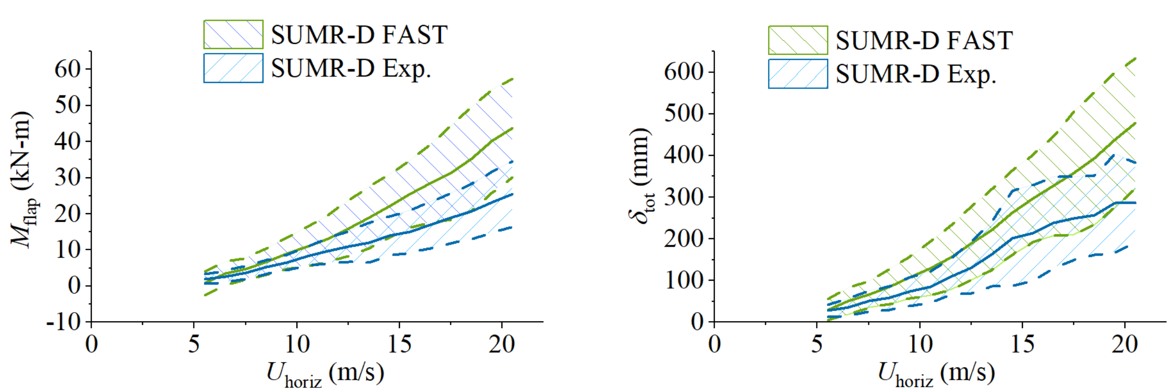

Figure 5-11: Comparison of SUMR-D experimental results to the SUMR-D FAST results with the solid lines depicting the means values for each bin and the shaded regions and dashed lines depicting ± one standard deviations for a) the flapwise bending moments and b) the deflection distances in a horizontal pitch-to-feather configuration.

5.3.3 Scaling Assessment of Demonstrator

Next, the experimental scaling method used is considered in terms of its ability to predict the full-scale SUMR-13 performance. The computational SUMR-13 model is put in the same configuration as the experimental cases and is subjected to similar non-dimensional wind speeds as summarized in Sections 5.2.3 and 0. Additionally, the SUMR-13 results are binned in similarly scaled bin sizes as the experimental SUMR-D bins (1 m/s) by applying the wind speed scaling summarized in Section 5.2.1 for a SUMR-13 bin size of ~2.23 m/s.

For the parked, horizontal, pitch-to-feather conditions, Figure 5-12a and 12b present the non-dimensional mean and standard deviations for the flapwise bending moments for the SUMR-D experimental, SUMR-D FAST, and SUMR-13 FAST results. Each of the mean results show good alignment through the range of wind speeds. Again, this indicates appropriate coefficients of lift for the computational SUMR-D, and it additionally indicates minimal effects of Reynolds number differences on the coefficient of lift. Figure 5-12b shows the standard deviations of each rotor with the SUMR-13 turbine exhibiting higher standard deviations than that of the SUMR-D rotors. This difference is attributed to the higher distributed stiffness of the manufactured blades (required for the NRLE FC site testing). A higher stiffness lends itself to having a higher restoring forces against fluctuations in the wind causing smaller blade fluctuations during turbulent conditions. Fluctuations at higher wind speeds may be due to low amounts of data at these higher wind speeds, but may also be associated with non-linear behavior of the blade dynamics. However, the overall response shows that the aeroelastic scaling approach can allow sub-scale system experimental testing that is highly reflective of full-scale design response. Considering the much lower costs associated with building and testing a 20% scale turbine compared to a full-scale, this indicates the enormous potential for sub-scale testing in validating novel extreme-scale turbines.

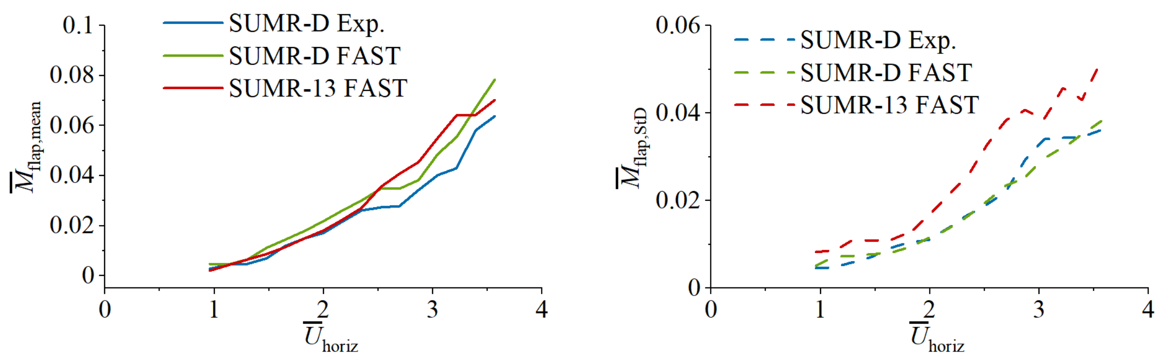

Figure 5-12: A non-dimensional comparison of the SUMR-D experimental data, SUMR-D FAST, and SUMR-13 FAST showing a) the means and b) the standard deviations of the horizontal pitch-to-feather bending moments.

Similar results are seen in Figure 5-13 for the horizontal, pitch-to-run configurations. Here, Figure 5-13a shows alignment of the mean flapwise bending moments for the FAST simulations which are higher than that of the experimental results. As explained and shown for Figure 5-11, this is due to using two-dimensional airfoil flat plate drag to predict the three-dimensional turbine results. As a result, the two-dimensional airfoils predict a higher coefficient of drag than what is in three-dimensional experiments and thus the simulations are over-predicting the experimental field results. Figure 5-13b presents the standard deviations of the rotor over the range of wind speeds. Similar to the pitch-to-feather conditions, FAST shows higher mean and fluctuating moments for the SUMR-13 than that of the SUMR-D which are attributed to higher blade stiffness in the sub-scale model.

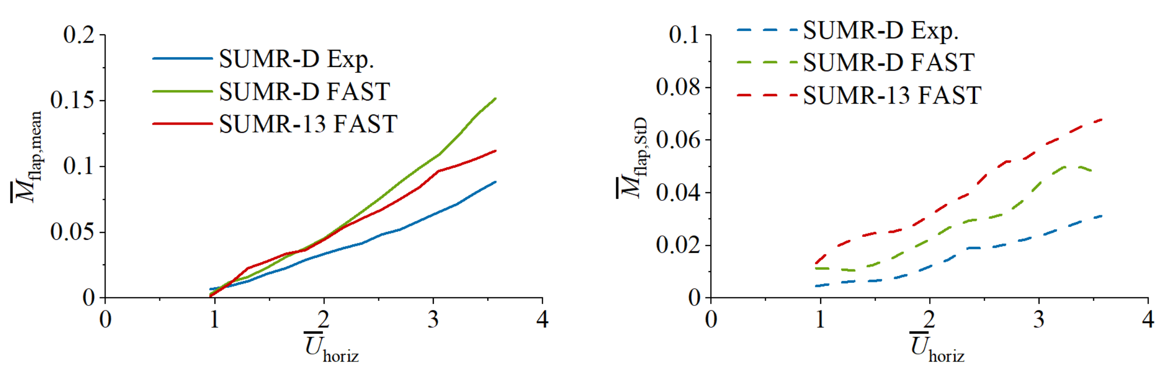

Figure 5-13: A non-dimensional comparison of the SUMR-D experimental data, SUMR-D FAST, and SUMR-13 FAST showing a) the means and b) the standard deviations of the horizontal pitch-to-run bending moments.

Finally, Figure 5-14 shows the deflection distances of a parked, horizontal, pitch-to-run configuration. Figure 5-14a and b present results similar to that seen in Figure 5-13, however the deflections have higher differences due to their additional sensitivity to bending stiffness. In particular, FAST predicts higher mean deflection values for the SUMR-13 FAST simulations than compared to that of the SUMR-D blades due to the lower stiffness of the SUMR-13 blades. Likewise, with the standard deviations, the mismatch in values indicates differing beam restoring forces and therefore stiffness in the blade model as previously concluded. As noted above, the differences in SUMR-D FAST and SUMR-D experimental results are attributed to the differences in the drag coefficient at high angles of attack. As such, the predicted deflections for SUMR-13 may be expected to be similarly over-predicted. However, the overall response again demonstrates that the aeroelastic approach employed in this study can allow sub-scale system experimental testing that is highly reflective of full-scale design of novel extreme-scale turbines.

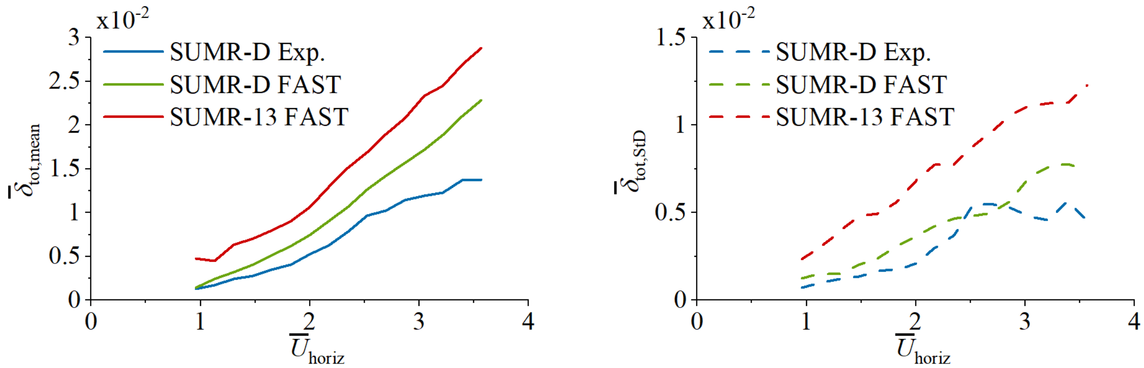

Figure 5-14: A non-dimensional comparison of the SUMR-D experimental data, SUMR-D FAST, and SUMR-13 FAST showing a) the means and b) the standard deviations of the horizontal pitch-to-run deflection distances.

5.4 Conclusions and Recommendations

This study presents the parked testing results of a gravo-aeroelastically scaled 20-meter sub-scale blade model of the 104.4 meter SUMR-13 blade. The sub-scale blades are designed for mounting on the 2-bladed CART-2 turbine and operated in a downwind configuration at the National Renewable Energy Laboratory's Flatiron Campus (NREL FC). Due to the NREL FC having higher than ideal wind speeds and turbulence, the demonstrator blades were designed and manufactured to have a higher non-dimensional mass and stiffness values as compared to the full-scale model. The parked testing presented is performed in the horizontal position in a pitch-to-feather configuration for flapwise bending moments and a pitch-to-run configuration for both flapwise bending moments and deflection distances.

The experimental results were compared against computational results for both the full-scale SUMR-13 and the 'digital twin' of the SUMR-D rotor. The computational results were run with FAST using input wind speeds from TurbSim v2 to reflect the experimental wind field. The results show the SUMR-D FAST simulations have a reasonable coefficient of lift but a higher coefficient of drag than those of the manufactured model due to the simulations using two-dimensional airfoil coefficients which are significantly different than three-dimensional results when the flow is separated. Additionally, the results confirm the SUMR-13 rotor has a lower blade stiffness than the sub-scale models as was expected due to the design of the manufactured model needing to withstand conditions at the NREL FC. Despite the designs being highly flexible as compared to conventional rotors, the system shows reasonable tip deflections at high wind speeds indicating the SUMR-13 concept (for which there was no previous experimental data) is a feasible design in terms of handling parked conditions for the extreme case of a braked setting with both pitch-to-feather and pitch-to-run configurations. This supports the viability of a downwind flexible rotor concept for extreme-scale turbines. In addition, the present experimental and computational results importantly show that the aeroelastic scaling approach proposed herein can allow sub-scale experimental testing that is highly reflective of full-scale design response. This scaling can be an enormous cost advantage for validating novel extreme-scale turbines.

It is recommended that future simulations correct for the aerodynamic differences between two-dimensional airfoil results and three-dimensional results to further improve upon the predicted dynamics of the highly flexible blades. It is also recommended to consider other potential improvement to the FAST method for further accuracy in parked condition simulations. Additionally, it is recommended to continue the study to analyze the operational conditions to further understand the efficacy of the FAST simulations as well as to further analyze and develop the gravo-aeroelastic scaling method.

References

[1] Bir, G., and Jonkman, J. M. "Aeroelastic Instabilities of Large Offshore and Onshore Wind Turbinesa." *Journal of Physics*, Vol. 75, 2007.

[2] Zalkind, D. S., Ananda, G. K., Chetan, M., Martin, D. P., Bay, C. J., Johnson, K. E., Loth, E., Griffith, D. T., Selig, M. S., and Pao, L. Y. "System-Level Design Studies for Large Rotors." *Wind Energy Science Discussions*, 2019, pp. 1–35. doi:10.5194/wes-2018-80.

[3] Li, Z., Wen, B., Dong, X., Peng, Z., Qu, Y., and Zhang, W. Aerodynamic and Aeroelastic Characteristics of Flexible Wind Turbine Blades under Periodic Unsteady Inflows | Elsevier Enhanced Reader.

[4] Madsen, P. H., Pierce, K., and Buhl, M. *Predicting Ultimate Loads for Wind Turbine Design Work Performed under Task Number WE903330*. 1999.

[5] Goude, A., and Rossander, M. "Force Measurements on a VAWT Blade in Parked Conditions." *Energies*, Vol. 10, No. 12, 2017. doi:10.3390/en10121954.

[6] Cotrell, J. *The Mechanical Design, Analysis, and Testing of a Two-Bladed Wind Turbine Hub*. 1993.

[7] Dagher, H., Viselli, A., Goupee, A., Kimball, R., and Allen, C. "The VolturnUS 1:8 Floating Wind Turbine: Design, Construction, Deployment, Testing, Retrieval, and Inspection of the First Grid-Connected Offshore Wind Turbine in US."

[8] Osgood, R., Bir, G., Mutha, H., Peeters, B., Luczak, M., and Sablon, G. *Full-Scale Modal Wind Turbine Tests: Comparing Shaker Excitation with Wind Excitation*. 2010.

[9] Yao, S., Griffith, D. T., Chetan, M., Bay, C. J., Damiani, R., Kaminski, M., and Loth, E. "A Gravo-Aeroelastically Scaled Wind Turbine Rotor at Field-Prototype Scale with Strict Structural Requirements." *Renewable Energy*, 2020. doi:10.1016/j.renene.2020.03.157.

[10] Bay, C. J., Damiani, R., Jay Fingersh, L., Hughes, S., Chetan, M., Yao, S., Todd Griffith, D., Ananda, G. K., Selig, M. S., Zalkind, D. S., Pao, L. Y., Martin, D., Johnson, K. E., Kaminski, M., and Loth, E. "Design and Testing of a Scaled Demonstrator Turbine at the National Wind Technology Center." *AIAA Scitech Forum*, 2019.

[11] Bottasso, C. L., Campagnolo, F., and Petrović, V. "Wind Tunnel Testing of Scaled Wind Turbine Models: Beyond Aerodynamics." *Journal of Wind Engineering and Industrial Aerodynamics*, Vol. 127, 2014, pp. 11–28. doi:10.1016/j.jweia.2014.01.009.

[12] Goupee, A. J., Koo, B. J., Kimball, R. W., Lambrakos, K. F., and Dagher, H. J. "Experimental Comparison of Three Floating Wind Turbine Concepts." *Journal of Offshore Mechanics and Arctic Engineering*, Vol. 136, No. 2, 2014. doi:10.1115/1.4025804.

[13] Viselli, A. M., Goupee, A. J., and Dagher, H. J. "Model Test of a 1:8-Scale Floating Wind Turbine Offshore in the Gulf of Maine." *Journal of Offshore Mechanics and Arctic Engineering*, 2015. doi:10.1115/1.4030381.

[14] Martin, H. R., Kimball, R. W., Viselli, A. M., and Goupee, A. J. "Methodology for Wind/Wave Basin Testing of Floating Offshore Wind Turbines." 2014. doi:10.1115/1.4025030.

[15] Jonkman, J. M., Butterfield, S., Musial, W., and Scott, G. *Definition of a 5-MW Reference Wind Turbine for Offshore System Development*. 2009.

[16] Viselli, A. M., Goupee, A. J., Dagher, H. J., and Allen, C. "Design and Model Confirmation of the Intermediate Scale VolturnUS Floating Wind Turbine Subjected to Its Extreme Design Conditions Offshore Maine." *Wind Energy*, Vol. 19, No. 6, 2016, pp. 1161–1177. doi:10.1002/we.

[17] Simms, D. A., Hand, M. M., Fingersh, L. J., and Jager, D. W. *Unsteady Aerodynamics Experiment Phases II-IV Test Configurations and Available Data Campaigns*. 1999.

[18] Noyes, C., Qin, C., and Loth, E. "Tower Shadow Induced Blade Loads for an Extreme-scale Downwind Turbine." *Wind Energy*, Vol. 23, No. 3, 2020, pp. 458–470. doi:10.1002/we.2415.

[19] Kaminski, M., Loth, E., Griffith, D. T., and Qin, C. (Chris). "Ground Testing of a 1% Gravo-Aeroelastically Scaled Additively- Manufactured Wind Turbine Blade with Bio-Inspired Structural Design." *Journal of Renewable Energy*, Vol. 148, 2020, pp. 639–650. doi:10.1016/j.renene.2019.10.152.

[20] Griffith, D. T., and Richards, P. W. *The SNL100-03 Blade : Design Studies with Flatback Airfoils for the Sandia 100-Meter Blade*. 2014.

[21] Ananda, G. K., Bansal, S., and Selig, M. S. "Aerodynamic Design of the 13.2 MW SUMR-13i Wind Turbine Rotor." *AIAA SciTech Forum*, 2018. doi:10.2514/6.2018-0994.

[22] Noyes, C., Qin, C., and Loth, E. "Pre-Aligned Downwind Rotor for a 13.2 MW Wind Turbine." *Renewable Energy*, Vol. 116, 2018, pp. 749–754. doi:10.1016/j.renene.2017.10.019.

[23] Ichter, B., Steele, A., Loth, E., Moriarty, P., and Selig, M. S. "Amorphing Downwind-Aligned Rotor Concept Based on a 13-MW Wind Turbine." *Wind Energy*, Vol. 19, No. 4, 2016, pp. 625–637. doi:10.1002/we.

[24] Loth, E., Steele, A., Qin, C., Ichter, B., Selig, M. S., and Moriarty, P. "Downwind Pre-Aligned Rotors for Extreme-Scale Wind Turbines." *Wind Energy*, Vol. 20, No. 7, 2017, pp. 1241–1259. doi:10.1002/we.

[25] Kim, T., Larsen, T. J., and Yde, A. "Investigation of Potential Extreme Load Reduction for a Two-Bladed Upwind Turbine with Partial Pitch." *Wind Energy*, Vol. 18, No. 8, 2015, pp. 1403–1419. doi:10.1002/we.1766.

[26] International Eletrotechnical Commision. "IEC 61400-1 Wind Turbines - Part 1: Design Requirements." *Wind turbines – Part 1: Design requirements*, Vol. 2005, 2005, pp. 1–92. doi:10.1055/s-2007-985912.

[27] Igarashi, T., and Terachi, N. "Drag Reduction of Flat Plate Normal to Airstream by Flow Control Using a Rod." *Journal of Wind Engineering and Industrial Aerodynamics*, Vol. 90, No. 4–5, 2002, pp. 359–376. doi:10.1016/S0167-6105(01)00198-2.

[28] Loth, E., Selig, M. S., and Moriarty, P. "Morphing Segmented Wind Turbine Concept." *AIAA Applied Aerodynamics Conference*, No. July, 2010, pp. 1–6. doi:10.2514/6.2010-4400.

[29] Loth, E., Steele, A., Ichter, B., Selig, M. S., and Moriarty, P. Segmented Ultralight Pre - Aligned Rotor for Extreme - Scale Wind Turbines. 2012.

[30] Noyes, C., Qin, C., and Loth, E. Ultralight, Morphing Rotor for Extreme-Scale Wind Turbines. 2017.

[31] Bossanyi, E. A., Wright, A. D., and Fleming, P. A. *Controller Field Tests on the NREL CART2 Turbine*. 2010.

[32] K.A. Stol. "Geometry and Structural Properties for the Controls Advanced Research Turbine (CART) from Model Tuning." *Nrel/Sr*, No. September, 2004, pp. 500–32087.

[33] Virginia Offshore 90-Meter Wind Map and Wind Resource Potential. https://windexchange.energy.gov/maps-data/237. Accessed Dec. 9, 2019.

[34] Jonkman, J. M., and Buhl, M. L. *FAST User's Guide*. 2005.

[35] Spera, D. *Models of Lift and Drag Coeffi Cients of Stalled and Unstalled Airfoils in Wind Turbines and Wind Tunnels*. 2008.

[36] McTavish, S., Feszty, D., and Nitzsche, F. "Evaluating Reynolds Number Effects in Small-Scale Wind Turbine Experiments." *Journal of Wind Engineering and Industrial Aerodynamics*, 2013. doi:10.1016/j.jweia.2013.07.006.

6. Gravo-Aeroelastically-Scaled Demonstrator Tests to Represent an Extreme-Scale Downwind Turbine

Abstract:

Operational experimental testing results for a 44.5 m diameter wind turbine rotor were obtained to investigate aeroelastic flapwise moments and blade deflections of a novel downwind coned design with lightweight flexible blades. These results were non-dimensionally compared against FAST computational results for the digital twin of the manufactured sub-scale rotor as well as the full-scale concept rotor. The full-scale rotor is the 13-MW Segmented Ultralight Morphing Rotor (SUMR-13), which is a 2-bladed downwind rotor that achieves lightweight performance through flapwise load alignment. The sub-scale demonstrator rotor (SUMR-D) that was tested at 1/5th scale and designed using a gravo-aeroelastic scaling method to match the nondimensional gravo-aeroelastic flapwise loads, deflections, and dynamics of its full-scale counterpart. The sub-scale model was tested at The National Renewable Energy Laboratory's Flatirons Campus (NREL FC) which includes 50-year gusts which are 2.5 times higher than that of an ideally-scaled environment. To withstand the NREL FC site conditions, the manufactured SUMR-D rotor employed higher inboard non-dimensional mass density and stiffness relative to that for an ideally-scaled 20% model. To accommodate this difference, operational conditions were adjusted so the SUMR-D rotor could reasonably capture the scaled aeroelastic characteristics of the SUMR-13 rotor. The SUMR-D experimental results are compared with simulations from SUMR-D and SUMR-13 through key non-dimensional characteristics: rotor tip-speed ratios, RPM normalized by the first flapping frequency, tip deflections normalized by the blade length, and the normalized flapwise bending moments. Despite the enhanced blade robustness required for NREL FC testing, the sub-scale experimental model is able to reasonably represent the predicted dynamics in FAST. This included the operational conditions and loads in Region 3 and the tip deflections in Region 2. The results indicated that the Segmented Ultralight Morphing Rotor concept can successfully employ load-alignment and flexibility to achieve a lightweight rotor. The results also show that FAST generally provides reasonable predictions though further improvements can be made to the control system to more closely match that of the experimental results. Finally, the success of the first aeroelastically-scaled turbine operational field tests demonstrate the potential of low-cost high-fidelity sub-scale testing for novel extreme-scale turbine designs.

Nomenclature

a	=	speed of sound
EI	=	blade stiffness
g	=	gravitational constant
L	=	RMS error
l	=	distance between tabs
m	=	blade mass
M	=	moment
Ma	=	Mach Number
p	=	pixel location
Re	=	Reynolds Number
r	=	distance
s	=	spanwise location
S	=	total blade length
TI	=	turbulence intensity
t	=	time
U	=	wind speed
β	=	cone angle
δ	=	deflection
η	=	scaling factor
ρ	=	density
ϕ	=	blade pitch
λ	=	tip-speed ratio
μ	=	dynamic viscosity
Ω	=	rotor rotational rate
ω	=	blade frequency
Ψ	=	azimuth angle
φ	=	local airfoil twist angle

Subscripts

$()_0$	=	reference value
$()_{50-\mathrm{year}}$	=	50-year gust
$()_{\mathrm{adapter}}$	=	adapter value
$()_{\mathrm{edge}}$	=	edgewise value
$()_{\mathrm{eff}}$	=	effective value
$()_{\mathrm{f}}$	=	full-scale value
$()_{\mathrm{flap}}$	=	flapwise value
$()_{\mathrm{hub}}$	=	hub value
$()_{\mathrm{horiz}}$	=	horizontal value
$()_{\mathrm{pixel}}$	=	pixel to distance conversion
$()_{\mathrm{rated}}$	=	rated value
$()_{\mathrm{s}}$	=	sub-scale value
$()_{\mathrm{tot}}$	=	distance value
$()_{\mathrm{tip}}$	=	tip value
$()_{\mathrm{wind}}$	=	wind value
$()_{\mathrm{x,y,z}}$	=	coordinate frame
$()_{xx}$	=	tab distance from root (m)
$()'$	=	spanwise distributed value
$\overline{()}$	=	non-dimensional value

6.1 Introduction

6.1.1 Motivation for Operational Sub-scale Testing of Flexible Rotors

Offshore wind turbines are beginning to make their way into the American market with wind turbines being deployed off Rhode Island, Maine, and Virginia [1–3]. With states like Virginia recently passing clean energy legislation [1], it is expected for the offshore wind energy market to continue to grow to meet these needs. However, such turbines continue to have higher Levelized Cost of Energy (LCOE) as compared to onshore turbines [4]. As such, a common trend to help reduce the LCOE is to utilize larger turbines which have a larger swept area as well a higher hub height allowing access to higher atmospheric wind speeds [5–10]. For upwind rotors, this size growth may be limited due to the subsequent increase in blade length and flexibility which creates higher probability of tower strike and unwanted aeroelastic dynamics. Downwind rotors present an opportunity to alleviate these issues in long blades by allowing the blades to bend away from the tower at high thrust loadings, thereby reducing the blade structural requirements [11]. In addition, a recent downwind turbine concept uses flapwise load-alignment to reduce the flapwise loads and the corresponding structural requirements [12]. This load-aligning concept has been predicted (but never experimentally tested) to create lighter blades which can reduce the Levelized Cost of Energy. Such downwind configurations may allow turbines to increase in size and flexibility beyond that of conventional rotors today, i.e. to scales as large as 25 MW [13]. Unfortunately, current simulations are designed for conventional upwind rotors [14] and the accuracy of these simulations for downwind extreme-scale turbines with highly-flexible and highly-coned blades is unknown. This is because there are no experimental field test results for such designs to use as validation. It should be noted that full-scale turbine construction and testing would be inordinately expensive. To avoid these high costs, sub-scale experimental tests is an obvious practical opportunity since such testing for upwind designs have been highly informative [3] and cost-effective [11]. As such, there is a critical need for sub-scale experimental field test for the next generation of extreme-scale downwind turbines that can describe the aeroealstic operational behavior of the next generation of extreme-scale wind turbines.

6.1.2 Previous Sub-scale Testing

Previous sub-scale wind turbine models have been used to de-risk full-scale turbine designs such as the 1/50th scaled tests of the computational NREL 5-MW turbine [15,16]. These sub-scale designs were based on Froude scaling to ensure the wind-wave loads on the rotor and off-shore platform are non-dimensionally equivalent to those on a full-scale design [17,18]. To make up for Reynolds number mismatch in experiments, the study increased the model wind speed. To support the sub-scale experimental tests, a computational study was performed on the sub-scale rotor except the airfoils were redesigned in order to make up for the Reynolds number mismatch to achieve similar thrust and power coefficients [17]. Matching thrust and power of the rotor helped match the aerodynamic forces on the turbine platform, which was critical to scale the hydrodynamic response and stability of these floating turbines.

Additionally, three, 11-kW turbines were designed and deployed as sub-scale floating turbines for the Poseidon wind/wave prototype design which extracts both wind and wave energy [19,20]. In addition, a 1/8th scale rotor was deployed to replicate the full-scale Vulturn-US (with a 76.8 meter diameter turbine) to understand the wind/wave loads on a semi-submersible hull for a floating turbine [3,21,22].

For conventional onshore turbines, sub-scaling was employed to understand wind turbine wakes between multiple turbines at Sandia National Lab's SWiFT facility. These sub-scale turbines were designed to be large enough to represent the important physics of the wake interactions between turbines, yet small enough to be cost effective [23]. However, all the above sub-scale studies were based on conventional upwind rotor designs and conventional full-scale turbine sizes (less than 10 MW) and so rotor aeroelastic aspects were not critical. As a result, a stiff rotor was employed for the sub-scale models. Hence, scaling blade mass and stiffness and examining blade loads and deflections were not a priority. If one shifts attention to an extreme-scale lightweight rotor design, such properties and responses now become critical as the blades are much more flexible and their response is much more complex and important. Because extreme-scale turbines (greater than 10 MW) are new, no sub-scale testing have been previously conducted to replicate the aeroelastic operational behavior of extreme-scale turbines (neither for upwind nor downwind rotor configurations). As a result, there is no assessment of current computational capabilities to predict blade deflections and loads in operational conditions for flexible rotors (neither for upwind nor downwind rotor configurations).

In order to capture the gravo-aeroelastic properties of such extreme-scale blades at subscale conditions, a theoretical gravo-aeroelastic scaling (GAS) method was developed for operational conditions [24–26]. This scaling method seeks to replicate the load distributions on the blades (due to centrifugal, aerodynamic, and gravitational forces) and the associated blade deflections and dynamics. The first study to employ the GAS method is the 1% model [24] of the 100-meter SNL100-03 rotor [10]. This model utilized additive manufacturing and a bio-inspired design for the internal structure to match the full-scale mass and stiffness distributions so that blade static and dynamic deflections could be replicated. The static and dynamic deflections were investigated using ground testing with artificially applied distributed forces along the span of the blade that approximated the operational aerodynamic forces. The results showed that non-dimensional tip deflection, blade frequency, and blade mass could be reasonably captured with a sub-scale blade in a ground test. However, GAS has not been assessed for operational performance of a turbine in field conditions.

To make progress towards such an assessment, the GAS method was used to design a 20% scaled rotor of the 13-MW Segmented Ultralight Morphing Rotor (SUMR-13) for operational field testing. The SUMR-13 is a downwind, coned, 2-bladed turbine with 104-meter blades. The sub-scale model was designed and mounted at the National Renewable Energy Laboratory's Flatirons Campus (NREL FC) on the 2-bladed Controls Advanced Research Turbine (CART-2). The SUMR-D turbine is one of the largest downwind research turbines designed and installed with highly flexible blades in the last decade and the first research turbine to employ the flapwise load-aligned concept. It was designed, fabricated, and installed as a field-scale demonstration to determine whether the SUMR concept is a viable design and to examine whether the GAS approach for sub-scale systems can mimic the aeroelastic performance of an extreme-scale rotor, especially those with novel designs and/or high flexibility.

6.1.3 Study Objectives

To capture the dynamic properties of a highly flexible rotor within field-testing constraints, the gravo-aeroelastic scaling method was applied to design a sub-scale turbine for operation at the NREL FC in order to mimic the operational behavior of the full-scale SUMR-13 turbine in its designed Class IIB wind class conditions [27–30]. To investigate the sub-scale model's ability to represent the full-scale dynamics and deflections, operational experimental data were obtained for a wide range of wind velocities with significant inflow turbulence over a period of several months. To the authors' knowledge, these tests provide the first moment and deflection data of a downwind load-aligned flexible rotor in realistic wind conditions. These are also the first field tests to employ the GAS method for operational conditions and the first tests to deploy a subscale model that is aeroelastically consistent with that of an extreme-scale turbine. This data set may thus serve as a valuable database for future wind turbine research on extreme-scale (>10 MW) turbines.

The experimental results were also presented and compared against computational simulations that integrate the inflow turbulent field, the blade aeroelastic properties and a representative controller for this downwind load-aligned design. To the authors' knowledge, this is the first computational predictions of a downwind load-aligned flexible turbine based on actual site conditions using measured wind velocities and characteristics and the first to evaluate the capability of computations to predict operational rotor moments and deflections for such a highly-flexible and highly-coned downwind flexible rotor. Evaluating the accuracy of the predictions is important to assess and validate the fidelity of modern simulation tools for extreme-scale wind turbine designs. Finally, it is also the first study to combine experimental and computational results to evaluate the efficacy of gravo-aeroelastic scaling for operational conditions.

In the following, Section 6.2 describes the methods for developing the sub-scale model within site testing constraints, the experimental data collection approaches and associated data processing, and the computational methods for turbine performance. Section 6.3 includes the results and discussions of the experimental data as well as comparison to computational predictions. Finally, Section 6.4 provides concluding remarks and recommendations of future studies.

6.2 Methods: Scaling, Experimental, and Computational

6.2.1 Gravo-Aeroelastic Scaling

Extreme-scale rotor designs (>100-meter blade lengths) [5,10,12,27,31–33] are generally more flexible and exhibit greater aeroelastic dynamics as compared to those seen in conventional rotors. In general, the fidelity of computational models is unknown for representing these types of rotors in operation since there have been no published experimental results and comparisons with predictions. This is especially true for novel designs with downwind, coned, and/or load aligned blades. To examine these effects and the efficacy of the current computational models, physical models must be developed and tested. However, full-scale models can be quite expensive in terms of both cost and time, therefore sub-scale models can be highly beneficial if they can represent the full-scale rotor aeroelastic dynamics.

To examine the effects of highly elastic blades at the sub-scale size, a gravo-aeroelastic scaling method has been theoretically developed which would allow for a sub-scale model to behave similarly to that at the full-scale [24]. Since flapwise moments and deflections become critical at extreme-scale sizes, they are the focus herein for aeroelastic response. To achieve this, parameters are defined as the most critical to be held constant between the sub-scale and full-scale rotors: blade geometry, tip-speed ratio, rotor speed relative to flapwise frequency, non-dimensional flapwise moments, and non-dimensional tip deflections. These five parameters are defined in more details below.

1) Nondimensional blade geometry can be invoked using a scaling factor (η) which represents the ratio of the subscale blade length (S_s) to the full-scale blade length (S_f). This scaling factor is also applied to all external geometric properties for a geometrically-scaled rotor, matching the airfoil thickness, chord, etc. along the nondimensional spanwise length ($\bar{s}$), defined as the local spanwise location (s) normalized by the blade length (where s = 0 refers to the root of the blade). The scaling factor and the non-dimensional spanwise length are thus given as

$$\eta = {}^{S_s}/_{S_f} \tag{6.1}$$

$$\bar{s} = {}^{s}/_{S} \tag{6.2}$$

2) Rotor Tip-Speed Ratio (λ) is the ratio of the speed of the rotor tip relative to the upstream wind speed. It is a function of the rotational speed (Ω), radius of the hub and any needed adapters (r_{hub} and r_{adapter}), the blade length, the effective coning angle (β_{eff}) and the horizontal wind speed (U_{horiz}). Matching this ensures the full-scale flow angles over the blade during operation are seen in the sub-scale model ensuring proper aerodynamics on the rotor as long as the Reynold's number effects are kept to a minimum. The non-dimensional tip-speed ratio that incorporates these effects is given as

$$\lambda = \frac{\Omega[r_{\text{hub}} + r_{\text{adapter}} + S\cos(\beta_{\text{eff}})]}{U_{\text{horiz}}} \tag{6.3}$$

3) Nondimensional Rotational Rate ($\bar{\Omega}$) is the blade the rotational speed normalized by the blade flapwise frequency (ω_{flap}) at the specific rotational speed. Matching this ensures the input frequencies (Ω) of the rotor to output frequencies (ω_{flap}) of the blade are matched which ensures the dynamics which appear at the full-scale are also seen at the sub-scale. The non-dimensional rotation rate is defined as

$$\bar{\Omega} = {}^{\Omega}/_{\omega_{\text{flap}}} \tag{6.4}$$

4) Nondimensional flapwise moments ($\bar{M}$) of the rotor are a result of the blade loadings that cause blade flapwise deflections (mean and unsteady) and are direct indicators of the degree of load alignment (where no flapwise moment indicates a perfectly load-aligned condition). Based on dynamic pressure, surface area, and moment arm length, these moments scale as a function of the air density (ρ_{wind}), the square of the rated wind speed (U_{rated}) and the cube of the rotor blade length, so the non-dimensional flapwise moments are given as:

$$\bar{M}_{\text{flap}} = {}^{M_{\text{flap}}}/_{\rho_{\text{wind}} U_{\text{rated}}^2 S^3} \tag{6.5}$$

5) Nondimensional Tip Deflections ($\bar{\delta}_{\text{tot}}$) is the ratio of the blade tip deflection distance (δ_{tot}) normalized by the full blade length (S). When this value matches the full- to sub-scale models over a range of wind speeds for both mean and unsteady components, the system is properly aeroelastically scaled. The non-dimensional deflection is thus

$$\bar{\delta}_{\text{tot}} = {}^{\delta_{\text{tot}}}/_{S} \tag{6.6}$$

It should be noted that the first three parameters effectively are used to control a turbine operation while the last two parameters are responses for the rotor under such control given the wind test conditions and blade properties. The scaling for the wind and structural characteristics are discussed in the following.

For operational conditions, the aerodynamic angles of attack and ratio of thrust to centrifugal loads should also be maintained for accurate scaling between the full- and sub-scale systems. This can be achieved by employing the same tip-speed ratio and Froude scaling such that the wind speeds scale by $\eta^{1/2}$ [24]. As such, the nondimensional horizontal wind speeds ($\overline{U}_{\text{horiz}}$) is defined as the local horizontal wind speed (U_{horiz}) normalized by the defined rated wind speed (U_{rated}).

$$\overline{U}_{\text{horiz}} = {}^{U_{\text{horiz}}}/_{U_{\text{rated}}} \tag{6.7}$$

This same velocity scaling can be used for the other two components of the wind velocity as a function of time and for the time-averaged non-dimensional turbulence levels and wind shear (used to further scale the wind characteristics).

As mentioned, extreme-scale rotors exhibit highly elastic behaviors which are influenced by the mass distribution of the blade as well as the stiffness distribution of the blade. Therefore, it is additionally important to match the nondimensional mass and stiffness distributions of the blade structure as close as possible to maintain the aforementioned goals of matching the blade moments and deflections. Based on aerodynamic and gravitational loads, the non-dimensional mass and stiffness values can be non-dimensionalized by the density of the air (ρ_{wind}) and the gravitational acceleration (g).

$$\overline{m'} = {}^{m'}/_{\rho_{\text{wind}} S^2} \tag{6.8}$$

$$\overline{EI'} = \frac{EI'}{\rho_{\text{wind}} g S^5} \tag{6.9}$$

For simple beam bending, which holds true to wind turbine blades, the steady distributed deflections are proportional to the moment applied as $\delta' = M/EI'$. Thus, matching the aerodynamic bending moments and distributed stiffness will match the aerodynamic deflections. As such, during operation, a primary factor in the deflection dynamics is the blade root bending moment.

Finally, Reynolds number and Mach numbers are mismatched during operation. The differences in Mach number can be reasonably ignored due to the system operating below the effects of compressibility. However, the Reynolds number does provide differences in the aerodynamics which were determined to have an insignificant effect of the dynamics at this scale as shown in Chapter 2. The scaling parameters for various properties are summarized in Table 6-1.

Table 6-1: Summary of select scaling factors for the gravo-aeroelastic scaling method

Scaling Parameter	Scale Factor
Length: $\frac{\boldsymbol{S_s}}{\boldsymbol{S_f}}$	η
Wind Velocity: $\frac{\boldsymbol{U_s}}{\boldsymbol{U_f}}$	$\sqrt{\eta}$
Rotational: $\frac{\Omega_{\text{s}}}{\Omega_{\text{f}}}$	$1/\sqrt{\eta}$
Total Blade Mass: $\frac{\boldsymbol{m_s}}{\boldsymbol{m_f}}$	$\left(\frac{\rho_{\text{wind,s}}}{\rho_{\text{wind,f}}}\right)\eta^3$
Distributed Blade Mass: $\frac{\boldsymbol{m'_s}}{\boldsymbol{m'_f}}$	$\left(\frac{\rho_{\text{wind,s}}}{\rho_{\text{wind,f}}}\right)\eta^2$
Flap-wise Frequency: $\frac{\boldsymbol{\omega_{flap,\,s}}}{\boldsymbol{\omega_{flap,\,f}}}$	$1/\sqrt{\eta}$
Stiffness: $\frac{(\boldsymbol{EI'})_{\boldsymbol{s}}}{(\boldsymbol{EI'})_{\boldsymbol{f}}}$	$\left(\frac{\rho_{\text{wind,s}}}{\rho_{\text{wind,f}}}\right)\eta^5$
Reynolds Number: $\frac{\boldsymbol{Re_s}}{\boldsymbol{Re_f}}$	$\left(\frac{\rho_{\text{wind,s}}}{\rho_{\text{wind,f}}}\right)\left(\frac{\mu_{\text{wind,f}}}{\mu_{\text{wind,s}}}\right)\eta^{3/2}$
Mach Number: $\frac{\boldsymbol{Ma_s}}{\boldsymbol{Ma_f}}$	$\left(\frac{a_{\text{wind,f}}}{a_{\text{wind,s}}}\right)\sqrt{\eta}$

6.2.2 *Test Facility Characteristics*

The scale model presented herein is designed for mounting at the NREL FC on the two-bladed Controls Advanced Research Turbine (CART-2) platform. A wind rose data distribution for the NREL FC is seen in Figure 6-1 for 1-minute average wind speed over the years 2014-2017. As depicted, the primary direction of wind comes from 292 degrees with maximum wind speeds reaching 40 m/s during this time period. Since the winds at NREL FC come from a concentrated primary direction, the meteorological tower for the CART-2 turbine was located 86-meters upwind of the tower in the direction of the primary winds. The wind site has a typical turbulence intensity level of 18% year-round and the estimated 50-year gust wind speed for this site is 70 m/s.

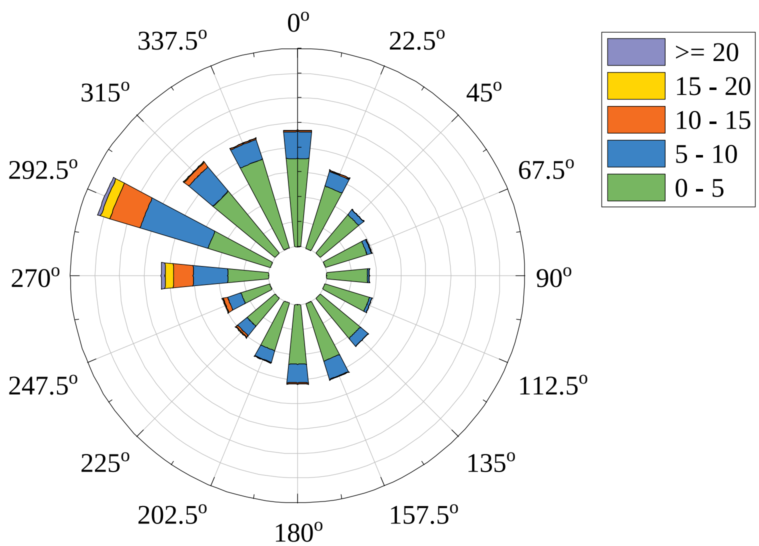

Figure 6-1: Based on data recorded from 2014-2017, the 1-minute average wind speed and direction distributions at 50-meters height for the National Renewable Energy Labs Flatirons Campus.

The meteorological tower consists of four distributed cup anemometers located at 3 m, 15 m, 36.6 m, and 58.2 m from the ground. This allows the mean wind shear to be determined for a given test period. Additionally, a sonic anemometer is located at 36.6 m above the ground giving the three wind speed (U) components in the x, y, and z directions. Since this height corresponds roughly to the hub-height of the CART-2 and velocity recorded at this location allows the instantaneous wind velocity direction and magnitude as well as the mean wind speeds and turbulence level to be determined for a given test period.

6.2.3 *SUMR-D Gravo-Aeroelastic Scaling*

The gravo-aeroelastic scaling of Section 6.2.1 was applied to the 13.2-MW Segmented Ultralight Morphing Rotor (SUMR-13) to design a 20% sub-scale rotor that could be tested with the winds described in Section 6.2.2. The full-scale SUMR-13 turbine is a 2-bladed downwind rotor designed with 12.5-degrees of coning in order to align the loads with the blade during operation [12,27,29,32]. The SUMR-D is also a 2-bladed rotor with full geometric scaling of the SUMR-13 blade.

However, there were some differences between the two turbines that were necessitated by mounting the blades on the CART-2 platform. The SUMR-13 is based on independent pitch control with zero teeter, zero shaft tilt and 12.5 degrees of coning. In contrast, the SUMR-D is employed with a shaft tilt (τ) of 3.7-degrees, collective pitch controls, and the CART platform has no coning. To ensure that the blades are set at 12.5-degrees of coning (to achieve similar load-alignment), this necessitated an adapter to be added inboard of the SUMR-D blades (as explained in the next section). The adapter radius is defined as $r_{adapter}$, and was designed to be small compared to the total rotor radius. While the CART-2 has the ability to teeter, the SUMR-D turbine was run with the teeter brake fully applied (effectively removing teeter).

Other differences were related to the site wind conditions described in Section 6.2.2. SUMR-13 was designed for a Class IIB wind site with a rated wind speed of 11.3 m/s and a 50-year gust of 59.5 m/s. SUMR-D at scaled conditions would therefore have a rated wind speed of 5.05 m/s and an ideal 50-year gust of 26.6 m/s. However, the 50-year gust for the NREL FC where SUMR-D was tested is about 70 m/s. Furthermore, NREL FC typically has 18% turbulence intensity while an idealized SUMR-D scaled environment would have a turbulence intensity of 14%. As such, NREL FC represents a much more severe testing environment in terms of the normalized 50-year gust speed and turbulence levels. To address this, the SUMR-D blade required additional structural robustness than would otherwise be employed for ideal scaling. As such, careful design was needed to also try and best match the full-scale aeroelastic response. In particular, the inboard portion of SUMR-D blades were designed and manufactured with higher distributed-mass density and stiffness than ideal scaling would suggest as shown by the non-dimensional distribution of Figure 6-2. This extra structural mass in the inboard portion is seen to be very large with an order of magnitude greater mass density and stiffness at the root ($\bar{s}$ =0). Despite the additional blade mass and robustness, the outboard stiffness was maintained to be consistent with theoretical scaling. This is critical as the stiffness in this portion primarily determines the aeroelastic deflection. As such, this design compromise based on stiffness and mass distribution was intended to allow both aeroelastic scaling for the SUMR-D while ensuring safe deployment at the NREL FC.

a) b)

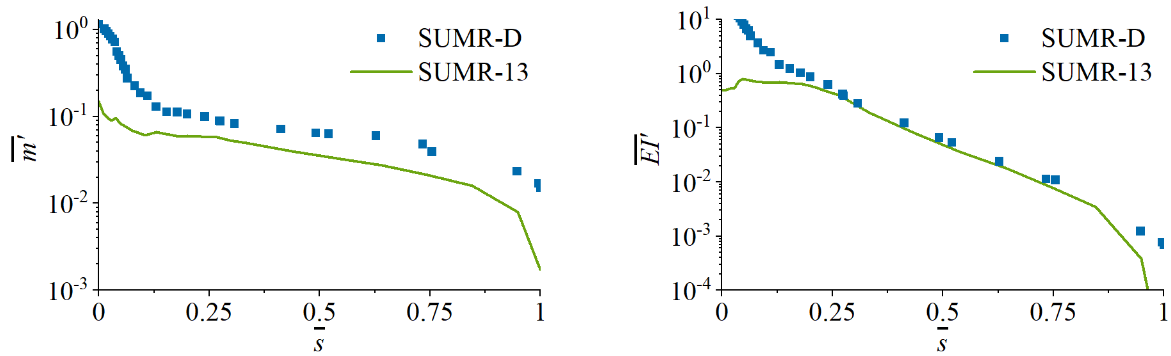

Figure 6-2: Distributed non-dimensional a) mass density ($\overline{m'}$) and b) stiffness ($\overline{EI'}$) over a non-dimensional blade length ($\bar{s}$) for the SUMR-13 and the manufactured SUMR-D rotors.

A summary of the blade properties, environmental conditions, and control set points are given in Table 6-2 for the full-scale SUMR-13, the ideally scaled SUMR-D (at a scaled environmental site), and the fabricated SUMR-D for the NREL FC testing site. The higher than ideal distributed mass and stiffness as well as differences in Reynolds number due to scaling results in the turbine operating with smaller than desired blade loads and deflections. To alleviate these differences, the controller is designed to be operated at differing set points in order to more closely match the goals as set out by the scaling goals summarized in Section 2.1. This included increasing the rated wind speed and the rotor rated rotation rate. The intent was to best match the non-dimensional loads and deflections with these adjustments (and the degree to which this scaling was successful is discussed in the results).

Table 6-2: Aerodynamic, structural, control, and environmental summary of the SUMR-13, Ideal SUMR-D, and fabricated SUMR-D turbines.

	SUMR-13	Ideal Scaled SUMR-D	SUMR-D Fabricated
Aerodynamic and Structural			
Design Innovation	Extreme Scale	Extreme Scale	Extreme Scale
Length Scaling Factor (η)	1	0.2	0.2
Blade Length (S)	104.36 m	20.87 m	20.87 m
Hub Radius (r_{hub})	2.5 m	0.5 m	1.38 m
Adapter Length (r_{adapter})	0 m	0 m	0.5 m
Coning Angle (β)	Variable	12.5 degrees	12.5 degrees
Shaft Tilt (τ)	0 degrees	0 degrees	3.77 degrees
Rated Froude Moment (Fr_{moment})	10.39	10.39	8.61
Blade Mass (m)	54787 kg	350.6 kg	985.6 kg
Flapwise Frequency (ω_{flap}) at 0 rpm	0.68 Hz	1.21 Hz	1.13 Hz
Flapwise Frequency (ω_{flap}) at Ω_{rated}	0.71 Hz	1.53 Hz	1.25 Hz
Ref. Reynolds Number (Re)/10^6	16.3	1.16	1.27
Ref. Mach Number (Ma)	0.227	0.101	0.111
Environment			
50-year Gust ($U_{\text{50-year}}$)	59.5 m/s	26.6 m/s	70 m/s
Turbulence Intensity (TI)	14%	14%	18%
Controls			
Tip-Speed Ratio (λ)	9.5	9.5	9.5
Rated Wind Speed (U_{rated})	11.3 m/s	5.05 m/s	5.75 m/s
Rated Rotor Speed (Ω_{rated})	9.82 rpm	21.96 rpm	21.47 rpm
Region II Pitch (ϕ)	0.458 degrees	0.458 degrees	-5 degrees

6.2.4 Effective Azimuthal and Coning Angles

As previously noted, the SUMR-13 has 12.5-degrees of coning at rated conditions, and thus the ideally scaled rotor would have the same coning angle. However, the CART-2 platform has no coning available. Therefore, a 0.5 m adapter is artificially mounted between the root of the blade and the pitch system of the platform. Figure 6-3 contains images of the root adapter being installed on the turbine and the mounting of the blades on the CART-2 turbine with the 12.5-degrees coning adapter.

a) b)

Figure 6-3: The coning adapter to provide a 12.5-degree coning of the blades showing a) the installation of the adapter and b) the SUMR-D blades being mounted on the CART-2 turbine with the 12.5-degree coning adapter. *Photos by Lee Jay Fingersh, NREL*

Since the pitch system is located in-board of the 12.5-degree coning adapter this causes a pitch-coning coupling to occur during operation. This leads to effective blade coning angles (β_{eff}) and azimuthal angles (Ψ_{eff}) which differ from their output values based upon the pitch (ϕ) of the blade. Equations (6.10) and (6.11) provide the conversions of the actual values to their effective values. Figure 6-4 provides the nominal vs. effective values as a function of the blade pitch over the operating pitch ranges.

$$\Psi_{\text{eff}} = \tan^{-1}\frac{\sin(\psi)\sin(\phi)\sin(\beta) + \sin(\psi)\cos(\beta)}{\sin(\psi)\sin(\phi)\sin(\beta) - \cos(\psi)\cos(\beta)} \tag{6.10}$$

$$\beta_{\text{eff}} = \tan^{-1}\frac{-cos(\phi)\sin(\beta)}{\sqrt{[\cos(\psi)\sin(\phi)\sin(\beta) - \sin(\psi)\cos(\beta)]^2 - [\sin(\psi)\sin(\phi)\sin(\beta) - \cos(\psi)\cos(\beta)]^2}} \tag{6.11}$$

As seen, this can cause a 5-degree difference in azimuth angle (ψ) and a 1.25-degree difference in coning angle (β).

a) b)

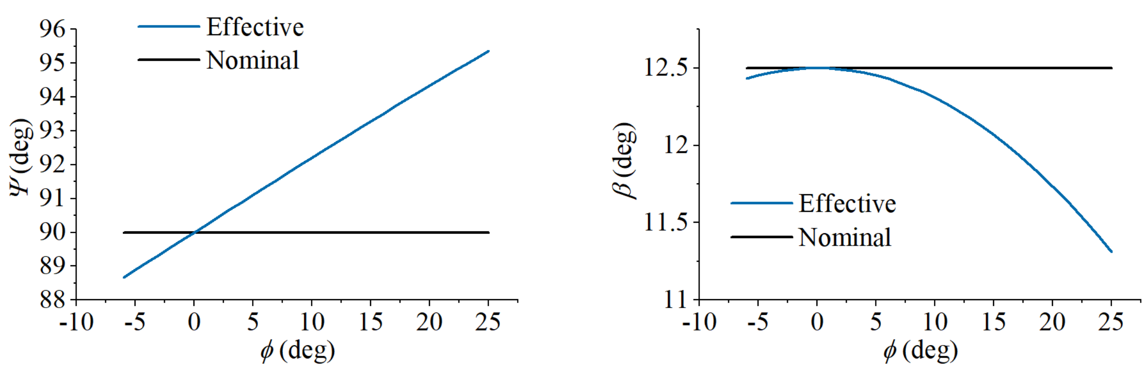

Figure 6-4: The effective a) azimuth (Ψ_{eff}) and b) coning (β_{eff}) angles as functions of pitch (ϕ) of the experimental SUMR-Demonstrator as compared to their output values due to a cone-pitch coupling on the turbine.

6.2.5 CART-2 SUMR-D Test Data Collection

The CART-2 platform samples data at 400 Hz, and 230-minutes of data are analyzed for all operational results excluding the tip deflection analysis. Table 6-3 provides characteristic data for the experimental tests. The turbine data recording system outputs instantaneous data for the RPM (Ω), pitch angles (ϕ), azimuth angles (ψ) and strain gauge moment data (M). A typical test interval for operational performance and moment collection was about 5-minutes (300 seconds) and more than 40 test intervals were used for total averaging. In addition, video feed was recorded and converted to tip deflections as will be discussed in Section 6.2.6. Table 6-3 provides total time of measurements (sum of all intervals) and other characteristic data for the experimental tests. As will be shown in the results, the moments and deflections were considered in terms of the instantaneous values as a function of wind speed in 1 m/s wind velocity bins, while rotation rate and pitch were considered over 1-minute averages with 0.5 m/s bins.

The moments are measured through strain gauges located 48 cm from the root of the blade aligned with zero-degrees pitch. The strain gauges were calibrated in low wind conditions to match the predicted bending moments on the rotor. To minimize the potential effects of temperature drift, the moments were recalibrated on a case-by-case basis.

Table 6-3: Wind data characteristics for the experimental conditions.

Data	Total Time (min)	Sampling Rate (Hz)	Bin Width (m/s)	Mean Horizontal Velocity (m/s)	Mean Turbulence Intensity	Mean Yaw Offset (deg)
Rotation Rate and Pitch	230	400	0.5	5.3 ± 2.04	17.3%	-0.55 ± 14.1
Moments	230	400	1	5.3 ± 2.04	17.3%	-0.55 ± 14.1
Deflections	17.25	10	1	4.54 ± 0.64	14.0%	-13.2 ± 13.6

The operational data were considered as a function of the horizontal wind speeds as defined by a cup anemometer located on the nacelle of the wind turbine as this is nearby to the rotor plane. Figure 6-5 displays two example data intervals with horizontal wind speed. The wind field shear is characterized through a power law exponent determined by the distributed meteorological tower cup anemometers described in Section 6.2.2. The three-directional components of the wind velocity are gathered from sonic anemometer data on the meteorological tower and used to determine the horizontal and vertical flow angles.

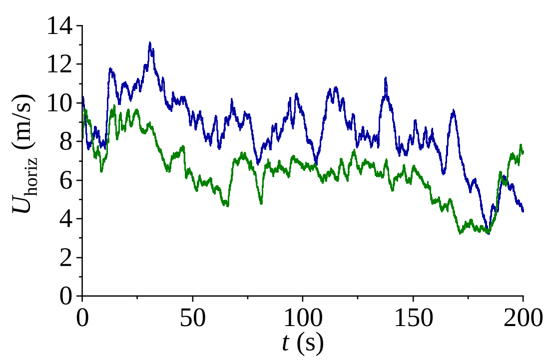

Figure 6-5: Two samples of 200-second horizontal wind speeds (U_{horiz}) for the experimental SUMR-D results showing the range of wind speeds over time (t) as measured by the cup anemometer located on the nacelle of the turbine.

6.2.6 Tip Deflection Collection

For collecting the aeroelastic deflections of the experimental tests, a camera was mounted on the hub of the turbine and pointed towards the tip of the blade as seen in Figure 6-6. Due to the camera being inboard of the pitch system, the pitch-coning coupling describe in Section 6.2.4 limits the results to blade conditions with non-changing pitch angle (Region 2).

Figure 6-6: Image of the camera used to determine tip deflections stationed on the hub of the rotor and pointed towards the tip of the blade.
Photo by Lee Jay Fingersh, NREL

To convert the video images into blade deflections, a series of processing steps were needed. To first find the zero location of the blade, tabs are mounted at 8 m, 13 m, and 20.869 m along the blade. These three tabs are shown in Figure 6-7a for parked conditions at near-zero wind speeds (only gravitational deflection) with the blades in the horizontal (T-position) and pitch-to-run (Region 2). A ruler was also used at each of the three tabs so that any deflection at the outboard location was calibrated. These three positions ($p_8, p_{13}, p_{\mathrm{tip}}$) were used to determine the pixel locations in the x- and y-directions, e.g. $p_{\mathrm{x,tip}}$ and $p_{\mathrm{y,tip}}$ for the tip location. Given the x- and y- values, the distances between any two locations could be obtained. Figure 6-7b shows the pixel distances between each tab used for finding the blade deflection relative to the calibrated reference blade condition. This calibration was used to determine conversion from pixel location to deflection distances. The pixel-to-distance conversion at the tip (δ_{pixel}) on Blade 1 of the SUMR-D rotor (the only deflection measurements to be presented herein) is 1.43 mm/pixel.

a)

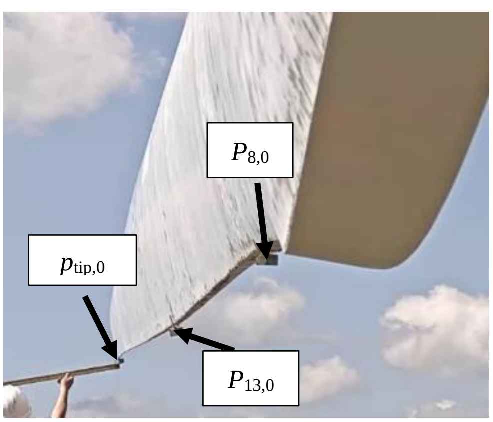

b)

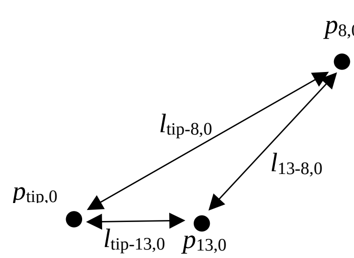

Figure 6-7: a) A view from the hub-mounted camera towards Blade 1 for the calibrated reference image in a horizontal pitch-to-run configuration with the pixel locations for the 3 tabs located at 8 m, 13 m, and the tip ($p_8, p_{13}, p_{\mathrm{tip}}$), b) definition of the three lengths between tabs for the calibrated reference image.
Photo by Lee Jay Fingersh, NREL

To determine the video reference frame (with no relative deflection) within a video sequence when the turbine was operating, a deviation length (L) with units of pixels was defined based on the distances between the tabs in an operational video image relative to that for the calibrated reference image (taken while parked) as:

$$L = \sqrt{(l_{\text{tip}-8} - l_{\text{tip}-8,0})^2 + (l_{\text{tip}-13} - l_{\text{tip}-13,0})^2 + (l_{13-8} - l_{13-8,0})^2} \tag{6.12}$$

The reference frame for each video was defined as the image which minimizes this deviation length, and thereby minimizes the RMS error. For this reference image, the tip location was obtained in terms of pixel locations as $p_{tip,x,0}$ and $p_{tip,y,0}$. For all other images in the video sequence, the tip deflection can then be found using the conversion between pixels distance and physical distances as:

$$\delta_{\text{tot}} = \delta_{\text{t,pixel}} \sqrt{(p_{\text{tip,x}} - p_{\text{tip,x,0}})^2 + (p_{\text{tip,y}} - p_{\text{tip,y,0}})^2} \tag{6.13}$$

Since these deflections indicate deformation in both directions, the measured deflections are the total deflections from both flapwise and edgewise effects. However, due to the camera capturing a two-dimensional still frame at a given time, out of plane bending and torsional bending (due to the tabs not being located on the airfoil center of twist) is not captured.

6.2.7 Computational Methods

To predict the SUMR-D moments and deflections and to assess the efficacy of the scaling approach for SUMR-13, a set of simulations was conducted using FAST [34], a wind turbine simulation software developed and maintained by NREL. The full-scale blade input is the original design for the SUMR-13 blade which has zero-degrees of tilt, a constant 12.5-degrees of coning, and no teeter. The structural characteristics of the SUMR-D employ a 'digital twin' constructed based on the manufactured model, ground testing, as well as total mass and stiffness distribution down the length of the blade [28,35]. The digital twin of the manufactured rotor has 3.7-degrees of shaft tilt and zero teeter as is found in the experimental tests. However, the simulations have a constant 12.5-degrees of coning as opposed to the experimental tests which has a coning angle which is dependent on the pitch angle. The aerodynamics of the SUMR-D blade used in FAST take into account the changes in Reynolds numbers and have a lower lift-to-drag ratio than that of the SUMR-13 blade. It should be noted that the FAST predictions herein neglect the tower shadow effects since this has been shown to have a negligible impact on the unsteady blade moment in comparison to the effects of incoming turbulence based on predictions by [36].

The FAST windspeed inputs are developed using the full-field turbulent-wind simulation tool, TurbSim v2 [37], developed by NREL specifically for use with FAST. The wind input time series for a given interval are based upon the sonic anemometer located on the meteorological tower as described in Section 6.2.2 with the incoming wind speeds are rotated such that each wind file has an average cross wind angle of 0-degrees. To further reduce the cross-angles and match the experimental results, the simulations are run with the yaw control turned on. Additional input parameters to the TurbSim model are the horizontal and vertical flow angles based upon the sonic anemometer wind speeds and the power law exponents based upon the distributed cup anemometer average wind speeds on the meteorological tower. The SUMR-D simulations for a given interval are typically 400 seconds long with the first 100-seconds removed (to eliminate any initial numerical transients) to provide 300 seconds of data to be compared with experiment. The SUMR-13 interval simulations are 500 seconds long (longer than SUMR-D input files due to the effects of time scaling) with the first 100 seconds similarly removed. An example non-dimensional time-series of wind inputs located at the hub are shown in Figure 6-8 with the wind speeds nondimensionalized by equation (6.7) and time being nondimensionalized ($\bar{t}$) by equation (6.14).

$$\bar{t} = {}^{tU_{\text{rated}}}\!/_{S} \tag{6.14}$$

It can be seen that the instantaneous values are not necessarily equal at a given time, but the mean and RMS of the wind velocities are equal. This is deemed suitable if we are to compare the means and RMS of the moments and deflections.

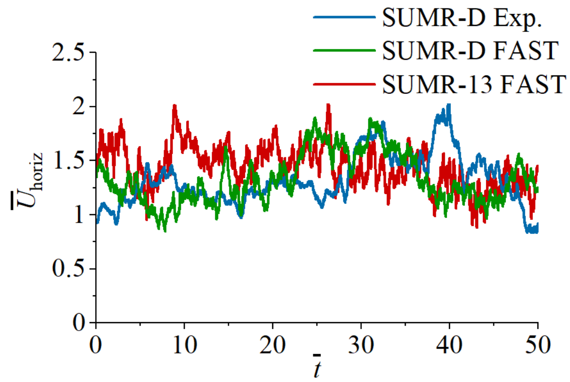

Figure 6-8: Non-dimensional horizontal wind speeds ($\overline{U}_{\text{horiz}}$) against a non-dimensional time ($\bar{t}$) for the SUMR-D experimental data, SUMR-D FAST simulations and SUMR-13 FAST simulations.

FAST predicts both the flapwise (δ_{flap}) and edgewise (δ_{edge}) deflections based upon a non-deflected blade state; however, the SUMR-D experiments determines the deflections as a total distance (δ_{tot}) reference to a static state with only gravitational deflections. Therefore, FAST data output were processed to be consistent with the experimental model by obtaining the deflected state in a horizontal pitch-to-run configuration for the flapwise ($\delta_{\text{flap},0}$) and edgewise ($\delta_{\text{edge},0}$) directions. Therefore, the tip deflection distances for the FAST simulations are determined by equation (6.15).

$$\delta_{\text{tot}} = \sqrt{(\delta_{\text{flap}} - \delta_{\text{flap},0})^2 + (\delta_{\text{edge}} - \delta_{\text{edge},0})^2} \tag{6.15}$$

Finally, the computational moments for SUMR-D are determined at the 48cm spanwise location (2.3% of the blade length), to match the strain gauge location on the SUMR-D rotor. However, the strain gauge locations consider flapwise and edgewise relative to zero-degrees pitch while the FAST flapwise and edgewise moments are relative to the local airfoil twist (φ). To convert the moments, SUMR-D and SUMR-13 blade twists of 34.3- and 13.5-degree twists at 2.3% of the blade length are used to rotated the FAST output coordinate frames to the experimental coordinate frames as

$$M_{\text{flap}} = M_{\text{flap},\varphi} \cos\varphi - M_{\text{edge},\varphi} \sin\varphi \tag{6.16}$$

This rotation is reasonable as the airfoil shape at this inboard location is simply a cylinder.

6.3 Results and Discussion

The following results begin with reviewing the experimental bin distribution and convergence of the flapwise bending moments and tip deflections, followed by the turbine performance (operational state and moments) and tip deflections (aeroelasticity) during operation. This is followed by comparisons with the computational SUMR-13 and SUMR-D turbines to evaluate the effectiveness of the FAST simulation tool and the effectiveness of the gravo-aeroelastic scaling developed herein.

6.3.1 Experimental Wind Conditions and Bin Convergence

The general operational data sets are shown in Figure 6-9. A total of 230-minutes of data are used for this analysis at a sampling rate of 400 Hz as noted in Table 6-3. Figure 6-9a shows the Probability Distribution Function of the wind speeds within this data set. The wind speeds fall between the cut-in and the cut-out wind speeds with equal portions at above rated and below rated wind speeds (5.75 m/s). Convergence of the blade flapwise bending moments (aligned with 0-degree pitch) is evaluated by processing various portion sizes of data as shown in Figure 6-9b. In particular, this figure shows the mean and +/- one standard deviation of the bending moments for two representative wind speed bins of 3-4 m/s (below rated) and 7-8 m/s (above rated) in increments of 25% of the total data per bin. The data for both bins shows reasonable convergence with minor differences between the 50% and 100% data cases. This suggests that the mean data for each bin are converged to within about 5% of the mean. Figure 6-9c shows example data as a function of azimuthal angle for the wind speed bin of 3-4 m/s, where the blue solid line is the azimuthally-averaged bending moment. Due to the pitch-coupling aspect from the coning adapter, the minimum average value for the bending moments occurs before $\Psi = 180$ degrees since to the SUMR-D Region II pitch is -5 degrees as summarized in Table 6-2. It can also be seen that there is a large variation of the instantaneous moments about the azimuthally-averaged bending moment. This can be attributed to the large turbulence at NREL FC coupled with blade flexibility and dynamics which combine to produce significant changes in the instantaneous aerodynamic angle and blade position. Another important result of Figure 6-9c is the lack of a significant drop in the flapwise blade moment as the blade passes downstream of the tower (for Ψ of about 160 degrees). This experimental result is consistent with previous predictions that the downwind load-aligned SUMR coned design does not suffer significantly from tower shadow effects [36].

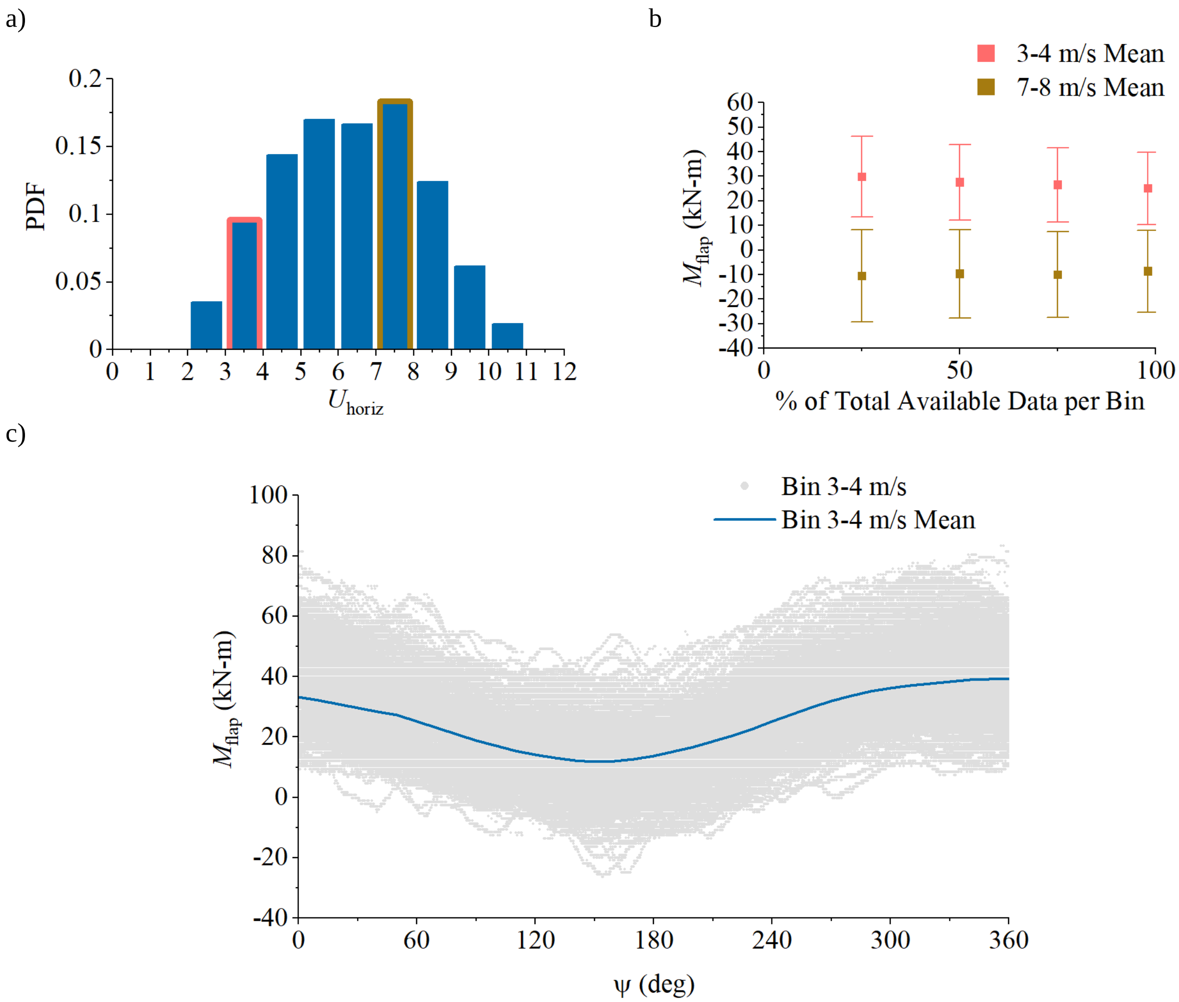

Figure 6-9: SUMR-D Experimental general operational data with 133-minutes of data sampled at 400 Hz showing: a) the Probability Distribution Function of the horizontal wind speeds, b) convergence of the mean and standard deviations for two representative bins in below-rated (3-4 m/s) conditions and above rated (7-8 m/s) conditions, and c) the instantaneous flapwise bending moments as a function of azimuth angles and the azimuthally-averaged mean values for the below-rated, 3-4 m/s bin.

The tip deflection data sets are shown in Figure 6-10. A total of 17.25-minutes of data are shown for this analysis at a sampling rate of 10 Hz and the results are portioned into 1 m/s bin. Only Region 2 results are obtained (with the pitch remaining constant within this region) due to the camera field of view constraints. Figure 6-10a shows the Region 2 wind speed conditions used in the analysis with the majority of data falling between cut-in and rated conditions. Any wind speeds in above rated conditions are gusts which occur while the system is operating in Region II. Convergence is seen in Figure 6-10b for the 3-4 m/s bin with some changes between 50%, 75% and 100% of the total available data. This trend suggests that the mean data for each bin are converged to within about 10% of the mean deflections.

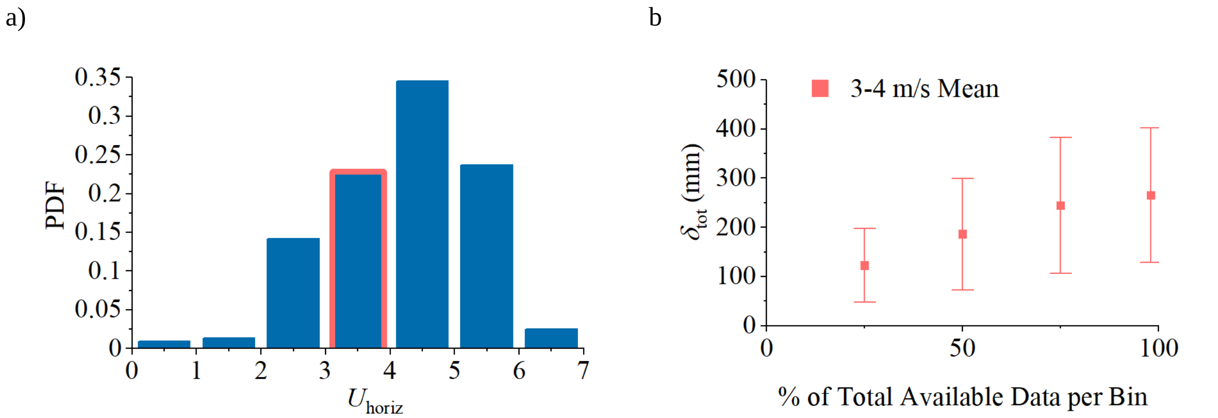

Figure 6-10: SUMR-D Experimental tip deflection data with 17.25-minutes of data sampled at 10 Hz showing: a) the Probability Distribution Function of the horizontal wind speeds with the highlighted portion as the example bin (3-4 m/s) in b) which shows the convergence of this bin as a function of percent of total data utilized.

6.3.2 Experimental Results as a Function of Wind Speed

Figure 6-11 shows the operational conditions for 1-minute average experimental data binned in 0.5 m/s bins showing the mean and +/- one standard deviation about the mean. Figure 6-11a shows the pitch of the system which follows the expected trends of wind turbine operation. The below-rated pitch conditions are saturated to -5-degrees as specified in scaling to allow the system to more closely match the full-scale system dynamics. Region 2.5 contains a high standard deviation of pitch controls due to the systems switching between Region 2 and Region 3 during operation. Figure 6-11b shows the operational rotational speed of the rotor which is held at an average of 21.47 RPM in Region 3 as defined through scaling.

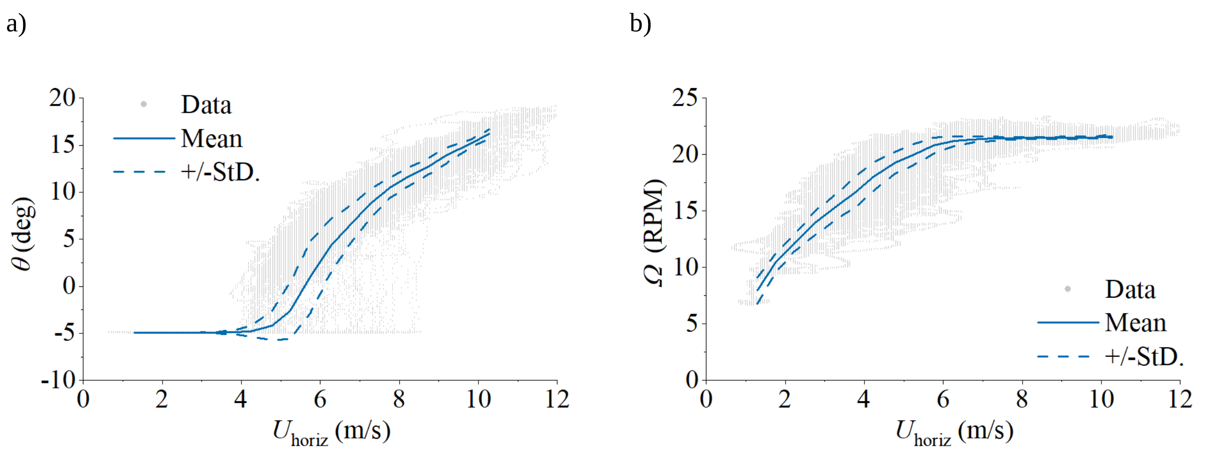

Figure 6-11: The experimental results with the mean and +/- one standard deviations about said mean averaged over 1-minute intervals and binned in 0.5 m/s bins for a) the blade pitch (θ) and b) the rotor rotational rate (Ω).

Based on the above controller and scaling parameters, the resulting flapwise blade moments and tip deflections are shown in Figure 6-12. Figure 6-12a shows the instantaneous flapwise bending moments. These moments cross through 0 kN-m at about 6.5 m/s where they are load aligned. This is expected as the full-scale SUMR-13 rotor is designed with 12.5 degrees of coning in order to load align the blades and reduce the bending moments during operation at conditions just above rated wind speed. There are large standard deviations of the blade moments across all operational conditions, which is consistent with the high turbulence levels and blade flexibility which increase as the wind speed increases. Figure 6-12b shows the operational tip deflections for Region 2 operations where the pitch remains constant. The experimental data for above rated wind speeds occurs when there are high-speed gusts while the system is operating Region 2 conditions. It can be seen that the aeroelastic deflections have high deviations about the mean and can exceed 800 mm (4% of blade length) near rated wind speeds. For a full-scale system, this is consistent with deflections of more than 4 meters.

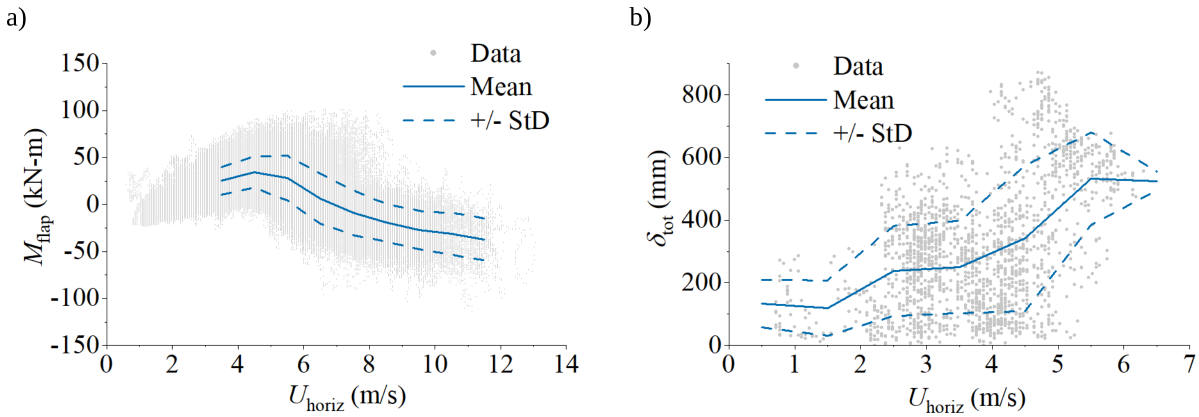

Figure 6-12: The experimental results showing the mean and +/- one standard deviation for the a) flapwise bending moments (M_{flap}) for all regions and b) tip deflections (δ_{tot}) for Region 2 pitch conditions.

6.3.3 Scaled Comparisons with FAST Predictions

To assess the efficacy of FAST as a simulation tool as well as the efficacy of scaling extreme-scale, highly flexible rotors with novel designs, the SUMR-D field test results were compared against the computational SUMR-D and SUMR-13 FAST simulations. The FAST results were run with simulated wind fields to match the experimental data as summarized in Section 6.2.5 and Section 6.2.7. For the following predictions and experiments, the data is again collected in 1 m/s bin sizes. As summarized in Section 6.2.1 the present gravo-aeroelastic scaling method targets the blade pitch, the non-dimensional rotational frequency, and rotor tip-speed ratio as being the most important values to support matching the blade loads and tip deflections.

As shown in Figure 6-13a, the mean pitch of the experimental results show saturation in below-rated conditions to a low value of -5-degrees. This aligns with the SUMR-D computational results; however, the pitch setting is different than that of the SUMR-13 since the pitch was altered in the sub-scale models in order to more closely match the full-scale blade dynamics stated by the scaling goals set in Section 6.2.1. In above-rated conditions, the controllers for the computational and experimental conditions exhibit similar pitch settings. The standard deviations for the pitch of the experimental SUMR-D rotor is shown in Figure 6-13b and are significantly higher than that of the simulations. This is attributed to the inability of the predicted controller in Region 2.5 to capture the increased dynamics between Region 2 (pitch) and Region 3 (generator speed) controllers.

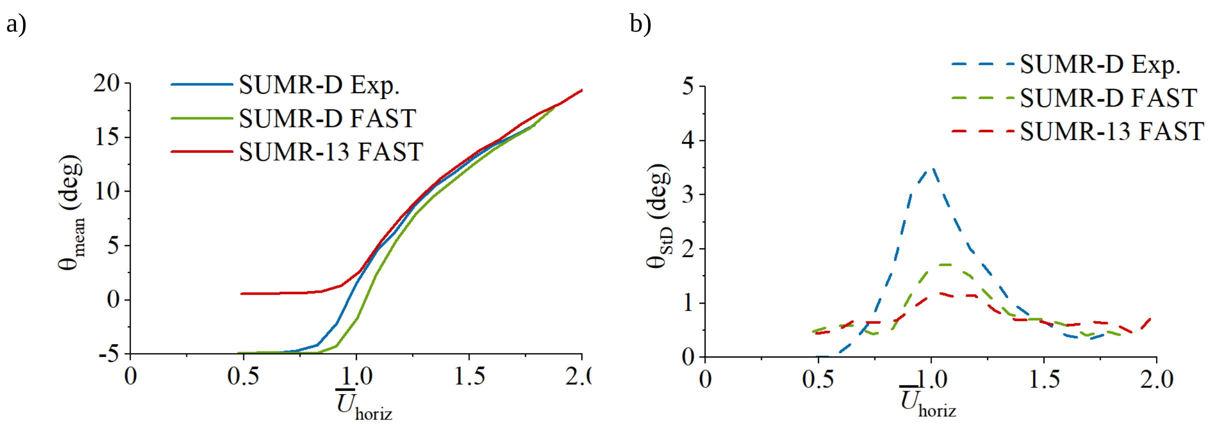

Figure 6-13: The experimental pitch averaged over 1-minute intervals in 0.5 m/s bins as compared to the computational results for the digital twin of the SUMR-D and the SUMR-13 rotor showing: a) the means and b) the standard deviations.

The non-dimensional rotor rotational rate (rotor speed normalized by the blade frequency) helps ensure the ratio of the input frequencies (rotational speed) to the output frequencies (blade frequencies) of the rotor are maintained through operation. This allows for the sub-scale system to exhibit similar response dynamics, such as resonance excitement. Figure 6-14a shows the means and +/- one standard deviations about said mean for the experimental and computational results. These results show good alignment of the SUMR-D experimental and computational results in

Region 3, though the SUMR-D FAST results have lower rotational rates than experimental results in Region 2. This is related to differences in the controls of the SUMR-D rotors. It should be noted that FAST-13 rotational frequencies are significantly smaller which was a result of the adjustments made to account for the increase inboard stiffness needed for testing at the NREL FC.

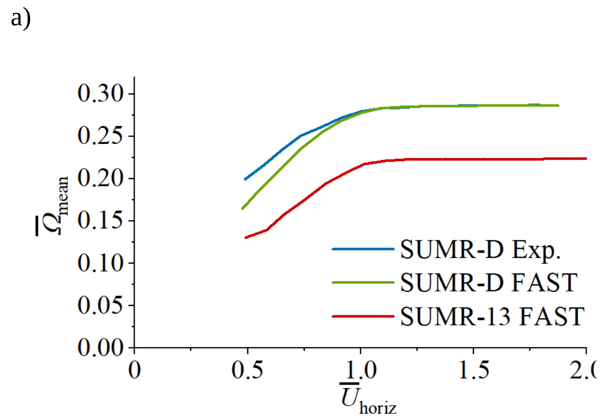

Figure 6-14: The experimental tip-speed ratios averaged over 1-minute intervals in 0.5 m/s bins as compared to the computational results for the digital twin of the SUMR-D and the SUMR-13 rotor showing: a) the means and b) the standard deviations.

Figure 6-14b shows the tip-speed ratio throughout the operating regions of the rotor. All results (experimental and computational) show reasonable alignment for the mean values during operation in Region 3 conditions. This lends itself to full-scale results as well as FAST predicting the experimental flow angles appropriately and thus well-scaled aerodynamics for above-rated conditions. For Region 2 conditions, the simulations show nearly constant mean tip-speed ratios at 9.5 which is expected, however the experimental data does not show constant tip-speed ratios which is attributed to the mismatched rotor RPM in Region 2 as seen in Figure 6-14a. The three above parameters (pitch, RPM, non-dimensional rotational frequency, and tip-speed ratio) are used to control the turbine, while the following presents the responses of the rotor to these control conditions. Figure 6-15 shows the binned instantaneous flapwise bending moments for the experimental results as compared to computational results. The experimental and computational SUMR-D flapwise moments show good agreement in Region 3 which is consistent with the rotor rpm, pitch, and blade structural models being well maintained between simulation and experiment. However, the below-rated bending moments are underpredicted as compared to experiments due to the differences in the rotor RPM as seen in Figure 6-14a. Additionally, the Region 2.5 standard deviations for bending moments are underpredicted compared to experiments which is a function of the high experimental standard deviations of pitch control as seen in Figure 6-11b. Aside from the above differences, the overall good agreement between SUMR-D FAST and experimental moments indicates that the wind flow input files for turbulence intensity and the models of the structural characteristics (especially blade stiffness) are reasonable. In fact, the SUMR-D predictions are surprisingly good given the novel rotor design (downwind, coned, and highly flexible) and the high turbulence levels.

A key aspect of the SUMR concept is load-alignment, whereby the rotor is designed so that the mean flapwise moments can be near zero for significant portions of operation. While the load-alignment has been previously predicted as part of the design, there have been no operational measurements to confirm this. In Figure 6-15a, the experiments show near-zero bending moments at a wind speed of about 20% above rated conditions for SUMR-D (as predicted by the FAST SUMR-D simulations) clearly indicating load-alignment. The full-scale SUMR-13 was designed to achieve this load-alignment at a higher wind speed as shown by the FAST SUMR-13 simulations. These results demonstrate that the load alignment concept can be directly achieved during rotor operation with this downwind turbine.

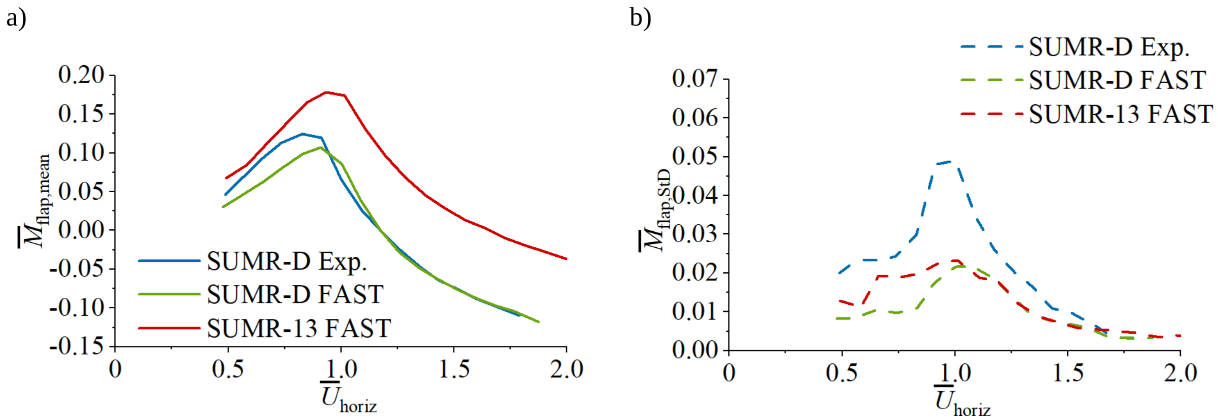

Figure 6-15: The experimental non-dimensional flapwise bending moments as compared to the computational results for the digital twin of the SUMR-D and the SUMR-13 rotor showing: a) the means and b) the standard deviations.

The above moment distributions also show that the present aeroelastic scaling approach can allow sub-scale system experimental testing that is highly reflective of full-scale operational conditions. Considering the much lower costs associated with building and testing a 20% scale turbine compared to a full-scale turbine, suggests an the enormous potential benefit for sub-scale testing in validating novel extreme-scale turbines.

Finally, the non-dimensional tip deflection distances are shown in Figure 6-16. It should be recalled that the experimental results are only shown for Region II due to the pitch-cone coupling limiting the camera field of view on the experimental rotor so that any deflections in the above-rated conditions are due to wind gusts while operating in Region 2. The simulations present data for the entirety of the operating conditions which includes Region 2.5 where the controller switches between Region 2 and Region 3 operations. As a result, the computational deflection distances are generally above those measured for the SUMR-D. For future work, it is recommended to filter the FAST simulations for low pitch conditions to have a more consistent comparison with the experimental data. Despite this, the standard deviations predicted by FAST for the SUMR-D align reasonable well with the experiments (especially considering the experimental uncertainty). Overall, the reasonable comparison between the SUMR-D computational and experimental deflections indicate that FAST has reasonable capability despite the combination of high turbulence, high flexibility, and a complex rotor design.

In terms of comparison with the full-scale predictions for SUMR-13, each of the SUMR-D models exhibit means and standard deviations below the SUMR-13 model. As with the bending moments, this is attributed to the higher blade stiffness of the SUMR-D (required for the NREL FC site testing) which leads to higher beam restoring forces acting against any additional loads on the blades. However, the overall response similarity between SUMR-D and SUMR-13 demonstrates that the present aeroelastic scaling approach allows sub-scale system experimental testing that is reflective of full-scale design of novel extreme-scale turbines.

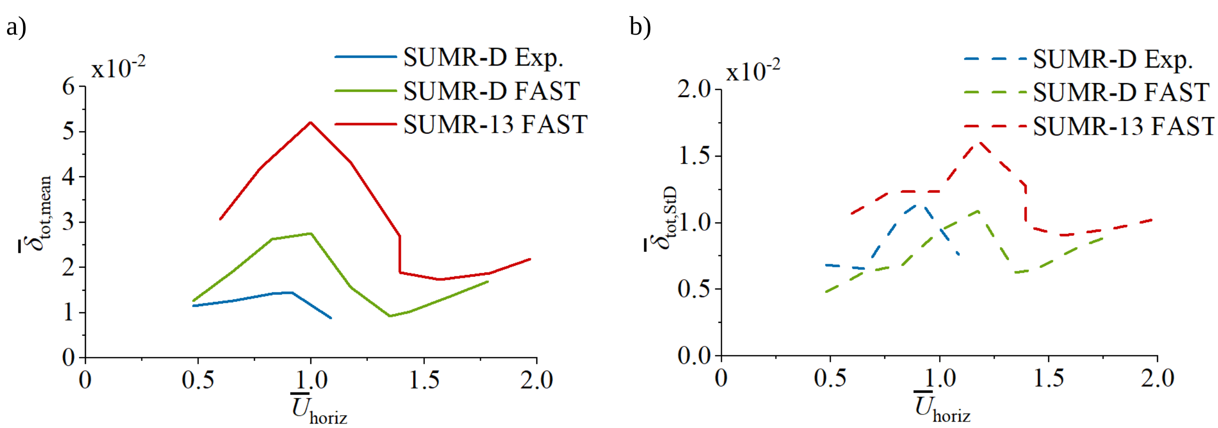

Figure 6-16: The experimental non-dimensional deflections as compared to the computational results for the digital twin of the SUMR-D and the SUMR-13 rotor showing: a) the means and b) the standard deviations.

6.4 Conclusions and Recommendations

This study presents the first operational field tests of a gravo-aeroelastically scaled rotor and the first for a design based on an extreme-scale downwind rotor with a load-aligned concept. The scaling method used in this study allows the development of sub-scale models that can reasonaby capture the dynamics and deflections of the full-scale system by matching key factors such as the non-dimensional rotational speed and outboard blade stiffness properties. The SUMR-13 model is designed to be highly flexible with a hinge at the root of the blade to allow for load alignment during operation. The sub-scale demonstrator is designed for mounting on the CART-2 tower at the National Renewable Energy Laboratory's Flatirons Campus. To match the coning of the full-scale rotor, an adapter is artificially attached to the CART-2 tower to create a 12.5-degree coning angle. The NREL FC provides higher wind conditions that those provided by an ideally scaled environment. This caused the SUMR-D to be designed with higher non-dimensional distributed mass density and stiffness for the inboard portion of the blade to withstand these conditions.

In general, data was taken over 230-minutes and sampled at 400 Hz. TurbSim v2 uses this wind data to create full-field turbulent wind files which are used by FAST along with structural characteristics of the SUMR-D digital twin and the full-scale SUMR-13 design. The results show FAST is able to reasonably match the tip-speed ratio of the full-scale rotor in Region 3. However, it displayed higher than ideal non-dimensional rotational rates and lower than ideal tip deflections. Despite these differences, the manufactured model was able to demonstrate the load-alignment concept showing the effectiveness of utilizing a downwind coned rotor for load reduction. This demonstrated load-alignment provides direct experimental support of the design performance benefits previously predicted for the SUMR concept.

In addition, the present experimental and computational results importantly show that the aeroelastic scaling approach proposed herein allowed sub-scale experimental testing that is reflective of full-scale design response, which can be an enormous cost advantage for validating novel extreme-scale turbines. Accordingly, it is recommended to continue to study to analyze the SUMR-D operational conditions to further develop and improve the gravo-aeroelastic scaling method. It is also recommended that the FAST SUMR-D controller model be revised to more accurately replicate the experimental SUMR-D controller. This will enhance the value of FAST in terms of its capability to predict the blade dynamics and deflections for extreme-scale flexible turbines. For tip deflection data collection, it can be beneficial to collect data that accounts for both out of frame bending and torsion of the blades, e.g. with a stereopair method.

References

[1] Yarmosky, A. Governer Northam Signs Clean Energy Legislation. https://www.governor.virginia.gov/newsroom/all-releases/2020/april/headline-856056-en.html#:~:text=Establishes renewable portfolio standards.,by the end of 2024.

[2] Dwyer, J., and Bidwell, D. "Chains of Trust: Energy Justice, Public Engagement, and the First Offshore Wind Farm in the United States." *Energy Research and Social Science*, Vol. 47, No. October 2018, 2019, pp. 166–176. doi:10.1016/j.erss.2018.08.019.

[3] Viselli, A. M., Goupee, A. J., and Dagher, H. J. "Model Test of a 1:8-Scale Floating Wind Turbine Offshore in the Gulf of Maine." *Journal of Offshore Mechanics and Arctic Engineering*, 2015. doi:10.1115/1.4030381.

[4] Stehly, T., and Beiter, P. *2018 Cost of Wind Energy Review*. 2018.

[5] Noyes, C., Qin, C., and Loth, E. "Pre-Aligned Downwind Rotor for a 13.2 MW Wind Turbine." *Renewable Energy*, Vol. 116, 2018, pp. 749–754. doi:10.1016/j.renene.2017.10.019.

[6] Roth-Johnson, P., Wirz, R. E., and Lin, E. "Structural Design of Spars for 100-m Biplane Wind Turbine Blades." *Renewable Energy*, Vol. 71, 2014, pp. 133–155. doi:10.1016/j.renene.2014.05.030.

[7] Griffith, D. T., and Ashwill, T. D. *The Sandia 100-Meter All-Glass Baseline Wind Turbine Blade : SNL100-00*. 2011.

[8] Griffith, D. T. *The SNL100-01 Blade: Carbon Design Studies for the Sandia 100-Meter Blade*. 2013.

[9] Griffith, D. T. *The SNL100-02 Blade : Advanced Core Material Design Studies for the Sandia 100- Meter Blade*. 2013.

[10] Griffith, D. T., and Richards, P. W. *The SNL100-03 Blade : Design Studies with Flatback Airfoils for the Sandia 100-Meter Blade*. 2014.

[11] Zalkind, D. S., Ananda, G. K., Chetan, M., Martin, D. P., Bay, C. J., Johnson, K. E., Loth, E., Griffith, D. T., Selig, M. S., and Pao, L. Y. "System-Level Design Studies for Large Rotors." *Wind Energy Science Discussions*, 2019, pp. 1–35. doi:10.5194/wes-2018-80.

[12] Ichter, B., Steele, A., Loth, E., Moriarty, P., and Selig, M. S. "Amorphing Downwind-Aligned Rotor Concept Based on a 13-MW Wind Turbine." *Wind Energy*, Vol. 19, No. 4, 2016, pp. 625–637. doi:10.1002/we.

[13] Qin, C. (Chris), Loth, E., Zalkind, D. S., Pao, L. Y., Yao, S., Griffith, D. T., Selig, M. S., and Damiani, R. "Downwind Coning Concept Rotor for a 25 MW Offshore Wind Turbine." *Renewable Energy*, Vol. 156, 2020, pp. 314–327. doi:10.1016/j.renene.2020.04.039.

[14] Osgood, R., Bir, G., Mutha, H., Peeters, B., Luczak, M., and Sablon, G. *Full-Scale Modal Wind Turbine Tests: Comparing Shaker Excitation with Wind Excitation*. 2010.

[15] Jonkman, J. M., Butterfield, S., Musial, W., and Scott, G. *Definition of a 5-MW Reference Wind Turbine for Offshore System Development*. 2009.

[16] Robertson, A. N., Jonkman, J. M., Goupee, A. J., Coulling, A. J., Browning, J., Masciola, M. D., and Molta, P. *Summary of Conclusions and Recommendations Drawn from the DeepCwind Scaled Floating Offshore Wind System Test Campaign*. 2013.

[17] Du, W., Zhao, Y., He, Y., and Liu, Y. "Design, Analysis and Test of a Model Turbine Blade for a Wave Basin Test of Floating Wind Turbines." *Renewable Energy*, Vol. 97, 2016, pp. 414–421. doi:10.1016/j.renene.2016.06.008.

[18] Goupee, A. J., Koo, B. J., Kimball, R. W., Lambrakos, K. F., and Dagher, H. J. "Experimental Comparison of Three Floating Wind Turbine Concepts." *Journal of Offshore Mechanics and Arctic Engineering*, Vol. 136, No. 2, 2014. doi:10.1115/1.4025804.

[19] Mølgaard, M., Bellew, S., and Nielsen, W. *General Rights Experimental and Theoretical Analysis of a Combined Floating Wave and Wind Energy Conversion Platform*. 2017.

[20] Kallesøe, B. S. *Aero-Hydro-Elastic Simulation Platform for Wave Energy Systems and Floating Wind Turbines*. 2011.

[21] Viselli, A. M., Goupee, A. J., Dagher, H. J., and Allen, C. "Design and Model Confirmation of the Intermediate Scale VolturnUS Floating Wind Turbine Subjected to Its Extreme Design Conditions Offshore Maine." *Wind Energy*, Vol. 19, No. 6, 2016, pp. 1161–1177. doi:10.1002/we.

[22] Dagher, H., Viselli, A., Goupee, A., Kimball, R., and Allen, C. "The VolturnUS 1:8 Floating Wind Turbine: Design, Construction, Deployment, Testing, Retrieval, and Inspection of the First Grid-Connected Offshore Wind Turbine in US."

[23] Berg, J., Bryant, J., LeBlanc, B., Maniaci, D., Naughton, B., Paquette, J., Resor, B., and White, J. "Scaled Wind Farm Technology Facility Overview." *AIAA SciTech*, 2014.

[24] Kaminski, M., Loth, E., Griffith, D. T., and Qin, C. (Chris). "Ground Testing of a 1% Gravo-Aeroelastically

Scaled Additively- Manufactured Wind Turbine Blade with Bio-Inspired Structural Design." *Journal of Renewable Energy*, Vol. 148, 2020, pp. 639–650. doi:10.1016/j.renene.2019.10.152.

[25] Loth, E., Kaminski, M., and Qin, C. "Gravo - Aeroelastic Scaling for Extreme - Scale Wind Turbines." *AIAA Aviation Conference*, 2017, pp. 1–11.

[26] Kaminski, M., Loth, E., Qin, C., Griffith, D. T., and Scaling, G. "Gravo-Aeroelastic Scaling a 13.2 MW Wind Turbine Blade to a 1-Meter Model." *AIAA SciTech*, 2018, pp. 1–12.

[27] Ananda, G. K., Bansal, S., and Selig, M. S. "Aerodynamic Design of the 13.2 MW SUMR-13i Wind Turbine Rotor." *AIAA SciTech Forum*, 2018. doi:10.2514/6.2018-0994.

[28] Bay, C. J., Damiani, R., Jay Fingersh, L., Hughes, S., Chetan, M., Yao, S., Todd Griffith, D., Ananda, G. K., Selig, M. S., Zalkind, D. S., Pao, L. Y., Martin, D., Johnson, K. E., Kaminski, M., and Loth, E. "Design and Testing of a Scaled Demonstrator Turbine at the National Wind Technology Center." *AIAA Scitech Forum*, 2019.

[29] Loth, E., Selig, M. S., and Moriarty, P. "Morphing Segmented Wind Turbine Concept." *AIAA Applied Aerodynamics Conference*, No. July, 2010, pp. 1–6. doi:10.2514/6.2010-4400.

[30] Loth, E., Steele, A., Ichter, B., Selig, M. S., and Moriarty, P. Segmented Ultralight Pre - Aligned Rotor for Extreme - Scale Wind Turbines. 2012.

[31] Peeters, M., Santo, G., Degroote, J., and Paepegem, W. "The Concept of Segmented Wind Turbine Blades: A Review." *Energies*, Vol. 10, No. 8, 2017, p. 1112. doi:10.3390/en10081112.

[32] Noyes, C., Qin, C., and Loth, E. Ultralight, Morphing Rotor for Extreme-Scale Wind Turbines. 2017.

[33] Loth, E., Steele, A., Qin, C., Ichter, B., Selig, M. S., and Moriarty, P. "Downwind Pre-Aligned Rotors for Extreme-Scale Wind Turbines." *Wind Energy*, Vol. 20, No. 7, 2017, pp. 1241–1259. doi:10.1002/we.

[34] Jonkman, J. M., and Buhl, M. L. *FAST User's Guide*. 2005.

[35] Yao, S., Griffith, D. T., Chetan, M., Bay, C. J., Damiani, R., Kaminski, M., and Loth, E. "A Gravo-Aeroelastically Scaled Wind Turbine Rotor at Field-Prototype Scale with Strict Structural Requirements." *Renewable Energy*, 2020. doi:10.1016/j.renene.2020.03.157.

[36] Noyes, C., Qin, C., and Loth, E. "Tower Shadow Induced Blade Loads for an Extreme-scale Downwind Turbine." *Wind Energy*, Vol. 23, No. 3, 2020, pp. 458–470. doi:10.1002/we.2415.

[37] Jonkman, J. M., and Kilcher, L. *TurbSim User's Guide: Version 1.06.00*. 2012.

7. Conclusion

7.1 Key Results

The included study presented a gravo-aeroelastic scaling method which reduces the cost of testing novel wind turbine designs at a fraction of the full-scale cost while capturing the full-scale blade dynamics and deflections during operation. The scaling method developed is a geometrically scaled rotor which is structurally designed to match the non-dimensional distributed blade mass and stiffness to fully replicate the full-scale gravitational, aerodynamic, and elastic loads on the rotor. These results were accomplished by matching the non-dimensional tip-speed ratio, the ratio of the rotational rate to the blade flapping frequency, and the operational tip deflections normalized by the blade length. The gravo-aeroelastic scaling method was demonstrated with three key models based upon highly flexible, extreme-scale rotors: a 20% ideally scaled computation model, an additively manufactured 1% model, and a manufactured 20% model which was testing in both parked and operational conditions.

The gravo-aeroelastic scaling method was first applied to the 13-MW, 104 meter blade, Segmented Ultralight Morphing Rotor (SUMR-13). This blade was computationally designed to be an ideally scaled rotor design which includes perfect scaling of the blades, rotor-nacelle-assembly, wind field, and control systems. This method retains the controller, aerodynamic, and gravitational interactions in order to analyze the effects of the Reynolds number differences on a turbine in a 20% scale environment for a servo-aero-gravoelastic (SAGE) scaling method. The goal of this scaling is to match the tip-speed ratio, the rotor rotational frequency normalized by the rotor speed, and the average tip deflections normalized by the blade length. Despite the differences in Reynolds number at the sub-scale, the turbine was able to match the stated goals to the full-scale model thus showing the SAGE method is viable at a 20% scale.

The SAGE method was then redeveloped for a gravo-elastically scaled rotor which is applied for a 1% model of the full-scale SNL100-03 rotor blade. To meet the strict structural requirements for a 1% model of a highly flexible light weight blade, the 1% model was additively manufactured and utilized a bio-inspired structural shape. This method allows for a low-cost fabricated model that can reflect the proper non-dimensional flapwise dynamics and elastic deflections of the full-scale blade. The scaling was achieved by reasonably reproducing the non-dimensional flapwise frequency, tip-deflections, deflection shapes, and linear mass density distributions of the full-scale model. The scaling performance of the various blade structural designs presented were evaluated through gravo-elastic ground tests and quantified with a Blade Structural Scaling Error (BSSE) which considers the differences in total blade mass and deflections. The final 1% blade model presented had the lowest BSSE 0.16 which is based on a 3% mass error and a steady flapwise tip deflection error or 15.6%.

A gravo-aeroelastic scaling (GAS) method was then applied to the full-scale 13-MW Segmented Ultralight Morphing Rotor (SUMR-13) for mounting and testing at the National Renewable Energy Laboratory’s Flatirons Campus. This model intends to replicate the non-dimensional tip deflections, tip-speed ratio, and the non-dimensional rotational rate for testing at the National Wind Technology Centers Flatirons Campus (NREL FC) on the two-bladed (upwind) Controls Advanced Research Turbine (CART-2). The NREL FC presents wind conditions which are harsher than that of an ideally scaled environment based on the full-scale SUMR-13 environment. This resulted in higher than ideal distributed blade mass density and stiffness. While this was non-ideal, the total blade mass of the sub-scale model is half the weight of conventional rotors of the same size and therefore the gravitational dynamics of the extreme-scale rotor are present at the sub-scale. Despite these differences between the sub-scale and full-scale, computational results revealed a rotor design which appropriately scales the mean and fluctuating blade tip deflections reasonably well in above-rated conditions which was the primary testing region of the NREL FC through adjustments to controller set points.

The previously stated 20% GAS manufactured model of the SUMR-13 blades were then tested in parked conditions at the NREL FC on the CART-2 turbine. The turbine was tested in two horizontal configurations: pitch-to-run and pitch-to-feather. Results are presented through root bending moments for both configurations and through tip deflections for the pitch-to-run configuration. The experimental results were non-dimensionally compared against computational results for the ‘digital twin’ of the manufactured model and for the full-scale SUMR-13 model subject to a comparable full-scale wind field using FAST which exhibited low cross-winds. The results show the SUMR-D FAST simulations had an appropriate coefficient of lift but a higher coefficient of a drag and lower stiffness than those of the manufactured model. Additionally, the results indicated the SUMR-13 rotor has a lower blade stiffness than the sub-scale models as was expected due to the design of the manufactured model needing to withstand the high wind conditions at the NREL FC.

The study concluded with observing the operational conditions for the manufactured SUMR-D rotor. The main goals for the gravo-aeroelastic scaling method were described in detail with the tip-deflections, rotational rate normalized by the blade frequency, and tip-speed ratio being the primary drivers in the scaling process. Likewise with the parked testing, the experimental results are compared against the non-dimensional computational results for both the ‘digital twin’ of the manufactured model and the full-scale model. Each of the computational models were subjected to non-dimensional wind fields similar those present in the experimental tests. The results show good alignment for the tip-speed ratio of the full-scale rotor, however it displays higher than ideal non-dimensional rotational rates and lower than ideal tip deflections. Despite these differences, the manufactured model was able to demonstrate the load-alignment concept by having a reduction in blade loads through operation.

7.2 Contributions to the Field

The included dissertation developed a scaling method which was accurately used to model full-scale novel computational blade designs at a sub-scale size to save both time and cost of manufacturing. While this method was applied to extreme-scale rotors the concepts can be applied to many applications such as: conventional horizontal axis wind turbine rotors, vertical axis wind turbine rotor, airplanes, etc.

The SAGE method outlined in Chapter 2 provided an ideal scaling method for all systems of a wind turbine blade including the control systems. This development provided methods for sub-scaling all aspects of the wind turbine assembly which can be utilized in whichever manor is beneficial to the current research efforts.

The 1% model produces an additively manufactured model which utilized bio-inspired structural designs to match the non-dimensional full-scale mass and stiffness distributions. The additive manufacturing techniques can lower the cost of full-scale manufacturing and testing, providing the opportunity to investigate several novel designs at a faster rate than with conventional manufacturing techniques. Additionally, when additively manufacturing, structural designs can go beyond those developed while using conventional manufacturing techniques thus reducing the mass of materials needed and therefore the total cost of the wind turbine.

The 20% manufactured scaled model showed a fully-completed example of the gravo-aeroelastic scaling method and its ability to develop sub-scale rotor which represent the full-scale rotor dynamics. The study begins with an in-depth development of the method used, the application to a 20% model, and finishes with the experimental results for parked and operational conditions. This study can be used for many other novel wind turbine designs looking to create sub-scale rotor which can accurately represent the full-scale dynamics at a fraction of the cost and time to build the full-scale turbine.

7.3 Future Studies and Recommendations

It is suggested for future work to continue the study into the ideal scaling of the 20% rotor by adjusting either the aerodynamics or control system of the rotor in order to fully-match the extreme-scale dynamics and deflections. This will provide opportunities to improve upon the scaling method and create scale models which accurately portray the dynamics of extreme-scale systems. Additionally, noting the success of using additive manufacturing for the 1% model with a structural optimized bio-inspired design, it is suggested to further explore additive manufacturing for full-scale non-conventional blade designs. This concept may lead to a reduction the blade mass while continuing to maintain the structural stiffness and can lead to a reduction in the Levelized Cost of Energy due to the ease of manufacturing.

As the full-scale SUMR-13 is designed with many novel characteristics it is suggested the SUMR-D experiments are observed for these results and their ability to reduce loads on the blades. Such concepts include the downwind rotor concept which can be effected by tower shadow. As such, it is suggested the SUMR-D experimental data are investigated to characterize and understand tower shadow effects. Additionally, the SUMR-13 design includes a 12.5% coning angle allowing for a reduction in loads on the blades which allows for the lightweight structure they present. While the load alignment concept is show through the low blade loads through operational conditions, a further in depth study of the load alignment concept is desired.

Finally, it is suggested to develop scaling methods which accurately measure the coupling of blade modes in extreme-scale rotors. For the current study, a strong emphasis on the flapwise dynamics was observed as these are of concern for tower strike in flexible rotors. However, as rotor blades become more flexible, there is a higher opportunity for modes to be coupled and it is suggested to develop a scaling method which captures these coupled modes and dynamics of the blades in a sub-scale model.